A MULTI-TECHNIQUE APPROACH TO DETERMINE TEMPORAL AND
SPATIAL VARIABILITY OF GROUNDWATER-STREAM WATER
EXCHANGE IN ÇAKIT STREAM, NİĞDE/TURKEY

A THESIS SUBMITTED TO
THE GRADUATE SCHOOL OF NATURAL AND APPLIED SCIENCES
OF
MIDDLE EAST TECHNICAL UNIVERSITY

BY

KASIMCAN KORUK

IN PARTIAL FULFILLMENT OF THE REQUIREMENTS
FOR
THE DEGREE OF MASTER OF SCIENCE
IN
GEOLOGICAL ENGINEERING

JUNE 2019

Approval of the thesis:

A MULTI-TECHNIQUE APPROACH TO DETERMINE TEMPORAL AND SPATIAL VARIABILITY OF GROUNDWATER-STREAM WATER EXCHANGE IN ÇAKIT STREAM, NİĞDE/TURKEY

submitted by **KASIMCAN KORUK** in partial fulfillment of the requirements for the degree of **Master of Science in Geological Engineering Department, Middle East Technical University** by,

Prof. Dr. Halil Kalıpçılar
Dean, Graduate School of **Natural and Applied Sciences**　　　_____

Prof. Dr. Erdin Bozkurt
Head of Department, **Geological Engineering**　　　_____

Assoc. Prof. Dr. Koray Kamil Yılmaz
Supervisor, **Geological Engineering, METU**　　　_____

Examining Committee Members:

Prof. Dr. Hasan Yazıcıgil
Geological Engineering, METU　　　_____

Assoc. Prof. Dr. Koray Kamil Yılmaz
Geological Engineering, METU　　　_____

Prof. Dr. Zuhal Akyürek
Civil Engineering, METU　　　_____

Prof. Dr. İsmail Yücel
Civil Engineering, METU　　　_____

Assoc. Prof. Dr. Harun Aydın
Environmental Eng., Van Yüzüncü Yıl Uni.　　　_____

Date: 17.06.2019

I hereby declare that all information in this document has been obtained and presented in accordance with academic rules and ethical conduct. I also declare that, as required by these rules and conduct, I have fully cited and referenced all material and results that are not original to this work.

Name, Surname: Kasımcan Koruk

Signature:

ABSTRACT

A MULTI-TECHNIQUE APPROACH TO DETERMINE TEMPORAL AND SPATIAL VARIABILITY OF GROUNDWATER-STREAM WATER EXCHANGE IN ÇAKIT STREAM, NİĞDE/TURKEY

Koruk, Kasımcan
Master of Science, Geological Engineering
Supervisor: Assoc. Prof. Dr. Koray Kamil Yılmaz

June 2019, 111 pages

Characterizing the spatio-temporal distribution of groundwater-surface water exchange fluxes are of paramount importance in understanding catchment behavior. The objective of this study is to quantify the spatio-temporal distribution of the exchange fluxes along the Çakıt Stream (Niğde, Turkey) through coupling a set of geophysical techniques and in-stream measurements in a hierarchical manner. First, geological and water quality information were combined at the regional scale to determine the focus area at the reach-scale. Second, Electromagnetic Induction (EMI) surveys were conducted over the determined reach of stream to pinpoint potential groundwater upwelling locations along the streambed. EMI anomalies guided our focus to a 600 meter-long reach of the stream. Along this selected reach, Fiber-Optic Distributed Temperature Sensing System (FO-DTS) was utilized to investigate top-of-the-streambed-temperature profiles at fine spatial and temporal scales. Furthermore, vertical hydraulic gradients and exchange fluxes were investigated at three potential locations using nested piezometers and vertical temperature profiles, respectively. Water quality parameters were also measured along the reach in surface water and in the piezometers. Results of these studies indicated that study reach has heterogeneities in terms of vertical water-flow components with seasonal transitions.

EMI survey was successful in identifying a groundwater upwelling location with relatively high anomaly. FO-DTS measurements also indicated high temperature anomaly during cold air temperature and low flow conditions at the same upwelling site. Finally, point-based traditional methods supported the observations of EMI and FO-DTS quantitatively.

Keywords: Groundwater – Surface water interaction, EMI, FO-DTS, Streambed Vertical Temperature Profiles, Nested-Piezometers.

ÖZ

ÇAKIT DERESİ, NİĞDE/TÜRKİYE'DE YERALTI-YÜZEY SUYU ETKİLEŞİMİNDE DEĞİŞKENLİKLERİN ZAMANSAL VE MEKANSAL OLARAK BELİRLENMESİ ADINA ÇOK TEKNİKLİ BİR UYGULAMA

Koruk, Kasımcan
Yüksek Lisans, Jeoloji Mühendisliği
Tez Danışmanı: Doç. Dr. Koray Kamil Yılmaz

Haziran 2019, 111 sayfa

Havza hidrolojisinde yeraltı-yüzeysuyu akış etkileşiminin zamansal ve mekansal dağılımını anlamak büyük önem arz etmektedir. Bu çalışmanın amacı jeofiziksel teknikleri ve nehiriçi ölçümleri hiyerarşik düzende uygulayarak Çakıt Deresi'ndeki (Niğde, Türkiye) yeraltı-yüzeysuyu akış etkileşimini belirlemektir.. İlk olarak, Çakıt Deresi üzerinde detaylı çalışma yapılacak kısım daha önce havza boyunca gerçekleştirilen anyon-katyon analizi ve mevcut jeolojik bilgiler kullanılarak belirlendi. Daha sonra, Çakıt Deresi'nin seçilen kısmında elektromanyetik indüksiyon (EMI) çalışması potansiyel yeraltısuyu çıkış noktalarını belirlemek amacıyla gerçekleştirildi. EMI çalışmasından elde edilen anomaliler çalışmanın 600 metre uzunluğundaki nehir yatağına odaklanmasına yardımcı oldu. Belirlenen bu nehir yatağı boyunca, fiber-optik dağıtımlı sıcaklık algılama teknolojisi (Distributed Temperature Sensing – DTS) kullanılarak zamansal ve mekansal olarak detaylı ölçekte nehir yatağı yüzeyi sıcaklık profili incelendi.

Ayrıca, dikey hidrolik eğim ve dikey akış, sırasıyla, yan yana piyezometreler ve dikey sıcaklık profilleri kullanılarak üç potansiyel noktada incelenmiştir. Yüzey suyunda ve piyezometrelerde su kalitesi parametreleri ölçüldü. Çalışmaların sonuçları, araştırma

yapılan nehir yatağı bölümünde yeraltı ve yüzeysuyu arasında dikey su akışı bileşenlerinin mevsimsel ve mekânsal heterojenliğe sahip olduğunu göstermiştir. EMI araştırması, nispeten yüksek anomalili bir yeraltısuyu etkileşiminin olduğu yerin tespitinde başarılı olmuştur. FO-DTS ölçümleri, soğuk hava sıcaklığı ve düşük akım koşullarında EMI ölçümlerini destekleyici yüksek sıcaklık anomalisi vermiştir. Son olarak, noktasal geleneksel yöntemler EMI ve FO-DTS gözlemlerini desteklemiştir.

Anahtar Kelimeler: Yeraltı-Yüzeysuyu Etkileşimi, EMI, FO-DTS, Dereyatağı Dikey Sıcaklık Profilleri, Yanyana Piyezometreler.

To My Family

ACKNOWLEDGEMENTS

TABLE OF CONTENTS

LIST OF TABLES

TABLES

LIST OF FIGURES

FIGURES

xvii

xviii

LIST OF ABBREVIATIONS

ABBREVIATIONS

CMD	Electromagnetic Conductivity Meter
DSİ	General Directorate of State Hydraulic Works
EC	Electrical Conductivity
EMI	Electromagnetic Induction Survey
FO-DTS	Fiber-Optic Distributed Temperature Sensing Technology
GW-SW	Groundwater-Surface Water
MTA	General Directorate of Mineral Research and Exploration
TUBITAK	Scientific and Technological Research Council of Turkey
VHG	Vertical Hydraulic Gradient
WFD	European Union Water Frame Directive

CHAPTER 1

INTRODUCTION

1.1. Groundwater-Surface Water Interaction

In recent years, irregularities in use of the water resources have increased due to developed technology, urbanization and industrialization, and hence management and protection of water sources have been better perceived in time. Many developed civilizations especially Europe have taken precautions against water pollution, and they have funded high amounts of economic budgets in order to supply the increasing clean water demands. The supply of high amount of clean water resources necessitates scientific studies, and hence this need has led the regarding scientific studies to be supported by developed civilizations. The support of scientific studies has increased ever since European Union Water Framework Directive (WFD) was released to make legal regulations for the management of water resources. WFD is a legislation that has the aim to protect all sort of water bodies, and to form a set of standards for water resources. The WFD standards are tended to reach the highest possible properties of both quantitative and chemical in water resources like surface waters, groundwater and coastal waters. Today, it has been well understood that water bodies like rivers, lakes and wetlands are parts of hydrological cycle, and they are hydraulically connected to groundwater partially or totally (Winter et al., 1998). Therefore, scientific studies give utmost importance to the groundwater-surface water (GW-SW) interaction to manage water resources efficiently considering chemical, physical and biological standards, and groundwater and surface water are investigated as a whole (Winter et al., 1998; Sophocleous, 2002).

Interaction between groundwater and surface water causes an exchange of water in a continuous manner. Chemical, physical and biological properties of groundwater and

surface water can change when the exchange occurs since they possess different properties (Kalbus et al., 2006). Transportation, degradation, precipitation, and sorption can be considered as some of the exchange processes that take place between groundwater and surface water affecting the chemical, physical and surface water properties. In other words, water quality properties are affected by the interaction of GW-SW. Water quality properties of a stream or a lake fed by groundwater can be dependent on the groundwater conditions based on the amount of interaction. Level of contaminant in a water body can be regulated by implementing a remediation process on regions where GW-SW interaction is a strong controlling factor. GW-SW interaction can also affect aquatic life in both contaminated and uncontaminated areas (Brunke and Gonser, 1997). Therefore, understanding the mechanism of GW-SW interaction can also provide strong foresight on the hydro-biochemistry studies (Schmidt et al., 2006). Beside water management and water ecology, understanding GW-SW interaction is also important in terms of water supply. Excessive use of either groundwater or surface water can affect the other, and this can be resulted with depletion of water resources (Winter et al., 1998). Therefore, GW-SW interaction cannot be denied in water budget studies. Considering all the facts explained above, it can be said that GW-SW interaction is the key to understand all types of water resources studies.

1.2. Objective

The objective of this study is to quantify the spatio-temporal distribution of the exchange fluxes along the long reaches of Çakıt Stream near Hasangazi Village located in the vicinity of Ulukışla/Niğde, south of Central Anatolia, Turkey. The study was conducted from a large basin scale to small stream reach scale. The relation between geology and water quality were investigated on basin scale to understand aquifer systems, and a general characteristic of the basin was described combining the information of geology, water quality measurements and reach-scale quantified exchange fluxes.

1.3. Approach

The study was conducted through coupling a set of geophysical techniques and in-stream measurements in a hierarchical manner in order to reach the objective of the study. First, general information was gathered together over the basin with the help of geological information and previously performed anion-cation analyses of which samples had been collected from all over the river network of the basin. By the help of the information available, an approximately 2-km long reach was determined, and potential permeable streambed locations were determined using a geophysical instrument. Then, temperature-based measurements and physical measurements were performed on smaller reaches of the determined reach to quantify the exchange fluxes of the streambed. The hierarchical methodology of the study is defined as follows:

(1) Understanding the general characteristics of the basin aquifer systems by combining the geological information and the major ion analyses of which samples had been collected from all over the river network of the basin.

(2) Application of handheld Electromagnetic Induction (EMI) Surveys on long reaches of Çakıt Stream to detect porous streambed sediment locations and local permeable streambed zones, and hence potential exchange flux zones.

(3) Collecting temperature transect data along a certain reach of the stream using Distributed Temperature Sensing (DTS) Technology to catch the temperature anomalies at locations where groundwater upwelling occurs.

(4) Installation of nested piezometers to determine vertical hydraulic gradient at potential upwelling locations within the streambed.

(5) Installation of iButton Temperature Loggers to obtain streambed vertical temperature profiles and hence temperature based vertical water flux estimation at potential groundwater upwelling locations.

(6) Analyses of water quality measurements (temperature and electrical conductivity) recorded from surface water, groundwater, and analysis of hydrochemical facies.

CHAPTER 2

BACKGROUND LITERATURE

2.1. Groundwater-Stream Water Interaction

Surface waters, such as streams, and groundwater are hydraulically interconnected components of the hydrologic cycle. The interconnection between groundwater and stream water can affect the water quality properties and its' distribution at benthic and hyporheic zone within the streambed (Brunke and Gonser, 1997; Winter et al., 1998). The interaction between groundwater and surface water can take place in three scales of flow systems as described by Tóth (1963): local, intermediate, and regional (Figure 2.1). While the time required for water exchange in local flow systems takes days, this can change up to hundreds of years for regional flow systems. Local flow systems can be considered as the most dynamic and shallowest systems since they flow from a high recharge location to a nearby lowland at scales of a few meters. Due to their higher mobility compared to intermediate and regional flow systems, local flow systems can be vulnerable to human-based contamination (Winter et al., 1998). Local flow systems can be underlain by intermediate and regional flow systems. Groundwater flows much longer distances through intermediate and regional flow systems and hence can contain more dissolved chemicals and solids, which in turn can affect water quality properties of surface waters.
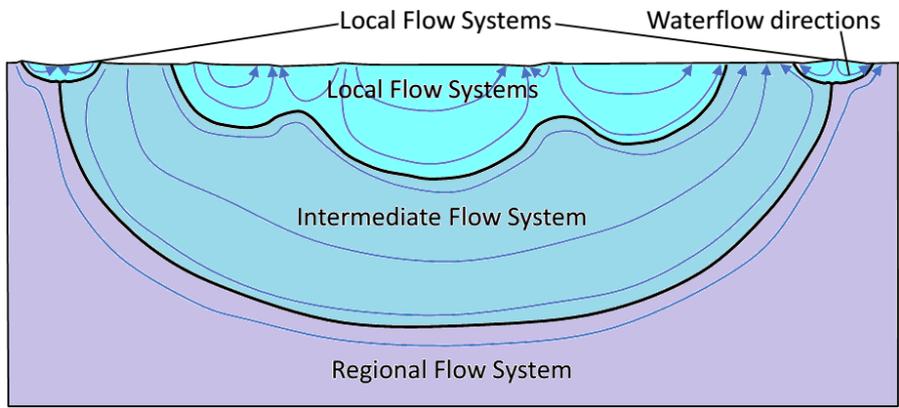
Figure 2.1. Groundwater flow systems (Reillustrated from Tóth, 1963)

Basically, groundwater-stream water (GW-SW) interaction can occur in three different ways: gaining streams where inflow of groundwater to streams is dominant (Figure 2.2a), losing streams where recharge of stream to groundwater is dominant (Figure 2.2b), or gaining and losing stream can both occur together. If the stream is disconnected by the unsaturated zone water table may upheave just beneath the stream with the effect of downwelling water fluxes, and this case is defined as disconnected stream (Figure 2.2c).
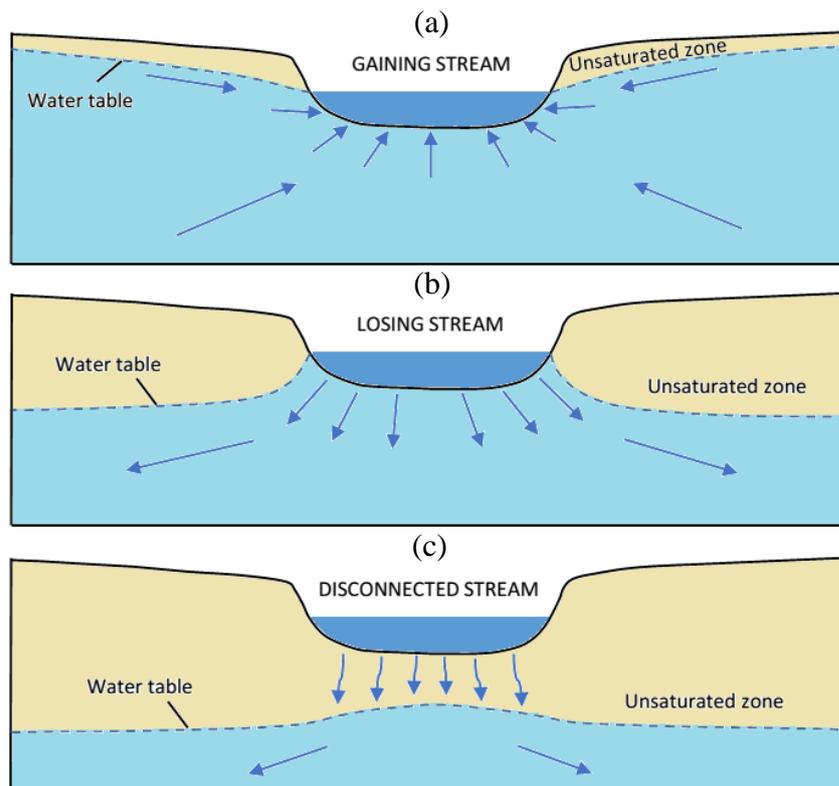
Figure 2.2. Two dimensional visualization of GW-SW interaction types
(Reillustrated from Winter et al., 1998)

The interaction between GW-SW can be controlled by different factors including geology, geomorphology, topography and climate (Sophocleous, 2002). Geological formations and units can affect the rate of GW-SW interaction. Streambed geometry can be shaped under the effect of geomorphology and topography, and an implication of the GW-SW interaction can be inferred from the information of geomorphology and topography. Rate of precipitation can affect the position of the water table, and stream water gain inflow from groundwater or vice versa based on the geometry of water table. Gaining or losing inflow conditions of stream water depend on the level of water table which may vary at local scales.

The GW-SW interaction and exchange take place mostly in hyporheic zone of the streams (Figure 2.3). Hyporheic zone can be described as saturated porous zone

7

between groundwater and stream water where the active mixing of groundwater and stream water occurs (Krause et al., 2009). Past studies have shown that hyporheic zones have high rate of local heterogeneities (Sophocleous, 2002; Kennedy et al., 2009; Malcolm et al., 2003; Binley et al., 2013). The local heterogeneities with high permeability zones were defined as "preferential discharge locations" by Conant (2004). Hence detection of these highly permeable preferential discharge locations can provide strong insights into the studies related groundwater surface water exchange.
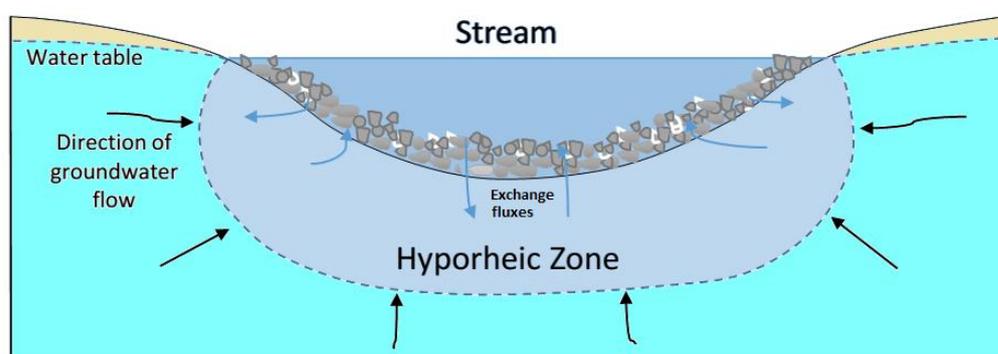
Figure 2.3. Hyporheic zone and GW-SW interaction (Reillustrated from Winter et al., 1998)

2.2. Hydrochemistry of Groundwater and Stream Water

Water can host dissolved solids, inorganic and organic substances, and organisms since it has highly dynamic form and reactive nature. Geology has an important control on the hydrochemistry of both surface waters and groundwater. Dissolved solids in water can provide information on their geologic history, its influence on soil or their mode of origin within the hydrologic cycle (Freeze and Cherry, 1979). Lithology of the surface and subsurface, where the water is in contact, can affect the physical and chemical characteristics of groundwater and surface water with dissolution of minerals (Candela and Morell, 2009). Hydrochemical composition of surface waters differs from groundwater. The states of substances in streams can be

dissolved, suspended, or deposited. Dissolved solids found in streams mainly come from groundwater, surface runoff and precipitation that drained through soil. Since chemical composition of groundwater and precipitation are different from that of surface water, interaction between GW-SW and events of precipitation may affect hydrochemical status of surface waters.

Generally, the amount of dissolved solids in groundwater is less than 1000 mg/L unless groundwater has (1) in contact with highly soluble minerals like gypsum, (2) been concentrated by evapotranspiration, and (3) been heated by geothermal sources (Todd and Mays, 2005). While there are several types of ions available in water, only a few of ions are greater than 1 mg/L, and these ions are defined as major ions. Ions whose amounts in the water are less than 1 mg/L and higher than 0.01 mg/L can be defined as minor ions, and those less than 0.01 mg/L are named as trace ions. Major ions available in natural waters can be classified as cations, which are calcium (Ca^{2+}), sodium (Na^+), magnesium (Mg^{2+}), potassium (K^+), and anions, which are chlorine (Cl^-), carbonate (CO_3^{2-}), bicarbonate (HCO_3^-) and sulfate (SO_4^{2-}). The amount of some ions in waters like fluorine (F^-), nitrite (NO_2^-) and nitrate (NO_3^-) can also be as high as major ions due to anthropogenic contamination.

Major ion evolution was concluded by Chebotarev (1955). Chebotarev (1955) concluded that chemical composition of groundwater tends to evolve towards that of seawater. The idea of major ion evolution was described by Domenico (1972) for large sedimentary basins in terms of three zones correlated with depth:

(1) Upper zone which is characterized by active groundwater flushing through relatively well-leached rocks. HCO_3^- is the dominant anion in this zone, and amount of dissolved solids is low compared to others.

(2) Intermediate zone which is characterized by less active groundwater flow compared to upper zone, and higher amount of total dissolved solids exists in this zone with high SO_4^{2-} content as dominant anion.

(3) Lower zone which is characterized by slow groundwater flow, and high amount of Cl^- content is the characteristics of this zone since less groundwater flushing causes deposition of soluble matters in this zone.

The description proposed by Domenico (1972) is only applicable for the basins with simple geology, and it cannot be decisive for basins having complex geology. As an example for simple geology, presence of HCO_3^- in stream water can be attributed to presence of calcite ($CaCO_3$) and dolomite ($CaMg(CO_3)_2$) in shallow soils where shallow aquifer interaction takes place. Note that availability of CO_2^- in shallow soils makes groundwater slightly acidic and in turn dissolves calcite and dolomite. Presence of SO_4^{2-} can be attributed to gypsum mineral ($CaSO_4 \cdot 2H_2O$) and anhydrite ($CaSO_4$). SO_4^{2-} is attributed to intermediate zone due to the fact that minerals like gypsum and anhydrite is highly soluble matters, and they mostly are flushed from shallow zones by groundwater to deeper zones unless the topography has a complex geology. Presence of Cl^- ion can be attributed to halite ($NaCl$) and sylvite (KCl) minerals. Normally, halite and sylvite forms under evaporitic closed marine or lake conditions million years ago, and they are only preserved under deep groundwater since chloride has the highest potential of solubility. Therefore, groundwater having Cl^- can be accounted to follow long flow path systems for sedimentary basins with simple geology. When halite and sylvite minerals exist in the strata, in which groundwater flows through, it can be said that hydrochemical facies of the water can evolve to Cl^- ion, and Cl^- ion is only expected to be trace ion in the strata of siltstone, shale, limestone and dolomite (Freeze and Cherry, 1979).

2.3. Measuring Methods for Exchange Fluxes of Groundwater-Stream Water

As it was emphasized previously, understanding the mechanism of interaction between groundwater and surface water can provide important foresight on studies of water management and water quality. For this purpose, several studies have been performed and new methods and technologies have been adopted to determine the GW-SW interaction processes and fluxes. Traditionally, hydraulic head estimations,

darcian flux estimations, streamflow discharge calculations, seepage calculations, environmental tracers, temperature monitoring and geophysical applications have been used to determine the GW-SW interaction (Kalbus et al., 2006). Using methods that are appropriate for the space and time scales of the exchange process is of paramount importance. While single methods can be insufficient to quantify GW-SW interaction, combining methods at multiple scales can fulfil ambiguities and has the potential to give robust results. Moreover, methods based on measurements of piezometers and seepage meters provide robust results at point scale, yet they may be inadequate to represent heterogeneities at the reach scale (Briggs et al., 2012; Kalbus et al., 2006). Therefore, multi-scale datasets spanning both time and space can be combined with robust point data to yield a better insight into the groundwater – surface water exchange.

The methods for measurement of exchange fluxes are further explained below under the subjects of non-thermal, thermal and geophysical methods.

2.3.1. Non-Thermal Methods to Determine Groundwater-Stream Water Exchange Fluxes

Hydraulic head measurement is a valid method for years. Piezometers which are made of pipes have been used to measure hydraulic head in many studies (Lee and Cherry, 1978; Conant, 2004) Hydraulic heads measured from nested piezometers which are installed into two different streambed depths can be used to calculate vertical hydraulic gradient. From two or more piezometers installed into the same depth, lateral or horizontal hydraulic gradient and hence groundwater movement direction can be estimated (Kalbus et al., 2006). Baxter et al., (2003) described how to install a piezometer mechanically into streambed. Lately, drill machines have also been used to install piezometers efficiently in harsh streambed conditions [e.g., Binley et al., 2013].

Darcian flux estimation is the method derived from Darcy equation (Darcy, 1856). Specific discharge of a fluid (q) can be estimated with a simple equation. In order to

calculate q, the equation requires two main variables: hydraulic conductivity (K), and hydraulic gradient (second term on right hand side).

$$q = -K\frac{dh}{dl}$$ (1)

where, dh is change in hydraulic head and dl is change in length. While hydraulic gradient estimation can be performed with simple piezometers, hydraulic conductivity requires field tests such as slug and bail tests (Hvorslev, 1951; Hyder et al., 1994) or laboratory tests such as permeameter test (Todd and Mays, 2005).

Streamflow discharge calculation is another standard method which is applied along a specific reach of a stream from two or more cross-sections of stream (Carter and Davidian, 1968; Kostaschuk et al., 2005). The method, which is also called differential stream gauging, provides a general information about the groundwater contribution along a specific river reach that has no lateral surface water inflow. The difference between two adjacent stream discharge measurements should be much higher than the uncertainties inherent in this method in order to obtain a reliable result (Kalbus et al., 2006).

Seepage meters, first designed by Lee (1977), are used to measure amount of seepage at a point within the streambed over a fix time period, and have been used by many researchers [e.g., Lee and Hynes, 1978; Landon et al., 2001]. Lately, automated versions of seepage meters have been designed so that change of seepage variations in time could be monitored [e.g., Rosenbarry, 2008].

Environmental tracers can be used to identify discharge and recharge zones of groundwater on small reaches of river (Kalbus et al., 2006). Use of major ions in hydrograph separation [e.g., Covino and McGlynn, 2007], stable isotopes of Oxygen-18 and Deuterium [e.g., Lambs, 2004], electrical conductivity [e.g., Schmidt et al. 2012], radioactive isotope radon-222 [e.g., Martinez et al. 2015], radioactive isotope of chlorine-36 [e.g., Shaw et al. 2014] are some of the environmental tracer - based

methods which are widely used in recent studies. A marked difference in chemical properties of water can occur with the inflow of an old water source or waters flowing from long distances to the hyporheic zone, and environmental tracers can be used to detect this difference (Shaw et al., 2014). Use of major ions in hydrograph separation is a powerful and widely used technique to determine different source of influxes to streams (McGlynn and McDonnell, 2003). Using conservative ions, a quantitative solution can be proposed to determine the amount of GW-SW interaction along the long reaches of streams. The techniques of stable isotopes and radioactive isotopes are based on the determination of naturally occurring geochemical variations in waters. Electrical conductivity measurements are employed in hydrological studies relying on the direct relation with the amount of total dissolved solid in waters. Lastly, it is important to notice that environmental tracers can have different limitations, and therefore combining multiple tracers can be more effective compared to single tracer (Cox et al., 2007).

2.3.2. Thermal Methods to Determine Groundwater-Stream Water Exchange Fluxes

Thermal based methods rely on the idea of detection of temperature difference between groundwater and surface water. Thermal based methods are explained in two parts in terms of the spatial extent of investigation. Point-based vertical water flux estimation using vertical temperature profiles and distributed temperature sensing technology are respectively explained below with detail since it offers an investigation at fine spatial and temporal scales.

2.3.2.1. Temperature Based Vertical Water Flux Estimation

Temperature is a very useful environmental tracer for determining GW-SW interaction since there is a difference between the temperature of groundwater and surface water on daily and seasonal time scales (Anderson, 2005). The idea that using temperature as tracer has firstly arisen in 1960s with works of Suzuki (1960) which

focused on predicting water flux through saturated sediments with one dimensional analytical equation:

$$\frac{\partial T}{\partial t} = K_e \frac{\partial^2 T}{\partial z^2} - \frac{n v_f}{\Upsilon} \frac{\partial T}{\partial z} \qquad (2)$$

where T stands for soil temperature, t is time, K_e is effective thermal diffusivity, z is depth of streambed, n is sediment porosity, v_f is vertical fluid velocity and Υ is the rate of specific heat of soil to the specific heat of water. Studies of Stallman (1963) and Bredehoeft and Papaopulos (1965) have followed the study of Suzuki with some different approaches and modifications. Lapham (1989) used streambed temperature measurements to quantify vertical water flow. From then on, studies continued to focus on temperature profiles to determine GW-SW interaction (Anderson, 2005).

New analytical and numerical methods have been developed to estimate exchange fluxes from temperature time series records at two different depths [e.g., Hatch et al., 2006; Keery et al., 2007]. Estimation of vertical water flow using temperature time series data is based on the determination of amplitude and phase shift difference of diurnal temperature data cycles obtained from two different depths. While the temperature measurements obtained from shallower depths show high amount of diurnal fluctuation, the measurements obtained from deeper depths show dampened diurnal fluctuation (Figure 2.4). The amount of dampening at deep measurements vary based on the temperature difference between groundwater and surface water as well as the degree of groundwater upwelling/stream water downwelling.
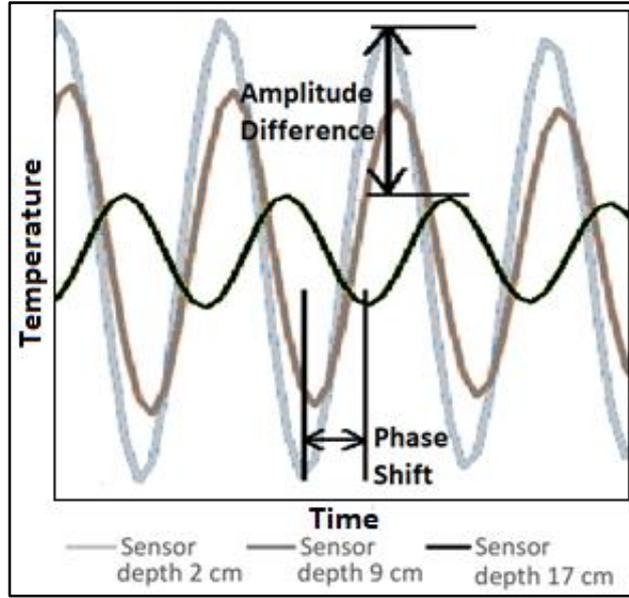
Figure 2.4. Illustration of diurnal amplitude difference and phase shift based on daily temperature recordings obtained from three different depths within the streambed

Hatch et al., (2006) offered solutions to solve the one dimensional analytical equation (2) using amplitude ratio and phase shifts under fully saturated streambed conditions. For the case of amplitude ratio the adapted solution is:

$$T(z,t) = A \, exp \left(\frac{vz}{2K_e} - \frac{z}{2K_e} \sqrt{\frac{\alpha + v^2}{2}} \right) \cos \left(\frac{2\pi t}{P} \right. $$
$$\left. - \frac{2}{2K_e} \sqrt{\frac{\alpha - v^2}{2}} \right) \tag{3}$$

where A is the amplitude of temperature variations at upper boundary, P is the period of temperature variations, v is rate of penetration of thermal front which is proportional to velocity of fluid ($v = v_f / \Upsilon$) and $\alpha = \sqrt{v^4 + (8\pi \, K_e / P)^2}$. First part of the right hand-side solution is for the dampening of amplitude of temperature

variations with depth into the streambed, whereas the second part is for the shift in phase with depth.

When equation (3) is separated into components, and first part is solved according to amplitude variations considering $A_r = A_d/A_s$ for which subscript d is standing for results obtained from deep measurements, and subscript s is of shallow measurements, and thus solution can be reduced to:

$$A_r = exp\left\{\frac{1}{2K_{e,d}K_{e,s}}\left[v\left(z_d K_{e,s} - z_s K_{e,d}\right) - \left(z_d K_{e,s}\sqrt{\frac{\alpha_d + v^2}{2}} - z_s K_{e,d}\sqrt{\frac{\alpha_s + v^2}{2}}\right)\right]\right\} \tag{4}$$

Assuming sediment properties of deep and shallow measurement points are the same, first part of the solution can be reduced to:

$$A_r = exp\left\{\frac{\Delta z}{2K_e}\left(v - \sqrt{\frac{\alpha + v^2}{2}}\right)\right\} \tag{5}$$

Finally, velocity of a thermal front can be solved when the equation (5) is rearranged:

$$v_{A_r} = \frac{2K_e}{\Delta z}lnA_r + \sqrt{\frac{\alpha + v_{A_r}{}^2}{2}} \tag{6}$$

Since velocity of a thermal front exists at both side of the equation, solution can be obtained iteratively, and thus fluid velocity can be obtained using thermal front velocity from the relationship of $v_{f,A_r} = v_{A_r}\Upsilon$.

Availability of inexpensive automated temperature sensors have eased the collection of temperature data from field (Constantz, 2008), and several automated software offering numerical solutions for the processing of temperature data have shorten the

16

time to obtain flux estimates from temperature data. For example, Gordon et al. (2012) introduced a computer program for automated calculation of the analytical solution of Hatch et al. (2006). Gordon et al. (2013) employed iButton thermochrons (temperature sensors) installed into steel rods to record vertical temperature profile of the streambed. Naranjo and Turcotte (2015) have designed a temperature profiling probe in which iButtons are employed to investigate groundwater – surface water interaction.

Although point-based water flux estimation using vertical temperature profiles offers robust results, they may require many measurements in order to clarify the exchange between groundwater and stream water along a reach similar to other point-based methods (Brodie et al., 2007). Therefore, different methods offering broader extent of investigation in terms of spatio-temporal manner have been seen necessary and more valuable for hydrological studies.

2.3.2.2. Fiber-Optic Distributed Temperature Sensing Technology

While previous works could only provide temperature measurements of point in space, Selker et al. (2006a-b) introduced and applied fiber optic distributed temperature sensing (FO-DTS) technology in the field of hydrology for the first time, and hence measurements can be performed both in time and space.

An optical fiber is a thin flexible strand of dielectric material that can trap optical radiation from starting tip to the end point (Casas and Cruz, 2003). Generally, optical fibers consists of two distinct materials; a glass core surrounded by a glass cladding which is lower in index of refraction (Merzbacher et al., 1996). Glass core material carries the light waves, and surrounding coating is used to protect this core and cladding layer. Mainly, advantages of fiber optic sensors are inherited from silica since they are passive, dielectric, having low losses at optical frequencies, and thus fiber-optic cables are immune to electromagnetic interferences, chemically inert, biocompatible, and withstand high temperature (López-Higuera et al., 2011). There are different types of commercially available fiber-optic cables which can be

employed according to different purposes. In terms of configuration, fiber-optics can be classified according to single mode and multi-mode fiber optic cables with changing fiber core size, or simplex and duplex fiber-optics according to number of fiber cores in a single cable tubes which can be served for different purposes (Deng and Cai, 2007).

Main working principle of FO-DTS is based on the detection of reactions of light source emitted through fiber optic cable (Figure 2.5). When the light source strikes matter the light may be reflected totally, which is known as Rayleigh scattering phenomenon, or a portion of light source is adsorbed and reemitted at wavelengths just above and below the frequencies of initial light source due to loss or gain of energy exchanged from electrons (Selker et al., 2006a). The loss and gain in specific frequencies of light sources is known as the Raman scattering phenomenon (Figure 2.6). In the case of FO-DTS, the light source launched through fiber-optic cable, generates non-elastic backscattering at specific frequencies greater (Stokes) and smaller (Anti-Stokes) than initial frequency of the light source because of the cable's nature (Selker et al., 2006a). Amplitudes of the backscattered light is determined at each measurement point of fiber-optic cable by the knowledge of travel time of light through the cable. While the amplitudes of Stokes are weakly dependent on temperature, amplitudes of Anti-Stokes are highly dependent on temperature changes (Selker et al., 2006a), and thus a temperature estimation can be performed by taking the ratio of amplitudes of Stokes and Anti-Stokes.
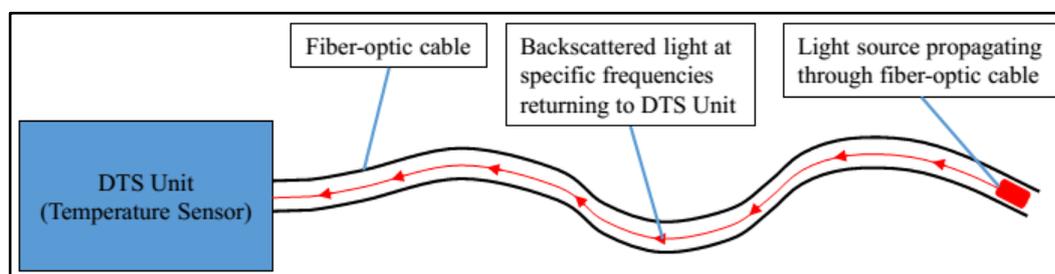
Figure 2.5. Illustration of fiber-optic distributed temperature sensing technology
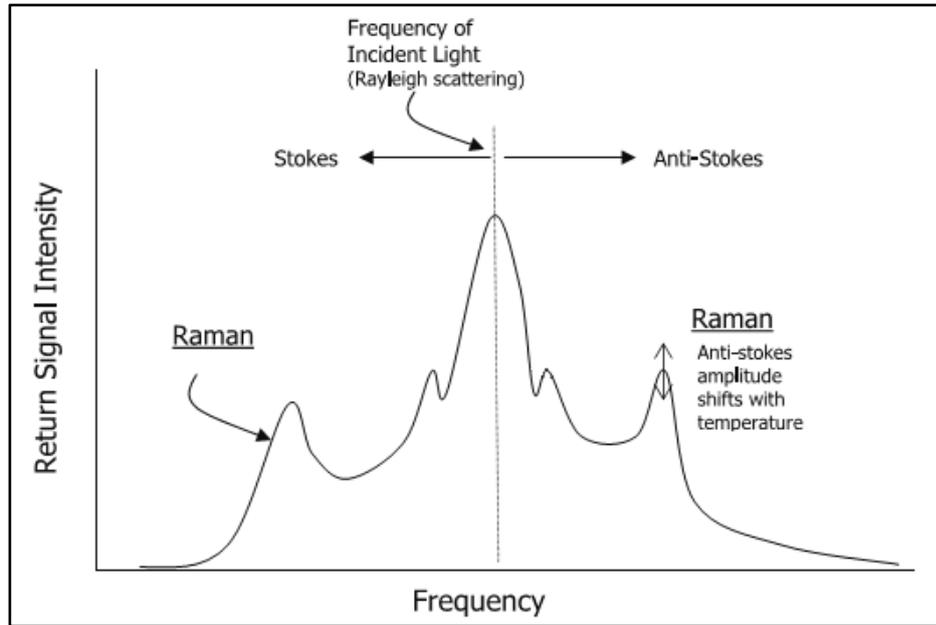
Figure 2.6. Raman backscattering of an incident light frequency (Adapted from Selker et al., 2006a)

Calibration of fiber optic cables is an important issue to get successful temperature data. Many studies have followed the guidance of Selker et al., (2006a) and offered calibration techniques and methods to apply FO-DTS [e.g., Hausner et al., 2011; Krause et al., 2012; Matheswaran et al., 2014; Van de Giesen et al., 2012]. Hausner et al., (2011) offered a single-ended calibration technique to get temperature data from a single-mode fiber-optic cable. The name "single-ended" implies that the laser source emitted from one end of the cable is extinct at the other end of the cable, and temperature results are obtained from one laser pulse. The equation proposed to estimate temperature (T) by Hausner et al., (2011) was:

$$T(z) = \frac{\Upsilon}{ln \frac{P_S(z)}{P_{aS}(z)} + C - \Delta\alpha z} \qquad (7)$$

where Υ is standing for the shift in energy between a photon at the wavelength of the incident laser and the scattered Raman photon, C is a dimensionless calibration parameter that encompasses properties of the incident laser and the FO-DTS instrument itself, and $\Delta\alpha$ is the differential attenuation between amplitudes of anti-Stokes and Stokes signal. While $P_S(z)$ and $P_{aS}(z)$, which are the power of the Raman Stokes and anti-Stokes respectively, are obtained from DTS measurements, Hausner et al., (2011) have sought to find values for Υ, C, and $\Delta\alpha$ parameters through experimental and field applications.

Later, double-ended calibration method, which can be more useful under harsh environmental conditions compared to single-ended calibration, was offered by Van de Giesen et al., (2012). The name "double-ended" implies that two laser pulses are sent from both end of the fiber-optic cable consecutively, and one temperature data is obtained from these two measurement periods by superposing two data adversely. Van de Giesen et al., (2012) used equation (7) for each forward measurement starting at z=0 and reverse measurement starting at z=L, and then a solution was offered based on the idea that $T(z) = T(L - z)$.

2.3.3. Geophysical Methods to Determine Groundwater-Stream Water Exchange Fluxes

Recently, number of geophysical methods to investigate the shallow subsurface and hydrological processes have been increased due to some restrictions on fieldwork such as the invasive sampling required for some methods are constrained in some areas, and environmental protection constraints (Binley et al., 2015). Traditionally, direct current resistivity, induced polarization, self-potential, ground penetrating radar, electromagnetic induction (EMI), seismic refraction, nuclear magnetic resonance, and microgravity methods have been employed in the field of hydrological studies (Binley et al., 2015), and they provide strong qualitative and quantitative solutions to infer local variations in streambed sediments (Crook et al., 2008).

Although geophysical methods are applicable with wide variety of vertical and horizontal survey scales in the field of hydrology (Binley et al., 2015), they can be challenging to use in harsh river conditions. In this respect, EMI technique offers a strong solution to detect local shallow streambed heterogeneities which can be employed even under harsh conditions since it is mobile and can be carried easily without great effort. Today, use of EMI surveys have been increasing in the field of hydrology [e.g., Binley et al., 2013; Rejiba et al., 2018; Gaona et al., 2019].

Main working principle of EMI technique relies on the principle that the EMI system energizes a transmitter coil oscillating current, and oscillating magnetic field is produced accordingly (Rejiba et al., 2018). Oscillating magnetic field produces a voltage response in the receiver coil which is used as a standard reference, and magnetic field oscillations experiencing a shift in amplitude and phase shift can be represented by a complex number, and then the complex number can be interpreted in terms of apparent electrical conductivity and depth of investigation (Rejiba et al., 2018). In other words, EMI system can provide an apparent electrical conductivity data over a depth as a function of separation between transmitter and receiver coil (Binley et al., 2013). Assuming the contribution of electrical conductivity at varying depths are known (McNeill, 1980), effective electrical conductivity of the streambed sediments can be estimated with the information of apparent electrical conductivity, known electrical conductivity of water column and depth of water column (Binley et al., 2013). Based on this knowledge, apparent electrical conductivity (σ_a) for a two layer model can be estimated using the formula below:

$$\sigma_a = \sigma_w\big(1 - CS(z_w)\big) + \sigma_{sb}CS(z_w) \qquad (8)$$

where σ_w is the electrical conductivity of stream water, σ_{sb} is electrical conductivity of streambed sediments, and $CS(z_w)$ is the cumulative sensitivity function proposed by McNeill (1980):

$$CS(z) = \frac{1}{\sqrt{4z^2 + 1}} \tag{9}$$

where z is the depth scaled by the coil separation. Finally, electrical conductivity of streambed sediments can be estimated from equation (8) since all the other parameters are known.

By the assumption that porosity has a positive relationship with electrical conductivity (Archie, 1942), and assuming pore water electrical conductivity varies insignificantly, effective electrical conductivity of streambed sediments can be attributed to porosity and thus permeability of streambed sediments (Binley et al., 2013). Finally, a permeable streambed can be interpreted as a high potential for GW-SW interaction zone.

Lately, Gaona et al., (2019) applied FO-DTS at a small stream reach with sandy streambed sediments, and they support the temperature data obtained from FO-DTS with EMI survey to interpret the GW-SW interaction. The study of Gaona et al., (2019) showed that combining FO-DTS and EMI can provide strong insight for hydrological studies.

CHAPTER 3

DESCRIPTION OF THE STUDY AREA

3.1. Physiography

The basin where the study carried out covers a 529 km^2 area between 34.393°-34.768° E longitudes and 37.378°-37.594° N latitudes in Niğde, south of Turkey (Figure 3.1). Access to the study area from Ankara has been provided through D750 motorway. Ulukışla town, which is located 100 km west of Adana, and 300 km south-east of Ankara, stays within the boundaries of the basin. Other villages in the boundaries of the study basin are Bayağıl, Porsuk, Hasangazi, Koçak, Kılan, Emirler, Darboğaz, Gümüşköy, Tekneçukur, Alihoca and Madenköy (Figure 3.1). Orchards, farming and related agricultural activities are the main source of economy for the villages in the study area, and irrigation is provided by streams and small reservoirs constructed around the basin. The basin is a highland region with steep slopes. Bolkar Mountains are located at south of the area reaching up to 3450 m above sea level (a.s.l.) within the basin boundaries. Main stream of the study basin is Çakıt Stream. Çakıt stream starts from western part of the study basin at around 1400 m a.s.l. elevation, and the stream flows out of the basin boundary, where the elevation is around 970 m a.s.l., along 162 km long stream path into lake area of Seyhan Dam, Adana. Other stream branches of the basin are Kılan Stream, Ganimet Stream, Darboğaz Stream (after the confluence of Kılan and Ganimet Streams) and Alihoca Stream (Figure 3.1).
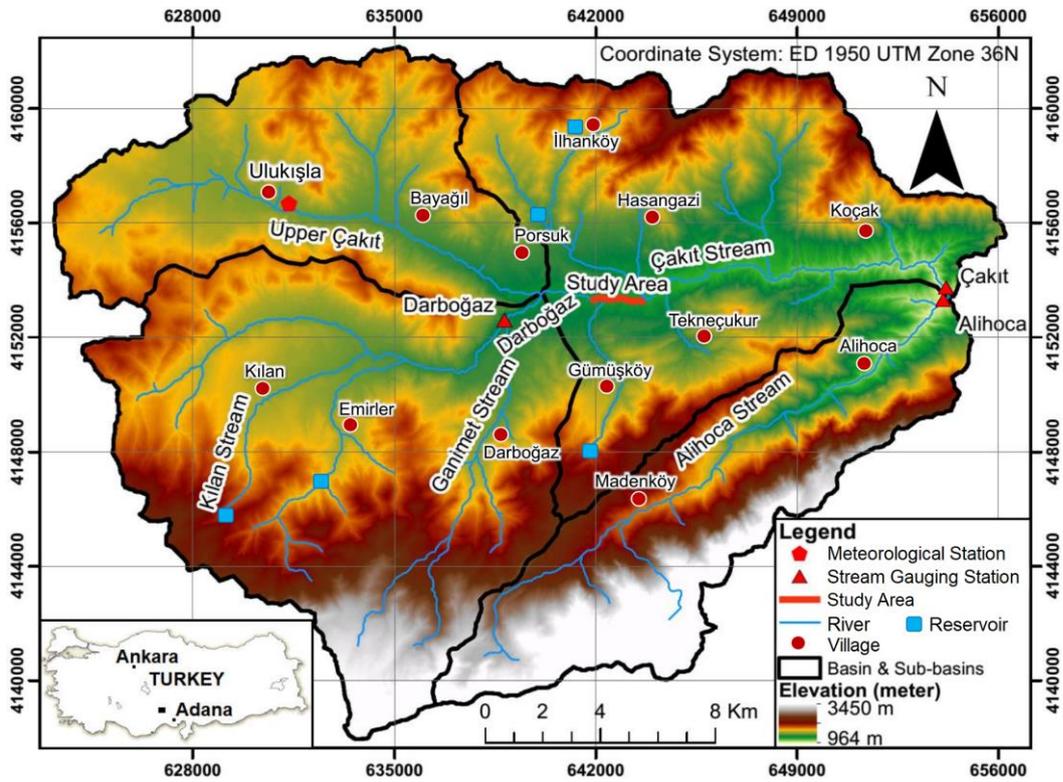
Figure 3.1. Regional view of the study basin and location of the reach-scale study area

3.2. Previous Works

The study area is a sub-basin of Seyhan Basin, Adana/Turkey. One of the most important document available for the study area is Seyhan Basin Master Plan Report (DSİ, 2016). Seyhan Basin Master Plan Report (DSİ, 2016) was previously compiled by The General Directorate of State Hydraulic Works (DSİ) within the structural adjustment and reform program for European Union WFD. Seyhan Basin Master Plan Report (DSİ, 2016) contains the issues related to conservation of natural resources such as water quality and water potential, land use condition, water demands and the methods to supply water demands within hydrological separation based basin boundaries. The information of geology and hydrogeology compiled for Seyhan Basin in Seyhan Basin Master Plan Report (DSİ, 2016) were used in regarding sub chapters.

The basin have been studied as a part of the project 115Y041 funded by TUBITAK. The project was aimed to obtain hydrological cycle parameters with a hydrological conceptual model. In the scope of the project, meteorological data such as air temperature, precipitation, wind and humidity data were obtained from Ulukışla Meteorological Station (Figure 3.1) and were gathered together. Moreover, flow gauging stations (Figure 3.1) and some other hydrological observation stations serving different purposes were constructed in the scope of the project. In June 2016, a major ion analyses were conducted to describe the origin and condition of the stream for the samples collected all over the basin as part of the project.

3.3. Climate

The climate of the study basin is characterized by continental climate. Turkish State Meteorological Service (MGM) classifies the climate of Niğde as semi-arid and mesothermal according to Thornthwaite's climate classification. From Thornthwaite's climate classification it can be inferred that the basin has without or rarely with water surplus, cold winter and warm summer climate conditions (DSİ, 2016).

Meteorological data are available which have been measured from Ulukışla meteorological station located on the west of the basin since 1937 (Figure 3.1). Mean monthly air temperatures (1937-2017) range from -1.8 °C (January) to 21.6 °C (July), with measured minimum and maximum air temperatures -21.5 °C (in February) and 37.5 °C (in July). Mean total annual precipitation is determined 343 mm from the meteorological station. Mean monthly precipitation ranges from 51.2 mm (May) to 7.3 mm (August), with measured maximum daily precipitations of months ranging from 24.3 mm (in July) to 70.2 mm (in December).

3.4. Surface Water Resources

Main stream of the basin is Çakıt Stream. Çakıt Stream starts from western hills of the basin, and discharge of the stream increases with the confluence of Kılan and Ganimet Streams from Darboğaz Stream channel (Figure 3.1). Alihoca Stream, Ganimet Stream, and Kılan Stream are originated from hillside of Bolkar Mountains, southern

boundaries of the study basin. Alihoca Stream confluences with Çakıt Stream towards the downstream end of the basin, which is the east of the study basin. Çakıt Stream is a 162 km-long stream, and it flows into the Seyhan Dam. Average river channel width of Çakıt Stream is 3.0-4.0 m. Channel widths change from place to place where topographical changes occur, and streamflow decreases at places where riffle-pool effect is observed. There are small reservoirs over the basin constructed for irrigation purposes near Darboğaz, Porsuk, İlhanköy and Kılan, and one of them is constructed for the use of gold mining activity in the south near Emirler (Figure 3.1).

There are three active stream gauging stations over the basin, one is located on the confluence point of Kılan and Ganimet Streams, and the other two are located at downstream end of the basin at Alihoca and Çakıt Stream branches (Figure 3.1). Summer baseflow conditions usually occur from July to October over the basin, and the amount of discharge starts to increase after October. Baseflow discharge amount measured at Darboğaz Stream Gauging Station was 6.5 L/s in 2017. Baseflow discharge amounts of stream gauging stations Alihoca and Çakıt, which are located at downstream end of the basin, are 10 L/s and 16 L/s, respectively. Melting snow affects Alihoca Stream more than other stream branches in the area during spring season.

3.5. Geology

3.5.1. Regional Geology

Central Anatolian Sedimentary Basins have developed through collisional and compressional tectonics (Şengör and Yılmaz, 1981). Taurus Mountains are also developed as a result of the collisional and compressional tectonics and extends along southern Turkey. The study basin is located in Ulukışla Basin (Demirtaşlı et al., 1984), which is between central Taurus Mountains and Central Anatolian Crystalline Complex. Ulukışla Basin is a foreland/Forearc or intraarc basin (Şengör and Yılmaz, 1981), and the basin developed during the period of Neo-Tethys closure (Seyitoğlu et al., 2017). Lately, Clark and Robertson (2005) proposed that Ulukışla Basin developed in an extensional or transtensional setting between Bolkar Carbonate Platform and

Niğde-Kırşehir Massif. Niğde Massif was interpreted as a Cordilleran-type core complex that developed along a detachment that has top-to NE-ENE sense of shearing, and the opening of Ulukışla Basin and the shearing along the detachment zone on the Niğde core complex were interpreted as unrelated events (Gautier et al., 2008). Finally, Seyitoğlu et al., (2017) suggested the existence of a low-angle normal fault named as İvriz detachment, located between Ulukışla Basin and Bolkar Group of Taurus Mountains (Figure 3.2).

The Central Taurus Mountains is composed of Permian-Cretaceous recrystallized limestone marble, slate and schist intercalations, which was named Bolkar Group by Demirtaşlı et al., (1984), that is considered as low-grade metamorphic rocks (Seyitoğlu et al., 2017). Bolkar Group is unconformably overlain by lower Paleocene-Lower Eocene sedimentary units (Demirtaşlı et al., 1984). Halkapınar Formation with clastic rocks, which are originated from Bolkar Group, and volcanic deposits in the Ulukışla Formation represent important parts of Upper Cretaceous-Middle Eocene basin fills (Seyitoğlu et al., 2017). Upper Eocene-Lower Oligocene gypsum and anhydrite units is named Kabaktepe Formation. Quaternary deposits settled over older units unconformably.
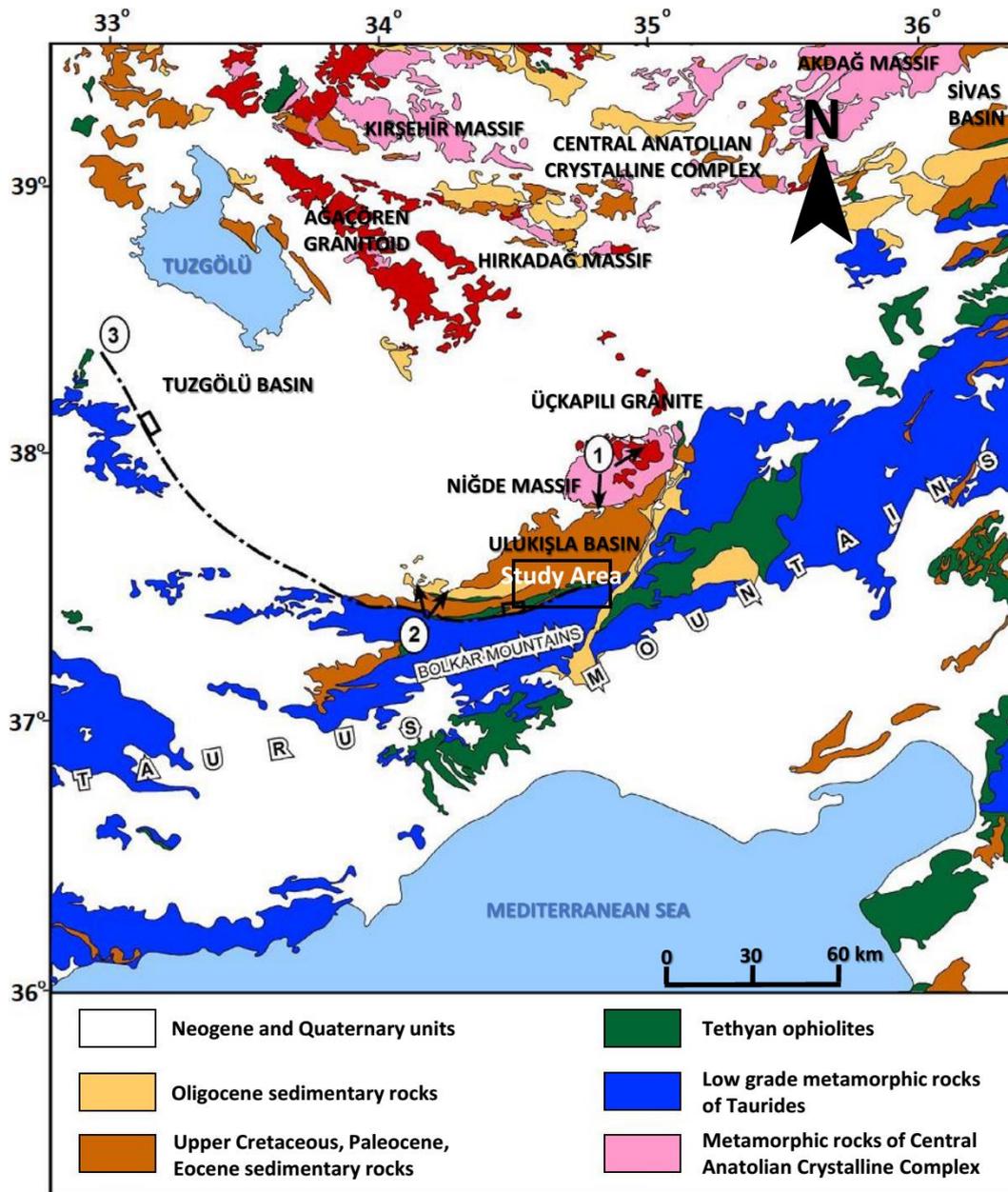
Figure 3.2. Regional geology of Middle Taurus Mountains, Ulukışla Basin and Central Anatolian Crystalline Complex (Adapted from Seyitoğlu et al., 2017). (1) Top- to-NE sense of shear on a detachment on the Niğde massif (Gautier et al., 2008), (2) top-to-N-NE sense of shear on İvriz detachment (Seyitoğlu et al., 2017), (3) Location of the Hypothetical breakaway fault (Seyitoğlu et al., 2017)

28

3.5.2. Local Geology

Southern section of the study area possesses a nappe structure, and the southern part are formed by the oldest units of the study area. Nappe structures represent the Paleozoic-Mesozoic eras, and they are mostly formed by shelf deposits and ophiolitic complex, which is composed by upper mantle and lower crust rocks representing Mesozoic oceanic lithosphere. In the middle and northern part of the study area, volcanism was active from middle Miocene to Quaternary period, and the units that have volcanic origin deposited synchronously with lacustrine and alluvial deposits.

The upper Cretaceous-Middle Eocene units are deformed by normal faults synchronously as a result of extensional tectonic regime, and the same units are overprinted by thrust faults implying that there was also contraction period following extensional tectonic regime (Seyitoğlu et al., 2017). Several folded deposits are also considered as the sign of post-middle Eocene contraction period, and having different intensity of deformation on the Upper Cretaceous-Middle Eocene units and the Upper Oligocene-Lower Miocene sequence can be attributed to existence of two contractional events during which occur in Post Middle-Eocene and Post-Oligocene times (Seyitoğlu et al., 2017).

Units exposed over surface in the study area from the oldest to the youngest units are Permian Marble Units in the south, Triassic Teknepınar Formation, Jurassic Köroğlu Formation, Cretaceous Çiftehan Formation and Ophiolitic Mélange, Paleocene Karadağ Volcanics, Halkapınar Formation, Ulukışla Formation and Çamardı Formation, Eocene Elmalı Syenite Units, Gümüş Limestone Units, Bozaltepe Formation and Dikmentepe Formation, Oligocene Kabaktepe Units, Miocene Kızıltepe travertines, and Quaternary alluvial cones, moraines and alluviums.

3.5.2.1. Marble Unit

The unit has massive shape at the bottom and medium layered with cherts towards top. The thickness of the unit is 1500 meters. The marble units are overlain by sedimentary deposits unconformably.

3.5.2.2. Teknepınar Formation

Formation is formed by gray, brown colored, thin-medium layered, and mostly pelagic origin limestone. Limestone include poorly sorted volcanic fragments in different amounts, and therefore they have flysch like appearance.

3.5.2.3. Köroğlu Formation

The units of the formation is represented by a thick carbonaceous bedding. The formation is characterized by dolomites at the bottom, dolomite-limestone intercalation at the middle part, generally medium-thick laminated, jointed, gray, black and purple colored units. Limestone shows oolitic characteristics from place to place, and upper levels of the formation have massive appearance. The formation overlies on older formations discordantly.

3.5.2.4. Çiftehan Formation

The formation is mostly composed of red colored micritic limestones, and the name of the formation was firstly given by Demirtaşlı et al., (1975). Units starting with gravel are generally overlain by thin-medium laminated, red colored pelagic limestone. The units continue with intercalation of micritic limestone basic volcanic deposits, and change to bluish gray, beige, pink colored pelagic limestone units with up to 500 meters thicknesses.

3.5.2.5. Ophiolitic Melange

Cenomanian aged complex mélange carrying ophiolites overlies Triassic-lower Cretaceous aged limestones discordantly, and they represent the ophiolitic mélange formation. The units took the form of nappe just after the deposition process, and therefore ophiolitic mélange outcrops are laid along contacts of nappe structures as banded formation.

3.5.2.6. Karadağ Volcanics

The units are comprised of intercalation of andesite-trachyte, lava, tuffites and agglomerates, and limestone lenses and intercalation of sandstone-mudstone may be included in the units.

3.5.2.7. Halkapınar Formation

Units are generally comprised of flysch like gravel, sandstone, clayey limestone, marn, spilitic lava, agglomerates and limestone blocks. Gravels form the basement of the units, and intercalation of turbiditic sandstone and shale take places towards upper levels. At younger units, olistostromes, agglomerates and large limestone olistoliths are observed. Turbiditic sandstones as basement units includes Triassic aged non-metamorphic limestone olistoliths.

3.5.2.8. Ulukışla Formation

The formation is generally comprised of shallow-deep marine sediments which is intercalated gravel, sandstone and shale units, sub-marine volcanics like agglomerates, andesitic pillow lavas and tuffites, and from place to place dikes or syenitic-monzonitic magmatites in the form of shallow intrusions. There also exists recifal limestone with inclusions of andesitic rocks in the formation. Basaltic lavas are gray, blackish brown colored, and mostly altered units. Non-altered lavas are rather solid and pores are filled by chlorite and calcite minerals, and epidotization is observable at jointed surfaces. Agglomerates are randomly aggregated depositions. Cretaceous very large olistoliths formed from pelagic limestones are settled from place to place in Ulukışla formation. Ulukışla formation overlies on older formations unconformably and again, younger formations on top of Ulukışla formation overlie unconformably.

3.5.2.9. Çamardı Formation

The units are formed by intercalation of flysch like sandstone and limestone, shale, mudstone and siltstone. Sandstones are characterized by thin-medium lamination and folded layers, and flow structures are observable at basement of beddings. There are

31

laminated siltstones and lava flows between Sandstones and clayey-sandy limestone layers. The rapid deposition of shallow marine sediments at basement, turbiditic units at middle and upper levels, existence of pelagic fauna and claystone-marn-mudstone-pillow lava intercalation can be interpreted as the formation corresponds to continental slope and continental rise.

3.5.2.10. Elmalı Monzonite-Syenite Unit

Unit can be differentiated from volcanics of Ulukışla Formation thanks to its' dirty white colored appearance. The unit has the capacity to carry ore material.

3.5.2.11. Gümüş Limestone Unit

Unit is bluish gray colored, formed by undisturbed layers, fossiliferous calcarenites and calcirudites. Facies changes can be observed laterally from limestone gravel to gravel. The thickness of the unit is approximately 50 meters.

3.5.2.12. Bozaltepe Formation

From basement to younger levels of the formation, gravel and mudstone, intercalation of turbiditic sandstone, laminated claystone and calciturbidites are observed. Interbeddings of gypsum can be observed between intercalation of turbiditic sandstone and shale at upper level of the formation. The formation starts with red colored mudstone lenses, and continues with intercalation of gravel lenses and sandstone units. Intercalation of medium-thin layered sandstone lenses, layered channel fillings and turbiditic sandstone exists toward upper levels of the formation. The thickness of the formation is 200-600 meters.

3.5.2.13. Dikmentepe Formation

The formation is characterized by massive orthoclase and pink colored trachytes.

3.5.2.14. Kabaktepe Formation

The formation is formed by gypsum and anhydrite, and sandstone, mudstone and limestone intercalation. Units start with intercalation of thin sandstone and dolomite

layers, then continues with white colored layered anhydrite units. Towards upper levels, units change to intercalation of thin-medium layered sandstone, mudstone, yellowish brown limestones and white colored anhydrite. Uppermost level of the formation is characterized by gypsum, interbedded limestone lenses and greenish gray colored marn. The thickness of the formation is approximately 750 meters.

3.5.2.15. Kızıltepe Travertines

The unit is formed by red-brown colored carbonate layers. The unit has massive and porous form. Fossils of vegetation, roots and leaf are well preserved in pores of the unit thanks to its' porous form. Lower and upper units are developed during a weathering period. The thickness of the unit is 75 meters. The unit overlies Kabaktepe units discordantly, and younger quaternary units overlie Kızıltepe travertines discordantly.

3.5.2.16. Alluvial Cone

The unit is formed by angular gravels, and sediments without a descriptive matrix.

3.5.2.17. Moraine

Aladağ Mountain region was exposed to the effect of severe glaciation during Pleistocene. Especially, north-view slopes of mountains have frequent glacial troughs. Existence of polished surfaces, horns and arêtes strengthen the idea of glacial activity. Moraines preserving the primary positions show that glacial period is rather young.

3.5.2.18. Alluvium

The unit is comprised of accumulation of loose sand, clay and mud along river valleys.
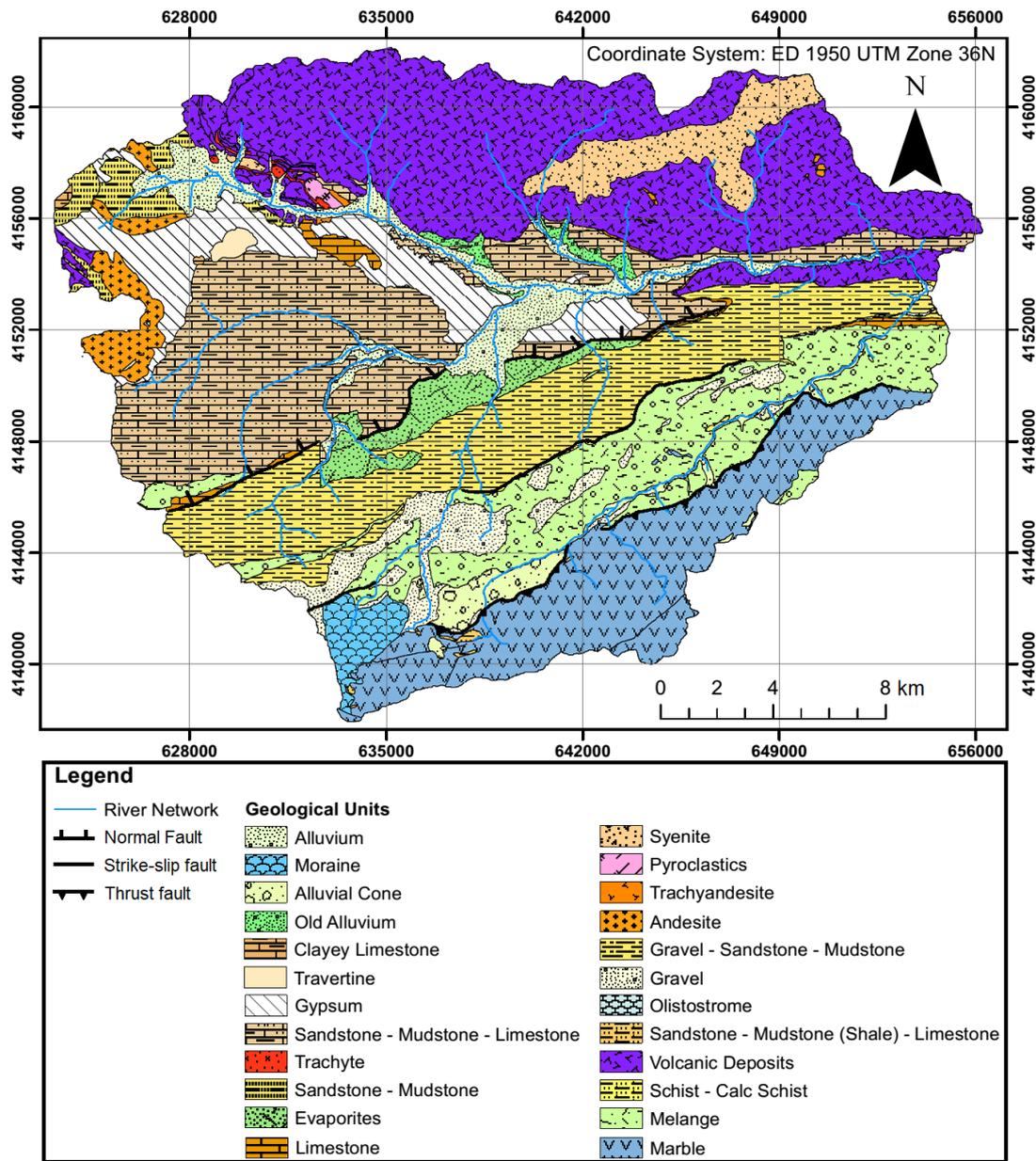
Figure 3.3. Geological map of the study area *(DSİ, 2016)*. Faults are adapted from
Seyitoğlu et al., *(2017)*.

Period / Epoch	Formation/Unit	Thickness (m)	Lithology	Description
Quaternary	Alluvium	30		Accumulation of loose sand, clay and mud along river valleys
	Moraine			Polished surfaces, horn and arete structures
	Alluvial Cone			Angular gravels, and sediments without a descriptive matrix
Miocene	Kızıltepe Travertines	75		Red-brown colored carbonate layers with massive and porous form
Oligocene	Kabaktepe Units	750		Gypsum and anhydrite, and sandstone, mudstone and limestone intercalation
Eocene	Dikmentepe Fr.			Massive orthoclase and pink colored trachytes
	Bozaltepe Fr.	200 600		Gravel, mudstone and intercalation of turbiditic sandstone, laminated claystone, calciturbidites and interbeddings of gypsum
	Gümüş Limestone	50		Bluish gray colored, undisturbed layers of fossiliferous calcarenites and calcirudites
	Elmalı Syenites			Dirty white colored syenite units
Paleocene	Karadağ Volcanics			Intercalation of andesite-trachyte, lava, tuffites and agglomerates
	Halkapınar Fr.			Flysch like gravel, sandstone, clayey limestone, marn, spilitic lava, agglomerates and limestone blocks
	Çamardı Fr.	200 900		Intercalation of sandstone and limestone, shale, mudstone and siltstone. Thin-medium laminated convoluted sandstone
	Ulukışla Fr.			Shallow-deep marine sediments, sub-marine sediments, syenitic-monzonitic magmatites, and recifal limestone with inclusions of andesitic rocks
Cretaceous	Ophiolitic Melange			Banded shape of units along contacts of nappe structures
	Çiftehan Fr.	500		Red-colored micritic limestone
Triassic	Teknepınar Fr.	350		Gray-Brown colored, mostly pelagic origin
Permian	Marble	1500		Massive shape at the bottom and medium layered with cherts at the top

Figure 3.4. Generalized columnar section of the study basin (DSİ, 2016)

35

3.6. Hydrogeology

According to Seyhan Basin Master Plan Report (DSİ, 2016), mostly Quaternary deposits show aquifer characteristics with some exceptions. Quaternary alluvium deposits in which most upstream of Çakıt Stream, Çakıt Stream and Ganimet Stream confluence together and downstream of conjunction area possess the highest aquifer properties with thicknesses up to 30-40 m. Moreover, deposits of limestone lenses in Kızıltepe Travertines, Kabaktepe Units, moraines, alluvial cones and marble units at south of the study basin show aquifer characteristics. The report calculates the total amount of water intake to Ulukışla-Pozantı sub-basin as 125.45 hm^3/year. Considering 70% secure yield, 125.45 hm^3/year water amount corresponds to 87.82 hm^3/year, and 57.24 hm^3/year of which water flows through streams, therefore 30.58 hm^3/year of the aquifer source is the amount of water reserved to common use. Currently, level of water consumption is estimated as 21.64 hm^3/year in the report and 8.94 hm^3/year is still available for common use. There are still active water wells in the study area. On the stream reach scale, alluviums, loose sands, clay and mud accumulations are the dominant streambed units. Clay and mud accumulations in the streambed generate local heterogeneities in terms of permeability and porosity. Gypsum within Kabaktepe unit increases the total dissolved solids within Çakıt stream.

CHAPTER 4

METHODS

4.1. Determination of the Location of the Reach-Scale Study Area

Major ion analyses conducted in June 2016 as a part of the TUBITAK project and the geological information were used together to determine the location of the stream reach where the spatio-temporal distribution of the GW-SW exchange fluxes will be investigated in detail. Major ion analyses were conducted to describe hydrochemical characteristics of the basin in 2016 with a total of 27 samples collected from the surface waters. The analyses of the collected samples were performed by DSİ. Table 4.1 lists the concentrations of major ions. Note that the samples are arranged according to river branches from upstream towards downstream. Moreover, color coding was used for each column to better reflect the changes ion concentrations. The major ion analysis is illustrated in the Piper diagram (Figure 4.1) and hydrochemical facies are shown in Figure 4.2. Maps in Figure 4.3-Figure 4.6 show variation in calcium, sulfate, bicarbonate concentrations and electrical conductivity over the basin, respectively.

Table 4.1. *Concentrations of major ions, total dissolved solids and electrical conductivity values for each sampling location (June, 2016) arranged in the downstream direction for each river branch*

River Branch	Sample Location	Ca (meq/L)	Mg (meq/L)	Na (meq/L)	K (meq/L)	CO₃ (meq/L)	HCO₃ (meq/L)	Cl (meq/L)	SO₄ (meq/L)	TDS (mg/L)	EC (µS/cm)
Upper Çakıt	1	19.86	3.29	2.50	0.27	0.00	6.32	2.30	16.80	1495.44	2232
	2	18.51	4.05	2.19	0.03	0.00	5.77	2.15	16.60	1207.34	1802
	3	14.59	2.81	1.76	0.02	0.00	5.22	1.44	12.06	975.52	1456
	4	16.53	2.91	1.88	0.03	0.00	4.91	1.43	15.04	1072.67	1601
Kılan	5	3.79	3.38	1.13	0.05	0.00	6.52	0.44	0.79	452.25	675
	6	5.28	3.43	1.04	0.03	0.00	5.60	0.40	3.33	528.63	789
	7	3.95	2.31	0.53	0.03	0.66	3.75	0.23	1.86	371.18	554
	8	3.98	2.46	0.56	0.04	0.82	3.39	0.24	1.99	370.51	553
Ganimet	9	2.11	1.54	0.20	0.02	0.00	3.80	0.12	0.39	248.57	371
Darboğaz	10	2.73	1.61	0.23	0.02	0.48	3.31	0.12	0.52	257.28	384
	11	3.21	1.97	0.37	0.03	0.66	3.23	0.21	1.20	304.85	455
Çakıt	12	4.67	2.18	0.50	0.03	0.00	4.10	0.28	2.72	406.69	607
	13	4.93	2.19	0.45	0.03	0.66	4.13	0.27	2.97	418.08	624
	14	6.76	2.61	0.63	0.04	0.48	4.87	0.28	4.82	440.86	658
	15	7.85	2.82	0.71	0.03	0.00	4.68	0.47	5.43	607.69	907
	16	7.59	2.77	0.75	0.03	0.82	4.61	0.48	5.44	615.06	918
	17	7.86	3.00	0.82	0.03	0.00	4.68	0.48	5.85	635.83	949
	18	8.01	2.89	0.83	0.03	0.66	4.60	0.48	5.99	641.19	957
	19	7.55	2.76	0.86	0.04	0.00	4.47	0.50	5.76	626.45	935
	20	6.82	2.73	0.88	0.03	0.00	3.95	0.37	5.86	596.97	891
	21	6.59	2.73	0.86	0.03	0.00	3.76	0.37	5.84	586.25	875
	22	5.95	2.56	0.77	0.03	0.00	3.61	0.35	5.05	539.35	805
Alihoca	23	2.11	1.26	0.06	0.01	0.41	3.11	0.10	0.21	199.66	298
	24	2.05	1.25	0.06	0.01	0.24	3.14	0.10	0.22	197.11	294
	25	2.19	1.40	0.07	0.01	0.30	3.18	0.11	0.24	217.75	325
	26	2.24	1.45	0.08	0.01	0.32	3.29	0.11	0.25	211.05	315
	27	2.27	1.51	0.10	0.02	0.33	3.49	0.11	0.26	226.46	338
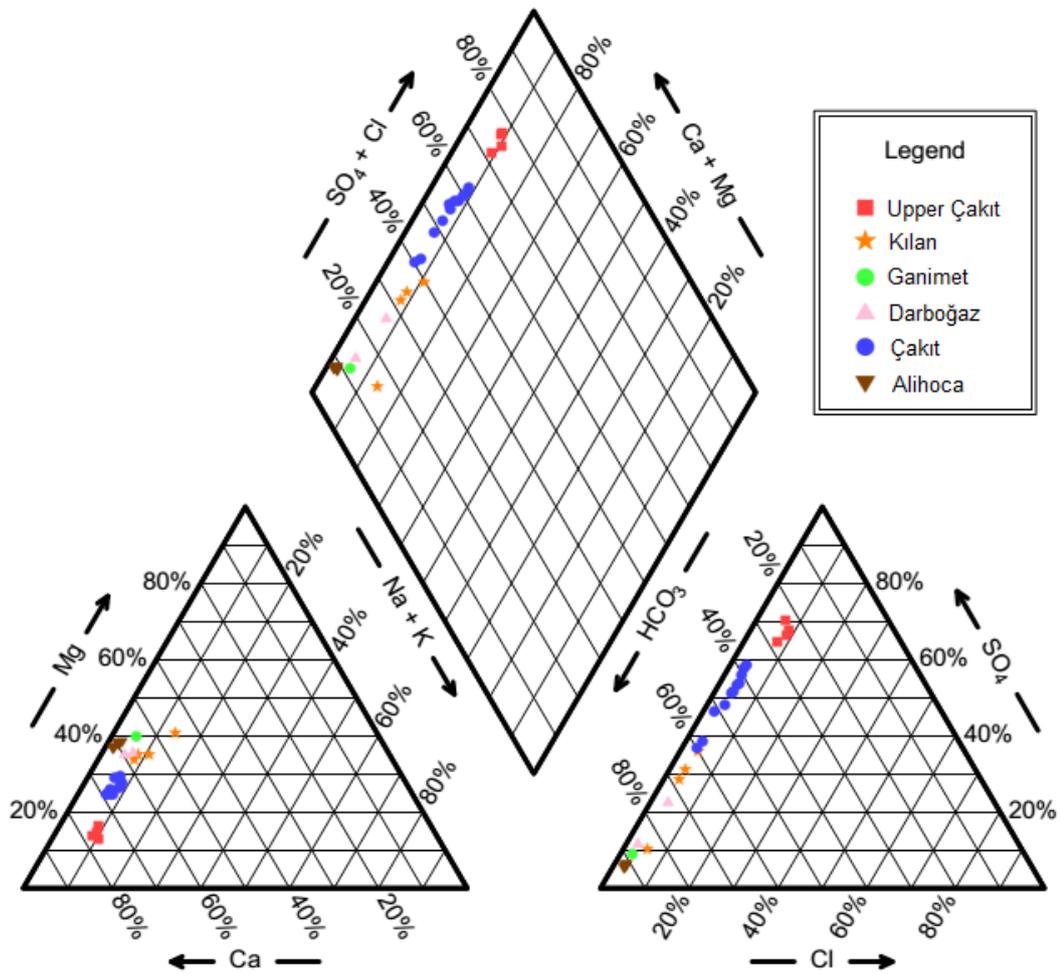
Figure 4.1. Piper diagram showing ionic composition of samples collected on June, 2016
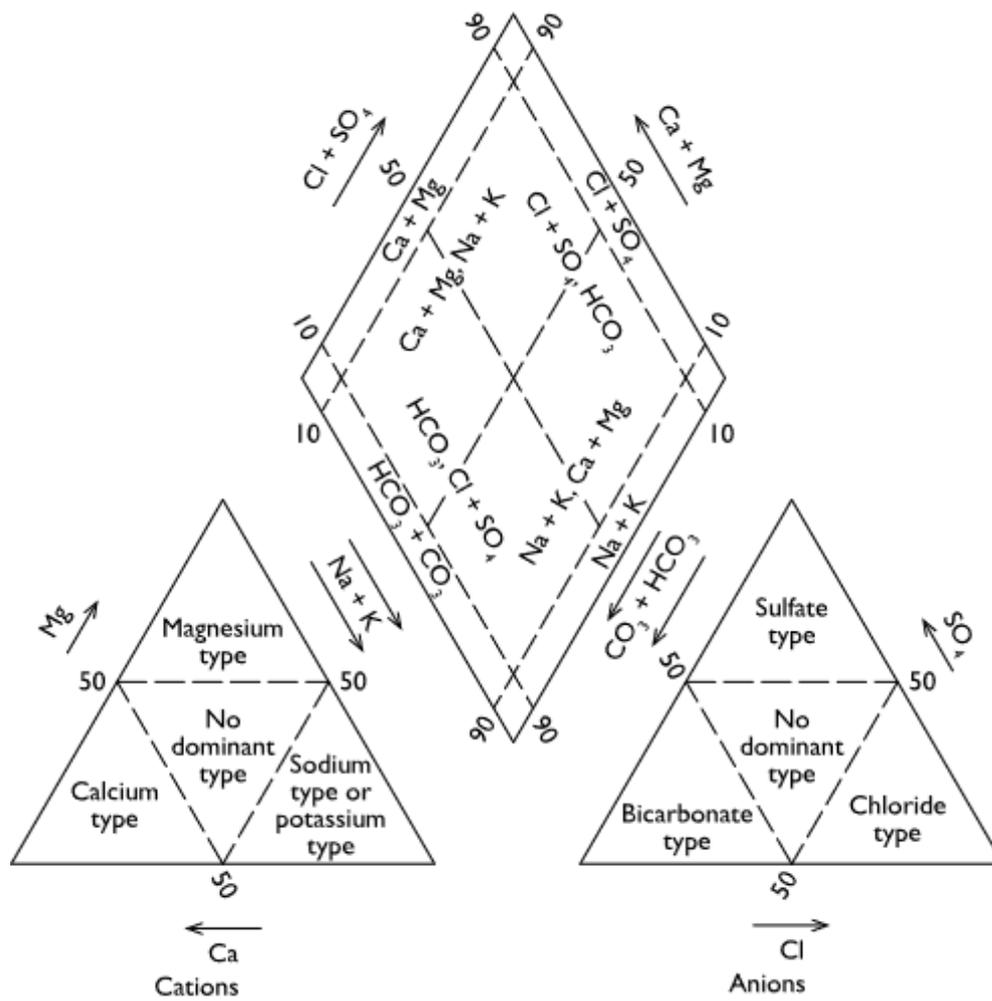
Figure 4.2. Types of hydrochemical facies according to piper diagram
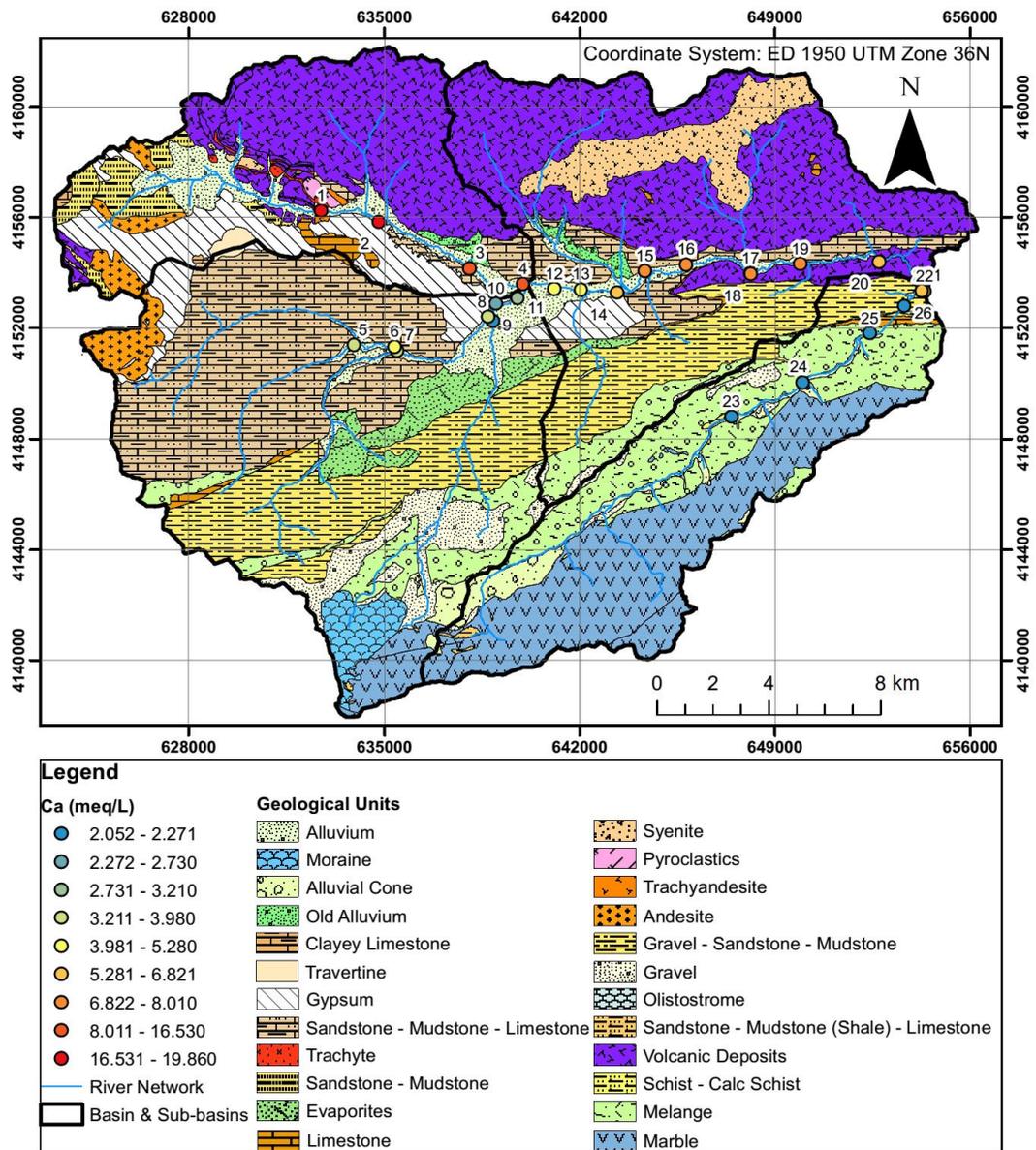
Figure 4.3. Sample classification according to calcium (Ca^{2+}) in meq/L
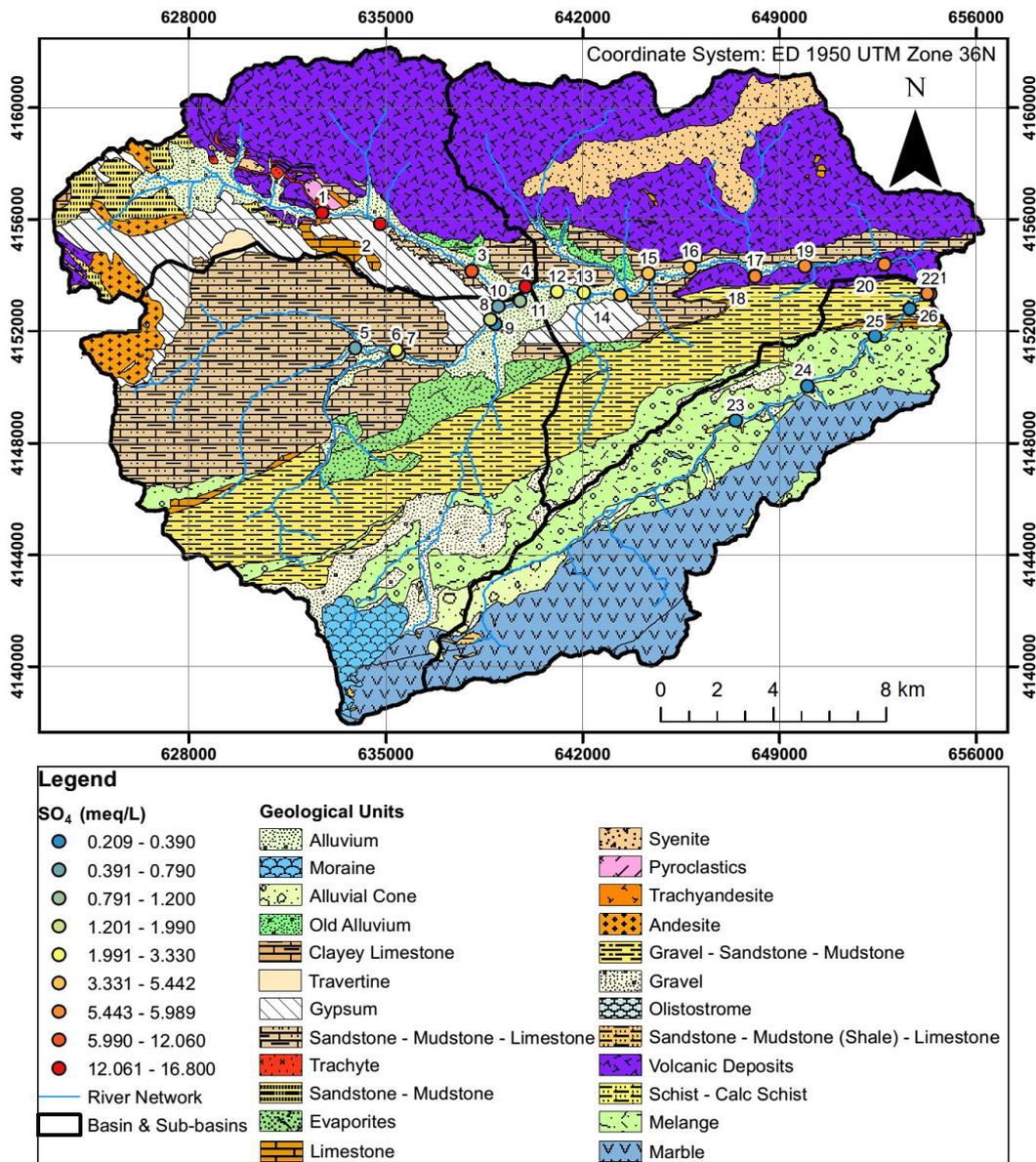
Figure 4.4. Sample classification according to sulfate (SO$_4^{2-}$) in meq/L
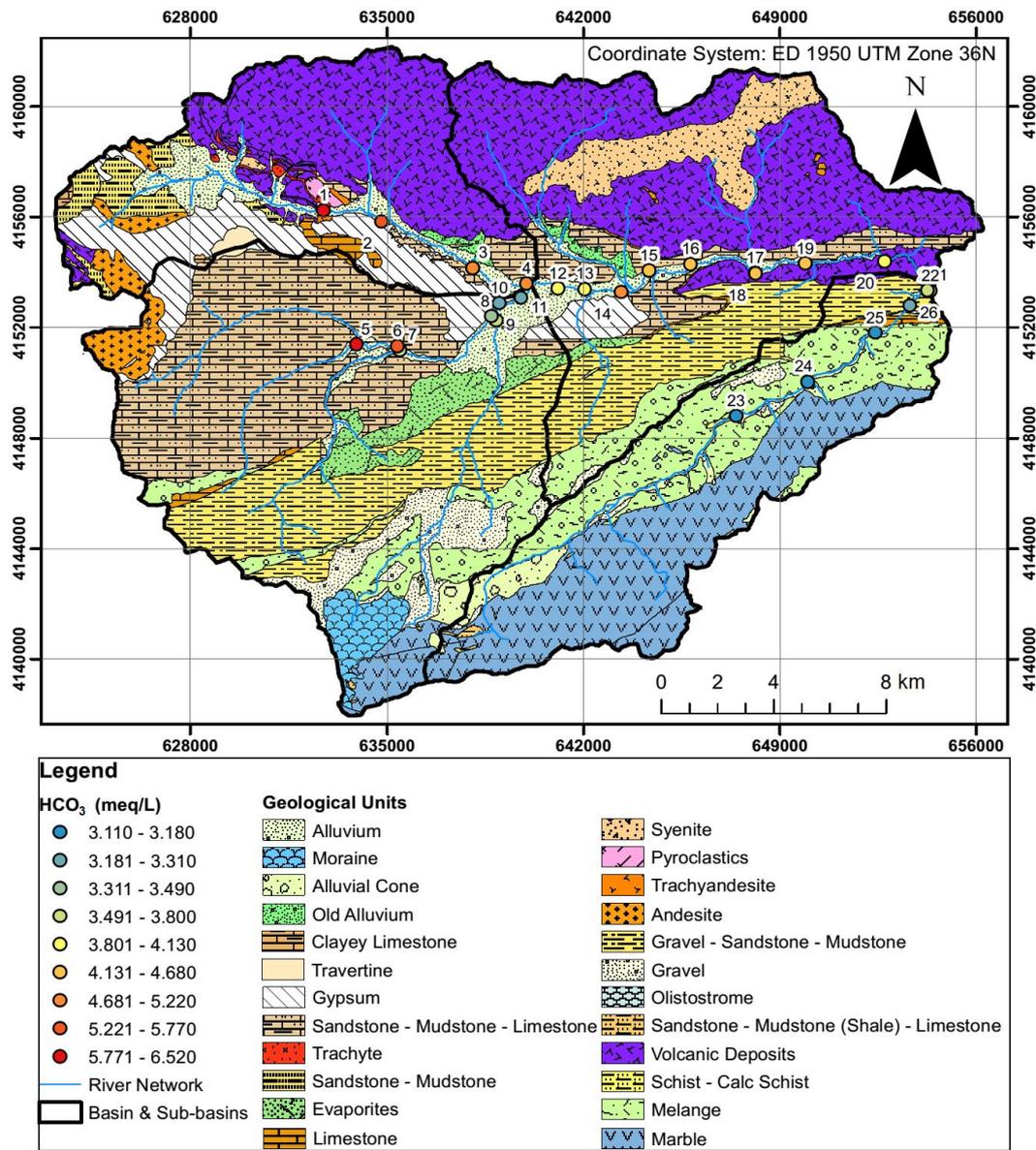
Figure 4.5. Sample classification according to bicarbonate (HCO^{3-}) in meq/L
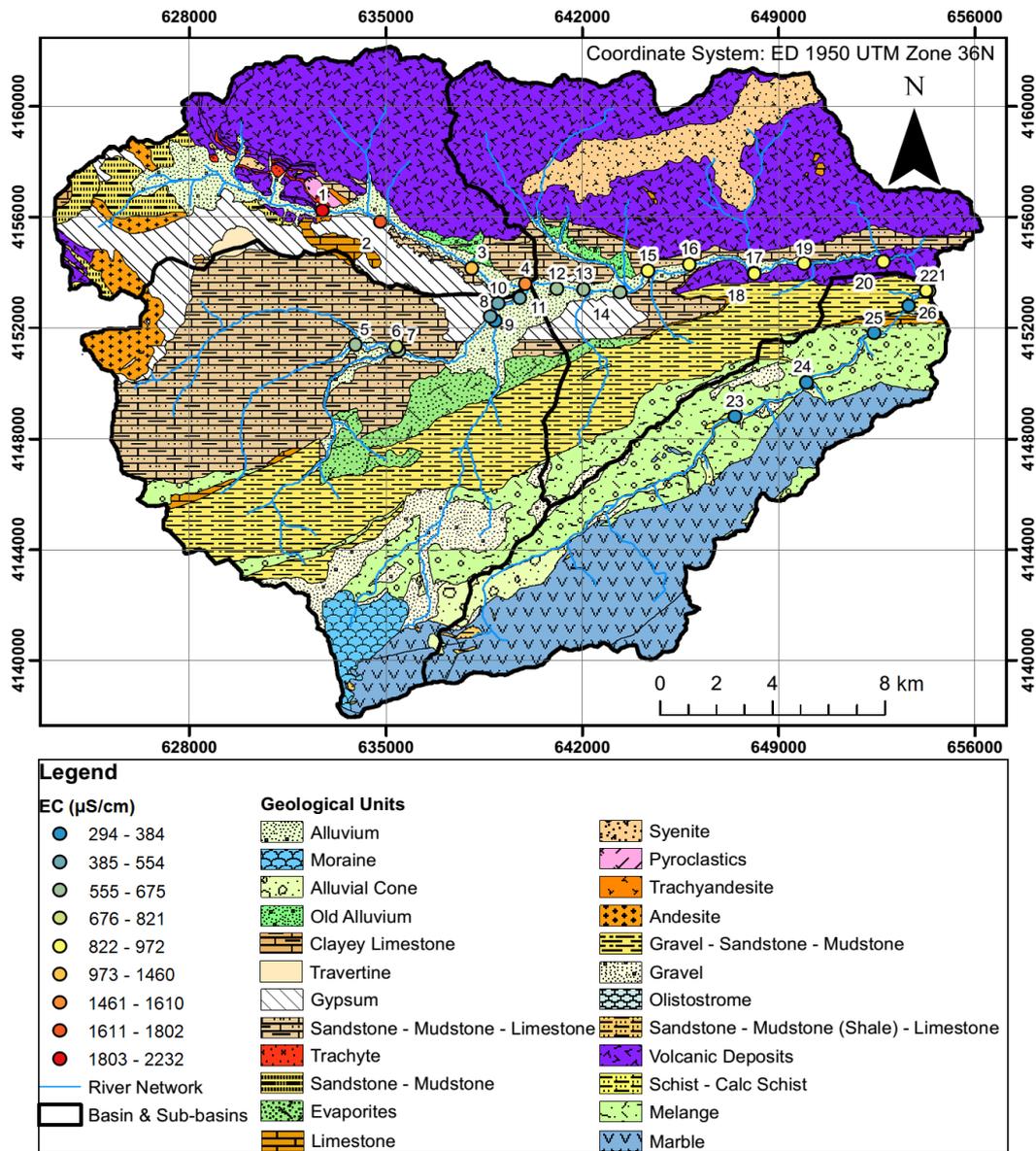
Figure 4.6. Sample classification according to electrical conductivity (EC), μS/cm

It is seen from Table 4.1 that Upper Çakıt Stream branch has the highest total dissolved solids, specifically attributed to the gypsum units ($CaSO_4 \cdot 2H_2O$) dissolving high concentrations of sulfate and calcium. On the other hand, Alihoca Stream branch shows the lowest total dissolved solids where bicarbonate and calcium have higher concentrations compared to other ions measured along this branch. Similar to Alihoca

branch, Ganimet and Darboğaz river branches are also characterized by low total dissolved solids. Upper Çakıt and Darboğaz branches merge immediately downstream of sampling locations 4 and 11, respectively, to form Çakıt river reflecting mixed ion concentrations. Along Çakıt River, sulfate and carbonate concentration increase from sampling location 13 to 14 due to confluence of a tributary draining gypsum units to the south. Confluence of a northerly tributary before sampling location 15 further increases ion concentrations, specifically sodium, sulfate and chloride.

Considering the cation concentrations, all the samples can be classified as Ca-type hydrochemical facies except one sample with no-dominant type in Kılan (See Figure 4.1, Figure 4.2 and Figure 4.3). In terms of anion concentrations, Upper Çakıt and downstream of Çakıt Stream can be classified as SO_4-type, whereas the rest of the basin can be classified as HCO_3-type surface waters (See Figure 4.1, Figure 4.2, Figure 4.4 and Figure 4.5). Overall, hydrochemical facies of Upper Çakıt and downstream parts of Çakıt are Ca-SO_4 type, whereas Ganimet, Darboğaz, Kılan and upstream part of Çakıt river branches are Ca-HCO_3 type waters. The results show that outcrops of gypsum units have strong controls on the hydrochemical characteristics of the Çakıt stream.

Relatively high HCO_3^- concentrations and low rate of Cl concentration (Table 4.1) can be simply attributed to shallow groundwater circulation in the basin according to major ion evolution (Domenico, 1972). Low TDS concentrations and relatively high HCO_3 concentrations in Alihoca, Ganimet and Darboğaz river branches together with steep stream gradients were interpreted as the sign of less GW-SW interaction potential. The discharge in Upper Çakıt is significantly low and stream is not accessible due to steep valley sides and relatively steep streambed slopes. Moreover, downstream part of Çakıt is also characterized by steep valley sides and relatively steep streambed slopes. Considering the high amount of alluvium deposits, gentle streambed slopes and accessibility, a 2-km reach in the upstream part of the Çakıt Stream, situated between sampling locations 12 and 14, was selected as the study reach where GW-SW exchange processes will be further investigated.

4.2. Application of Hierarchical Methodology in Çakıt Stream

4.2.1. Water-Borne Geophysical Survey

In our study, EMI surveys were used to pinpoint the locations with high permeability/porosity and hence locations with potential GW-SW interaction based on the idea proposed by Binley et al., 2013; see Chapter 2 for details. First, EMI survey has been conducted along the 2-km long reach of the Çakıt Stream (identified in Section 4.1) on 31 January, 2018 for reconnaissance purposes (Figure 4.7). The instrument used for EMI survey is the Multi-depth Electromagnetic Conductivity Meter (CMD) by GF Instruments (GF Instruments, Brno, Czech Republic). The instrument was used with the CMD-1 probe with an effective depth of 1.5 meters. Coordinates of EMI measurements were recorded simultaneously using a SATLAB-SLC GPS receiver (Satlab Geosolutions AB, Askim, Sweden), and water depth and water conductivity were measured with an Onset HOBO U20-001-01 water level data logger by dragging along the streambed. EC of the streambed sediments were estimated using the apparent EC data obtained from EMI surveys together with the water conductivity and water depth measured with the HOBO water level data logger (Onset Computer Corp., Bourne, Massachusetts, US) as described in Binley et al., 2013.

Based on the EC results obtained from the first EMI survey, another EMI survey and FO-DTS have been conducted on a narrower stream branch with a specific focus on a major anomaly location together with its' 550 meters of downstream (668 m in total length) (Figure 4.8). Figure 4.8 also shows the locations of nested piezometers and vertical temperature profiles which are determined according to the results of EMI survey. Reasons to choose the locations of nested piezometers and vertical temperature profiles are discussed in Chapter 5 in detail.

Figure 4.7. A view of EMI Survey conducted along Çakıt Stream. CMD (Orange device) is held horizontally at a certain distance from stream and HOBO (at the bottom of white stick) is dragged along the stream.
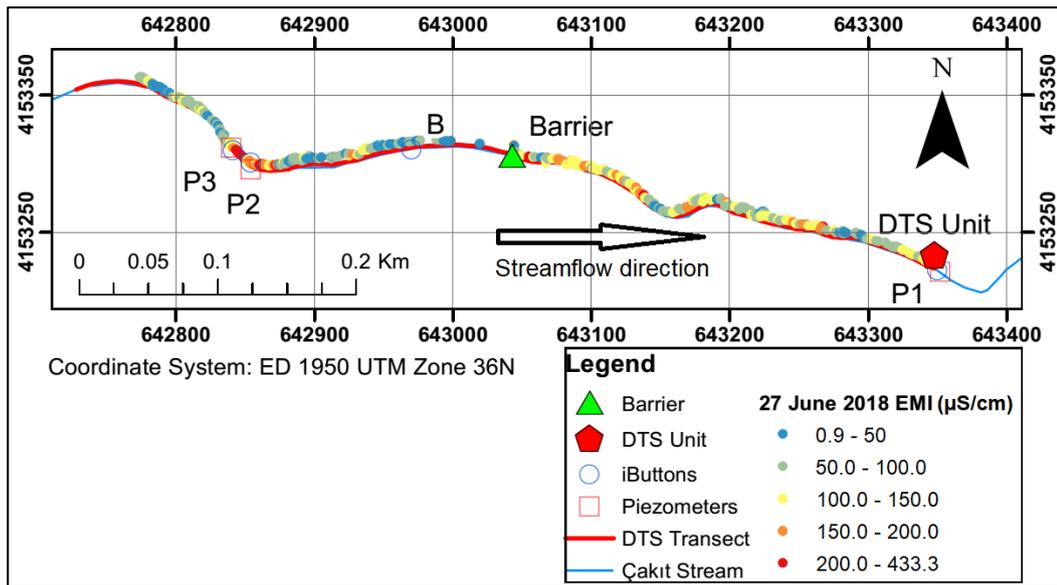
Figure 4.8. Map showing the locations of nested piezometers, vertical temperature profiles (iButtons) and FO-DTS transect along with EMI Survey conducted on 27 June 2018

4.2.2. Fiber-Optic Distributed Temperature Sensing Technology

FO-DTS unit employed for the study was XT-DTS™ (Silixa, Hertfordshire, United Kingdom) with finest sampling resolution of 25 cm over a measurement range of up to 10 km, and temperature resolution higher than 0.1 °C (Figure 4.9). The device has the capacity to be operated under ambient temperatures of -40 °C - +65 °C. A 1-km long multi-mode single steel wall tube armoured fiber optic duplexed cable (Silixa, Hertfordshire, United Kingdom) was employed together with XT-DTS™ (Figure 4.10). A Deep Gel Cycle Battery with 12 Volt 38Ah/20Hr capacity was used as energy source of DTS. Using the battery DTS system could be operated for approximately four hours. In all field works, planned measurements was to collect data for 30-min periods at different time intervals of a day. Considering 4 measurement periods would only use up roughly half of the battery, hence there would be no problem in terms of energy source during the measurement day.

Figure 4.9. Silixa XT-DTS and general setting of the device. DTS unit, temperature probe (gray stick) connected to XT-DTS, fiber-optic cable connection (orange cable with green plug), and computer connection via Ethernet cable (yellow cable).
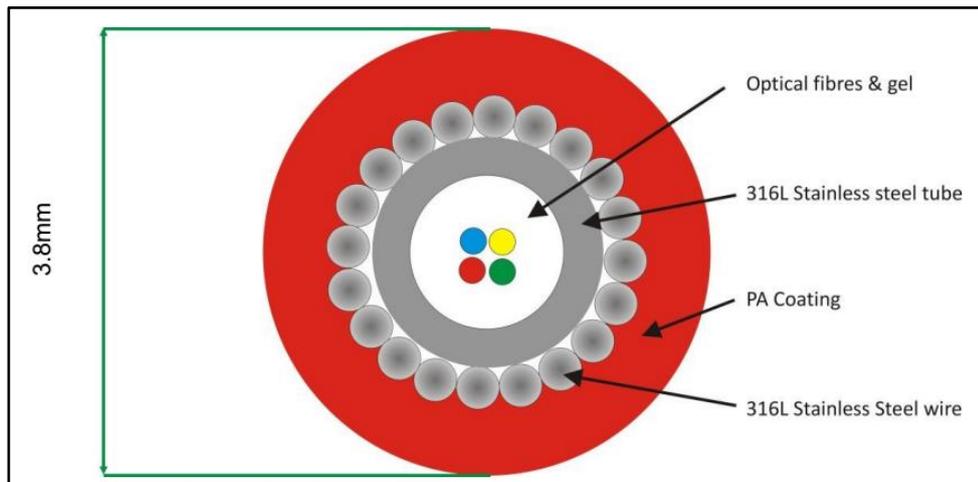
Figure 4.10. Inner layers of the Silixa multi-mode single steel wall tube armoured fiber optic duplexed cable. Two duplex Fiber cores and outer layers of the fiber.

Measurements were taken in June, September and October, 2018. Length of the cable laid on streambed was 668 meters, and FO-DTS unit was located at downstream end of the study site (Figure 4.8). Position of the cable was recorded at every twenty meters using Garmin hand-held GPS tracker. Cobbles were laid on cable to maintain the connection between streambed and cable at every few meters/where necessary. Although burying the cable in the streambed could give a better result, this option was not possible due to presence of pebbles, and cobbles (Figure 4.11). Double-ended calibration method, which is well described by Van de Giesen et al., 2012, was adopted for the study since it gives better results under harsh conditions (See Figure 4.12 and Figure 4.13a for field setting of FO-DTS). Measurements were taken at each 0.254 m and they have been performed continuously for approximately 30 minutes. XT-DTS™ was capable to take each measurement in 23 seconds when combined with the 1-km long FO cable. Two calibration baths, one hot and one cold, were located near FO-DTS unit (Figure 4.13b). 10 meters-long fiber-optic cables were submersed into calibration baths, so that approximately 40 measurements were recorded for each calibration bath considering spatial resolution of the setting is 0.254 m. Temperatures of the calibration baths were traced using Pt100 temperature calibration probes which

were provided together with FO-DTS Unit. Battery-powered aquarium pump was used in calibration baths to prevent thermal stratification.
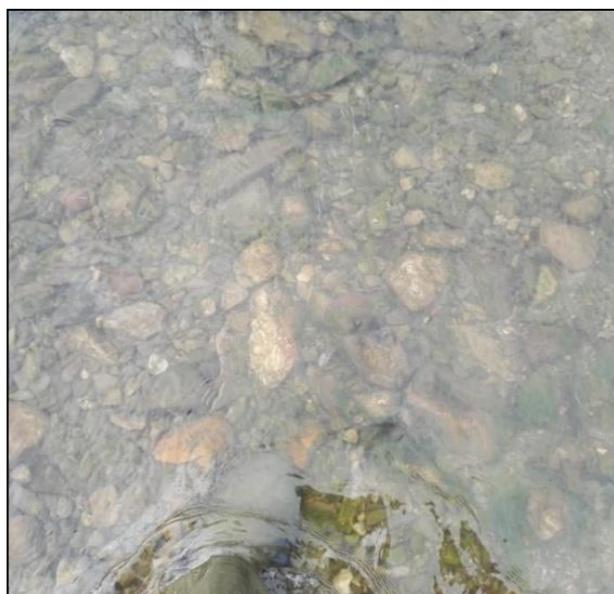
Figure 4.11. General view of streambed in terms of grain size (pebble-gravel, cobble and boulder)
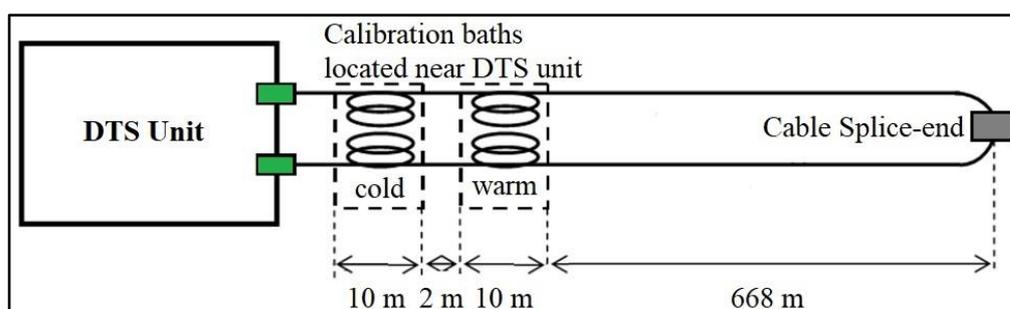
Figure 4.12. Field setting of FO-DTS system and length of the cables (adapted from Van de Giesen et al., 2012)

Figure 4.13. (a) A view of the field setup for the FO-DTS system and (b) calibration baths located near FO-DTS

It is important to point out that FO-DTS measurements performed on June, 2018 was intended to see the capabilities of FO-DTS technology on study site, and they were approximately 130 meters shorter at upstream end (538 meters in total length) compared to other measurement periods (668 meters in total).

4.2.3. Nested Piezometers and Vertical Hydraulic Gradient Estimation

Piezometers consisted of high density polyethylene (HDPE) pipes having an 32 mm outer diameter and 2.6 mm inner wall thickness. Screen length of piezometers was 20 cm at the bottom. Piezometers were incised instead of perforation so that plugging could be minimized and piezometer bottoms were plugged with plastic pipe caps to prevent vertical flow. For installation of piezometers, a mechanical installation method is applied similar to method described by Baxter et al., (2003). Installation units were constructed in Metal Workshop of Middle East Technical University. Installation units consist of a metal pointed inner driver rod and an outer metal tube that prevents collapse of opening during which driver rod is taken out of the metal tube (Figure 4.14). On top of these two units, massive caps, that osculate each other

when the inner rod is driven in, were welded to bear hammer blows. Holes on the sides of these caps enabled the use of an iron bar to take the units out of borehole after HDPE piezometers are installed through. After the installation, piezometers were supported by wooden sticks to prevent flexure, and top of the piezometers were closed by pipe caps with small openings to enable water to freely move in the piezometer.
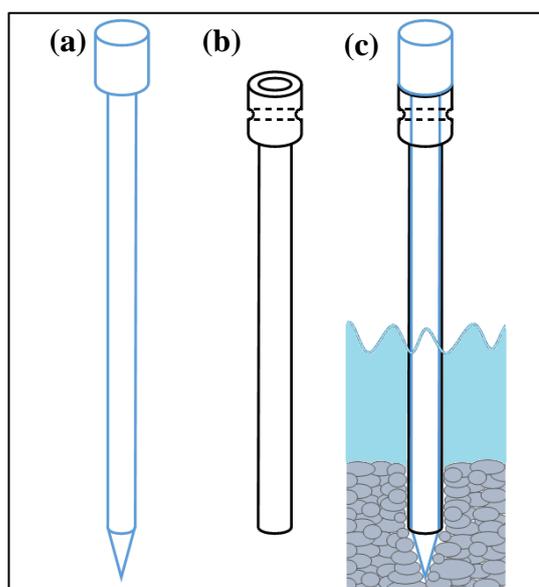
Figure 4.14. Installation units; (a) Metal pointed inner driver rod, (b) Outer metal tube that prevents collapse of opening during installation of piezometer, and (c) driving in installation units into streambed.

Seven piezometers were installed within the streambed using the explained method in 3 different sites with the names of P1, P2 and P3 (Figure 4.8). See Figure 4.15, Figure 4.16 and Figure 4.17 for the details of piezometer installations. Each site consisted of one shallow and one deep piezometers (nested). Three piezometer locations were chosen according to the results of EMI survey. From these three piezometer sites, two were the locations where major EC anomaly values were obtained from EMI surveys, and the third was the downstream end of the study site with low to intermediate EC value of streambed sediments. The depth of shallow and deep piezometers from

middle of the screen to top of the streambed vary between 36 cm – 43 cm, and 85 cm – 102 cm, respectively.

Piezometers P1, P2 and P3 were installed on 27 June, 28 June and 18 September 2018, respectively. While piezometer names with "S" represent shallow piezometers, the ones with "D" represent deep piezometers (for example, P1-D is for deep piezometer at site 1). Manual water level measurements, and hence hydraulic head values were taken from piezometers P1 and P2 between 28 June and 7 November 2018, and from piezometers P3 between 19 September and 7 November 2018 using a Solinst® level meter, Model 107 TLC Meter (Solinst Canada Ltd., Georgetown, Ont., Canada) (Figure 4.18).
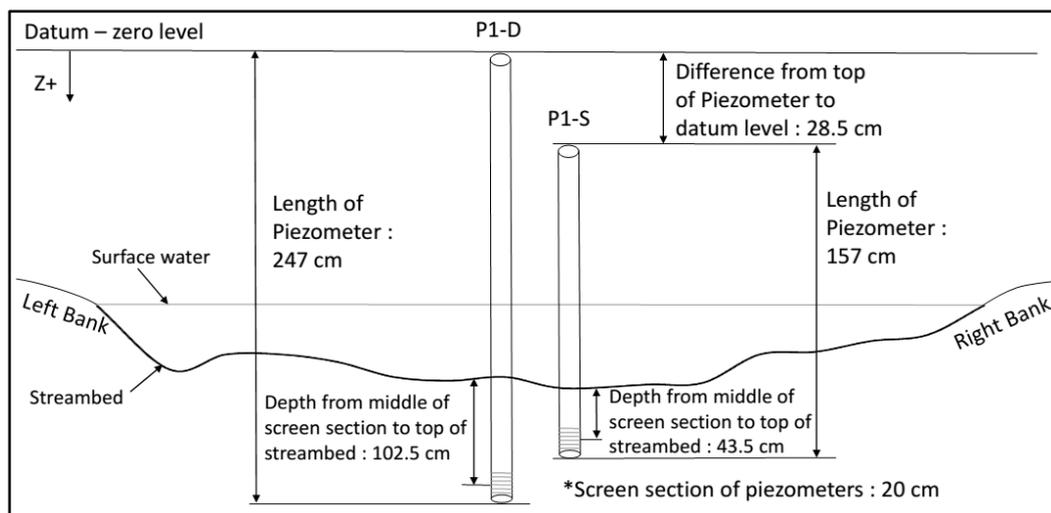
Figure 4.15. A sketch for piezometers of location P1
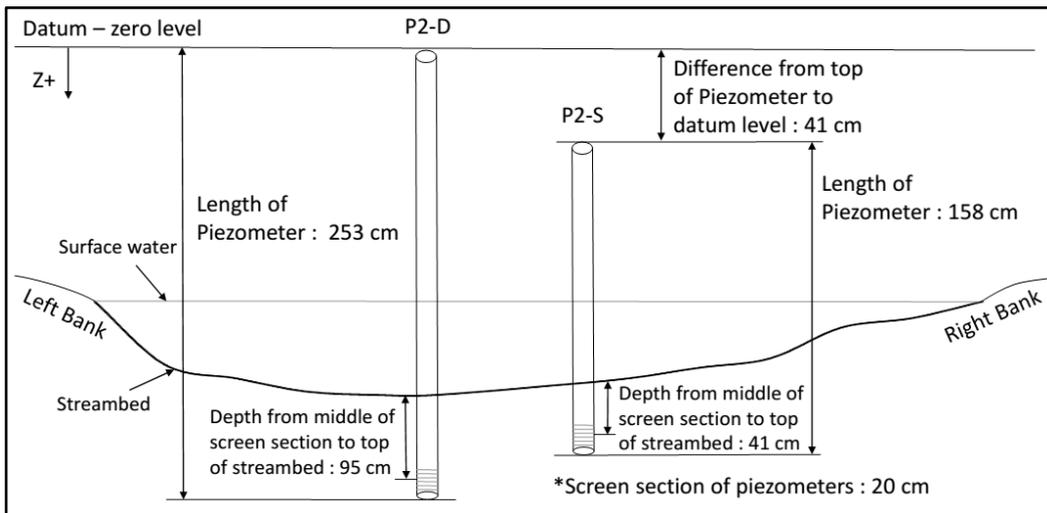
Figure 4.16. A sketch for piezometers of location P2
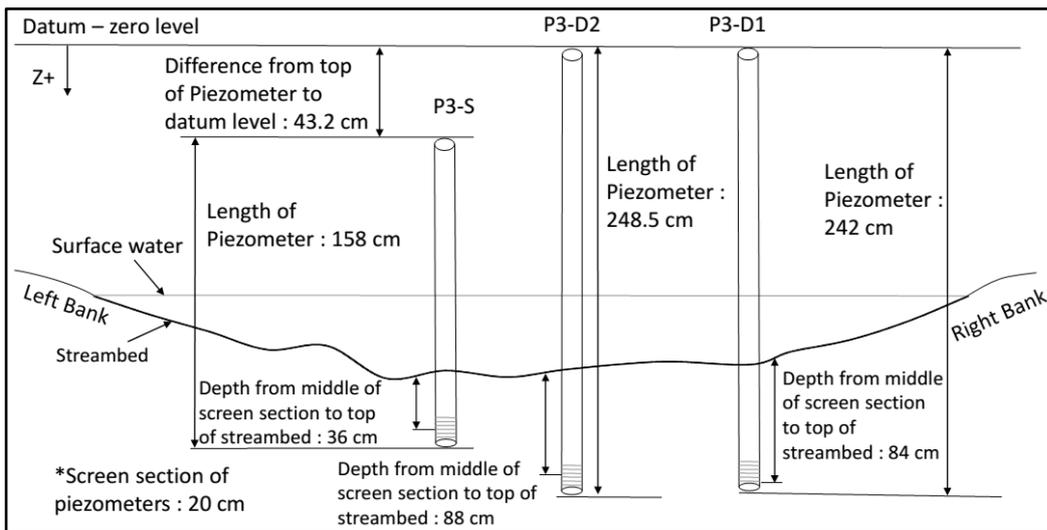
Figure 4.17. A sketch for piezometers of location P3

Figure 4.18. Water level, EC and temperature measurement using TLC meter

Hydraulic head measurements from nested piezometers and surface water stage were used to calculate vertical hydraulic gradient values, and hence the direction of streambed vertical flux at the point scale. Negative hydraulic gradient values indicate upwelling flux direction while positive values indicate downwelling flux direction. The vertical hydraulic gradient (VHG) for each single piezometer is calculated using Equation 10.

$$VHG(\%) = \frac{Depth\ to\ WL\ inside\ piezo. - Depth\ to\ surface\ water}{Depth\ to\ middle\ of\ screen\ from\ the\ streambed} \ x\ 100 \tag{10}$$

The VHG values for nested piezometers are calculated based on Equation 11:

$$VHG\ (\%) = \frac{WL_D - WL_S}{L_D - L_S} * 100 \tag{11}$$

where WL_D and WL_S denote water level of deep piezometer and shallow piezometer, respectively, L_D and L_S represent distance between the datum and the mid-screen for deep and shallow piezometers, respectively.

For more detail, automated water level measurements were performed using HOBO pressure transducers (Onset Computer Corp., Bourne, Massachusetts, US) emplaced in P2 and P3. A total of five pressure transducers were deployed –near P1 for atmospheric correction, P2-S, P2 surface water, P3-S and P3-D2. In order to calculate water levels, atmospheric pressure data obtained by HOBO pressure transducer near P1 is used as reference pressure. Water levels are calculated using the following equation:

$$h = \frac{P_{abs} - P_{ref}}{d_w * g} \tag{12}$$

where P_{abs} stands for absolute pressure measured in water, P_{ref} is reference air pressure, d_w is density of water and g is gravity. The continuous water level data obtained from HOBO pressure transducers are then used to calculate VHG of P2 and P3. VHG at site P2 is calculated using equation (10) while VHG at Site P3 is calculated using equation (11).

4.2.4. Vertical Flux Determination from Vertical Temperature Profile

Vertical water flux through the streambed were estimated from diurnal variations in streambed vertical temperature profiles. 1-Wire iButton Temperature loggers (Maxim Integrated® DS1922L) having 0.0625 °C resolution, 0.5 °C accuracy at -10°C to 65°C temperature range were used. iButtons were water-proofed with plasti-dip spray paint and embedded on wooden dowels at two different configurations (Figure 4.19). iButtons were shielded with metal washers to ensure proper thermal conductivity with the streambed. They were set to record the temperature every 10 minutes to make sure that the diurnal temperature variation is properly captured. iButton temperature profiles were recorded in 4 different sites; P1, P2, P3, and B (Figure 4.8) with time

periods ranging from 5 to 16 days. Although the EC data at location B failed in the quality control step, this site was chosen due to surficial features, such as reeds. Due to availability of only 7 sensors, the number of sensors per profile were varied between two and three in an effort to maintain a balance between the number of profile locations and ensuring flux estimation in case of a sensor failure. Considering the configuration of iButton sensors at known depths (Figure 4.19) one flux calculation (depth of 9.5 cm) can be made for the data gathered from location P1 in June, P2 in October and from B in October (two iButtons), and three flux calculations (depths of 5.5 cm, 9.5 cm and 13 cm) can be made with the data gathered from location P2 and P3 in September where three iButtons were installed at each location (see Table 4.2).
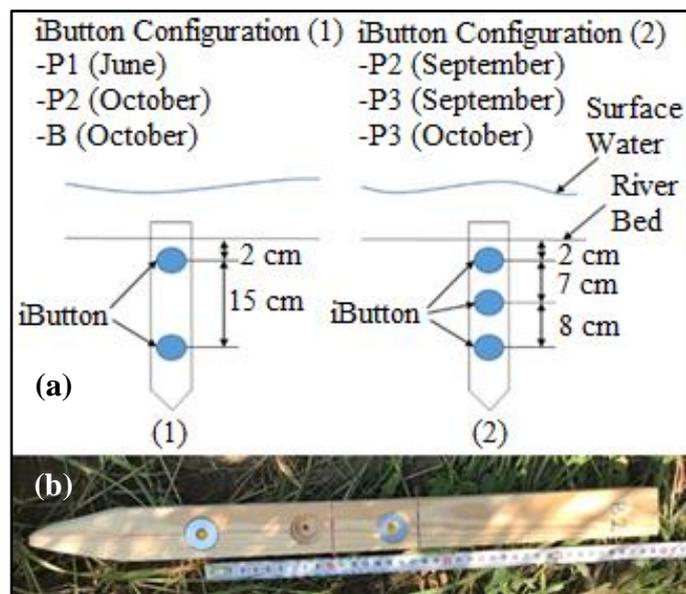
Figure 4.19. (a) Configurations of iButton Thermochrons at each location, (b) photo showing the configuration at location P1 in June field trip.

Table 4.2. *iButton installation sites and measurement periods*

Location	Starting date of gathering the data	End date of gathering the data	Coordinates (ED 50)	
			Easting (meter)	Northing (meter)
P1	28.06.18 11:40	02.07.18 15:10	643350	4153220
P2	18.09.18 16:40	03.10.18 12:00	642854	4153300
	26.10.18 16:30	07.11.18 11:30		
P3	18.09.18 16:00	03.10.18 12:00	642841	4153310
	26.10.18 16:30	07.11.18 11:30		
B	26.10.18 16:30	07.11.18 11:30	642970	4153310

Vertical water fluxes were estimated using VFLUX program – a vertical fluid heat transport solver (Gordon et al., 2012) based on Hatch et al., (2006) Amplitude Method. Typical values of sediment and water thermal properties suggested by the program developers were used; thermal dispersivity (0.001 m), thermal conductivity (0.0045 cal/(s·cm·°C)), volumetric heat capacity of the water (1.00 cal/(cm^3·°C)) and total porosity (0.28).

4.2.5. Analyses of Water Quality Parameters in Surface Waters and Piezometers

Temperature and electrical conductivity values were measured manually from surface waters and piezometers using Solinst® TLC Meter (Model 107). Surface water and piezometer measurements were performed twenty four times at P1 and P2, and fourteen times at P3 from 28 June, 2018 to 07 October, 2018 during all field campaigns.

CHAPTER 5

RESULTS AND DISCUSSIONS

5.1. Water-Borne Geophysical Survey

First EMI survey was performed as a reconnaissance along a 2 km long river reach on 31 June, 2018 with a depth of investigation equal to 1.5 m. A major anomaly was detected during this reconnaissance survey (Figure 5.1). This anomaly together with 500 m long reach towards downstream was selected as the study area to investigate the GW-SW interaction processes in a detailed manner. The second EMI survey has been conducted on 27 June, 2018 along this narrowed study area. Depth of stream water ranged between 0 - 80 cm with a mean value of 29.3 cm during 27 June, 2018 EMI survey. EC of stream water was 894 µS/cm during the 27 June 2018 survey. EC values were obtained by subtracting EC value of streamwater from apparent EC values inferred from EMI survey. It can be seen from Figure 5.2 that the locations of the major EMI anomalies coincide between the two EMI surveys representing winter (Figure 5.2a) and summer (Figure 5.2b) periods.
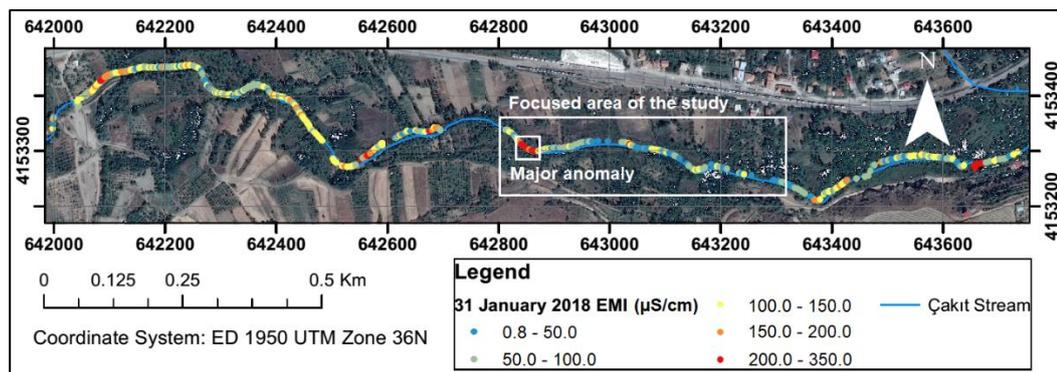
Figure 5.1. EC values (µS/cm) of streambed sediments inferred from EMI Survey performed on 31 January, 2018
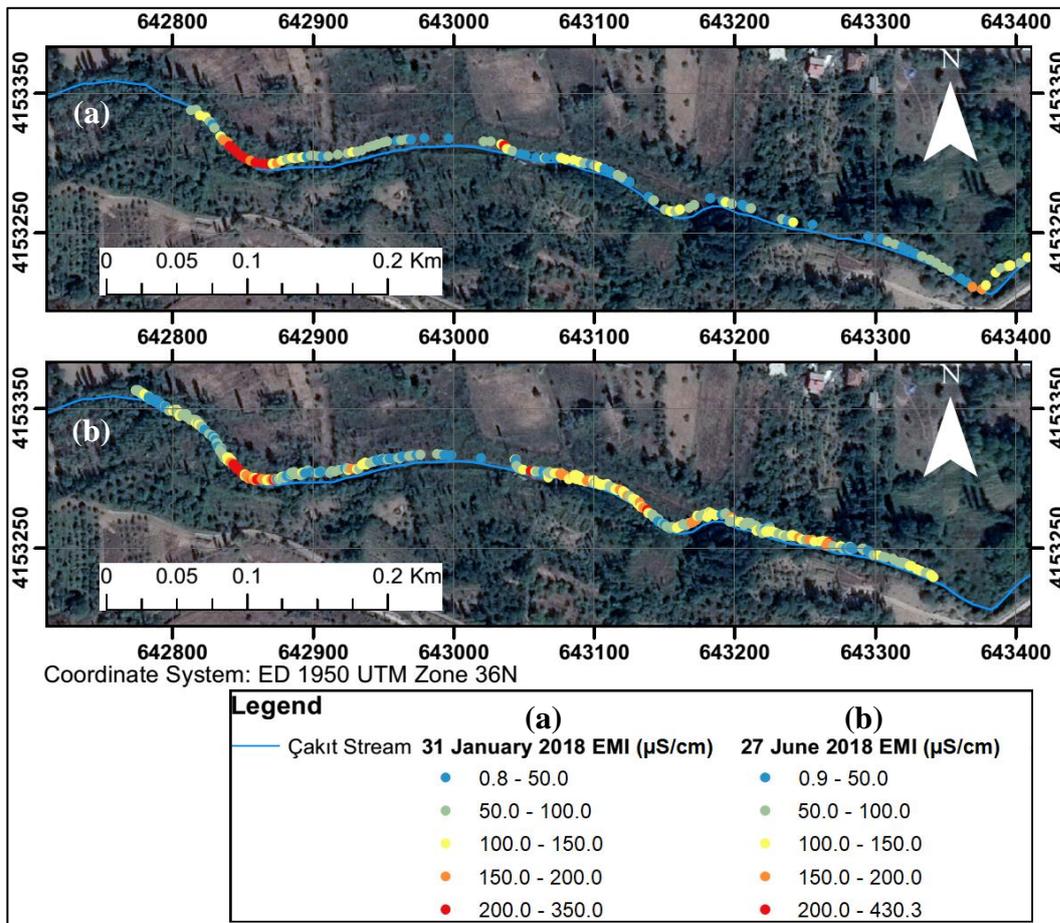
Figure 5.2. EC values (μS/cm) of streambed sediments inferred from EMI surveys on (a) 31 January, 2018, and on (b) 27 June, 2018

Considering that EMI anomalies coincide with potential groundwater upwelling locations, a multitude of techniques which were previously explained have been utilized to further characterize spatio-temporal distribution of GW-SW exchange fluxes along the selected study reach. Figure 5.3 shows the locations where these techniques have been conducted along with the results of EMI survey measured on 27 June 2018, as a reference.

60
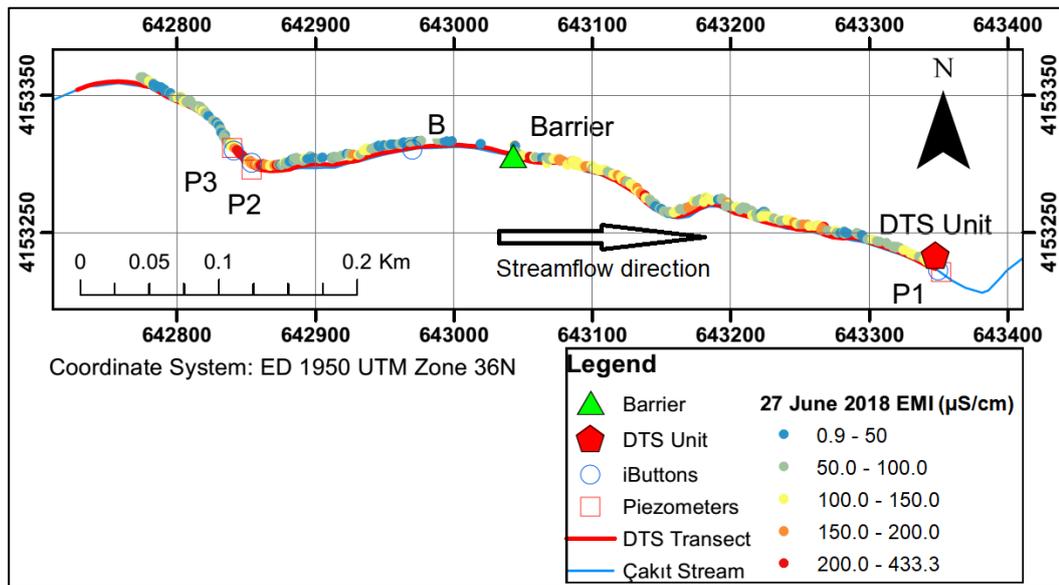
Figure 5.3. Map showing the locations of nested piezometers, vertical temperature profiles (iButtons) and DTS transect along with EMI Survey conducted on 27 June 2018

Figure 5.4 shows the distances between measurement sites along the study reach. Note that the fiber-optic cable used in FO-DTS measurements stretches between 0-668 m along the study reach. A man-made barrier diverting stream water for irrigation shown on Figure 5.3 and Figure 5.4 (see Figure 5.5 for the view of the barrier) is located at 328 m (around 643050 Easting), and the barrier affects hydrological behavior of the area in small scales.
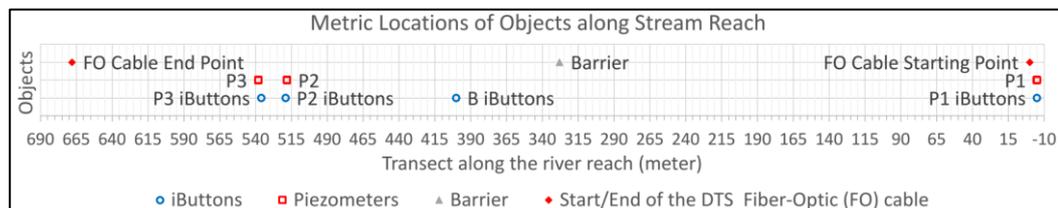
Figure 5.4. Transect along the study reach showing distances between measurement sites. Note that the beginning of the DTS fiber optic (FO) cable marks the origin.

Figure 5.5. View of the barrier from two different aspects

5.2. Fiber-Optic Distributed Temperature Sensing Technology

DTS measurements were performed in June, September and October field studies. During these measurements groundwater temperature was stable around 14 °C. Table 5.1 lists DTS measurement periods, minimum, mean and maximum values of the measured top-of-streambed temperatures, together with air temperature data collected from the nearest meteorological station, and daily stream discharge values collected from Çakıt stream gauging station. It can be seen that there is a marked difference in air temperature in October compared to June, and September periods. Moreover, stream discharge is also relatively lower in October than that of June and September.

Table 5.1. *DTS measurement statistics, air temperature and stream discharge at the time of measurement periods. Air temperature is the data collected from Ulukışla meteorological station, and stream discharge is the data collected from Çakıt stream gauging station.*

DTS Measurements		DTS Stream Measurement (°C)			Air Temperature (°C)			Stream
Date	Time	Min	Mean	Max	Min	Mean	Max	Discharge (m³/s)
27.06.2018	17:51-18:14	19.51	19.96	20.45	29.82	29.93	30.12	0.754
28.06.2018	11:18-12:12	16.51	17.69	18.80	28.52	29.25	29.72	0.711
	17:49-18:31	19.22	19.86	20.45	25.22	25.86	26.51	
18.09.2018	10:49-11:15	14.37	15.10	16.03	21.91	22.09	22.18	0.817
	13:28-13:53	16.90	17.56	18.22	24.48	24.60	24.83	
	17:33-17:48	15.76	16.53	17.24	23.58	23.88	24.14	
25.10.2018	07:41-08:11	11.17	11.66	12.17	10.58	11.59	12.42	0.672
	10:54-11:34	11.34	11.87	12.39	10.51	10.59	10.76	
	12:15-12:45	11.90	12.44	12.97	11.49	11.55	11.68	
	14:48-15:18	12.19	12.68	13.22	7.81	9.19	11.43	
26.10.2018	07:31-08:02	8.88	9.53	10.09	2.62	3.24	3.58	0.678
	10:51-11:21	9.18	9.69	10.21	2.15	2.50	2.83	
	12:32-13:02	9.73	10.43	11.11	4.59	5.22	5.51	

The temperature data obtained from FO-DTS measurements have been analyzed with the help of graphs shown in Figure 5.6-Figure 5.11. In these figures, the graphs along the first row show the 10-minute air temperature measurements obtained from Ulukışla meteorological station for the measurement day (Graph I) and measurement interval (Graph II). The graph (III) shows the depth of water above the streambed along the FO-DTS transect while graph (IV) shows the variation in temperature along the transect (y-axis) for each run (x-axis). For example, graph (IV) in Figure 5.6 shows that on June 28th, at time interval 17:49-18:31 (see also Table 5.1) 115 measurements (runs) were made along the FO-DTS transect. Note also that the DTS cable was out of the stream water at the shallowest section and at a barrier for diverting irrigation water (see Figure 5.5) corresponding to 195 m and 328 m distance along the transect, respectively. Hence the temperature data corresponding to these locations have been removed. Flow direction and piezometer locations are marked on this graph for better orientation. The graphs (V) and (VI) show the mean and standard deviation of the

temperature values obtained from all the runs at each measurement point (every 0.254 m) along the transect, respectively (mean temperature/standard deviation along the x-axis of graph (IV)). Note that the graphs (V) and (VI) also show the moving average of the highly variable mean temperature and standard deviations to be able to focus on persistent variations along the transect. In the graphs, the locations showing anomalies with respect to air temperature as well as locations with lower standard deviation values indicate sustained temperatures in time, and hence these are the locations for further investigation for upwelling groundwater.

Figure 5.6 shows the FO-DTS measurements taken on 28 June, 2018 at afternoon. As it is seen from graph (I) and graph (II) measurement period corresponds to times of cooling down of the air temperature, and yet the air temperature is between 25.2 - 26.5 °C during the measurement period. As a result of the cooling down of the air temperature, temperature of the surface water also decreases toward the end of the measurement period (along x-axis in Graph IV). It can be seen that the ponding due to the barrier strongly influences the surface water temperature (Graph IV) - ponding at upstream of barrier with higher depth of water cools the temperature along the streambed where fiber optic cable is located. However, the more stagnant ponded water warms at the surface due to solar radiation and flows downstream creating a warm anomaly at the downstream of the barrier. Standard deviation values of temperature along measurement points (Graph VI) do not show any marked low values that may indicate sustained water temperatures in time (x-axis).

Figure 5.7 shows the FO-DTS measurements taken on September 18th, 2018 around noon. It can be seen that the air temperature is warming during the measurements (Graph I and Graph II) which in turn warms the surface water across run numbers (Graph IV). More importantly however, temperature values along the transect (y-axis) highly fluctuates between 16.9 °C and 18.2 °C (Graphs IV and V) with a marked increase at the downstream of the barrier (325-328m). High variability in temperature values along the transect is possibly due to the marked solar radiation and shading effect. Note that the groundwater temperature at the same time was measured as

64

14.5°C in P2-D, hence possible groundwater inflow from the streambed would be indicated by sustained cold temperatures along the x-axis. However, groundwater inflow along the streambed could not be detected in June and September field trips due to several factors including the shading effect, stream water temperature values being close to the groundwater temperature values and high discharge conditions.
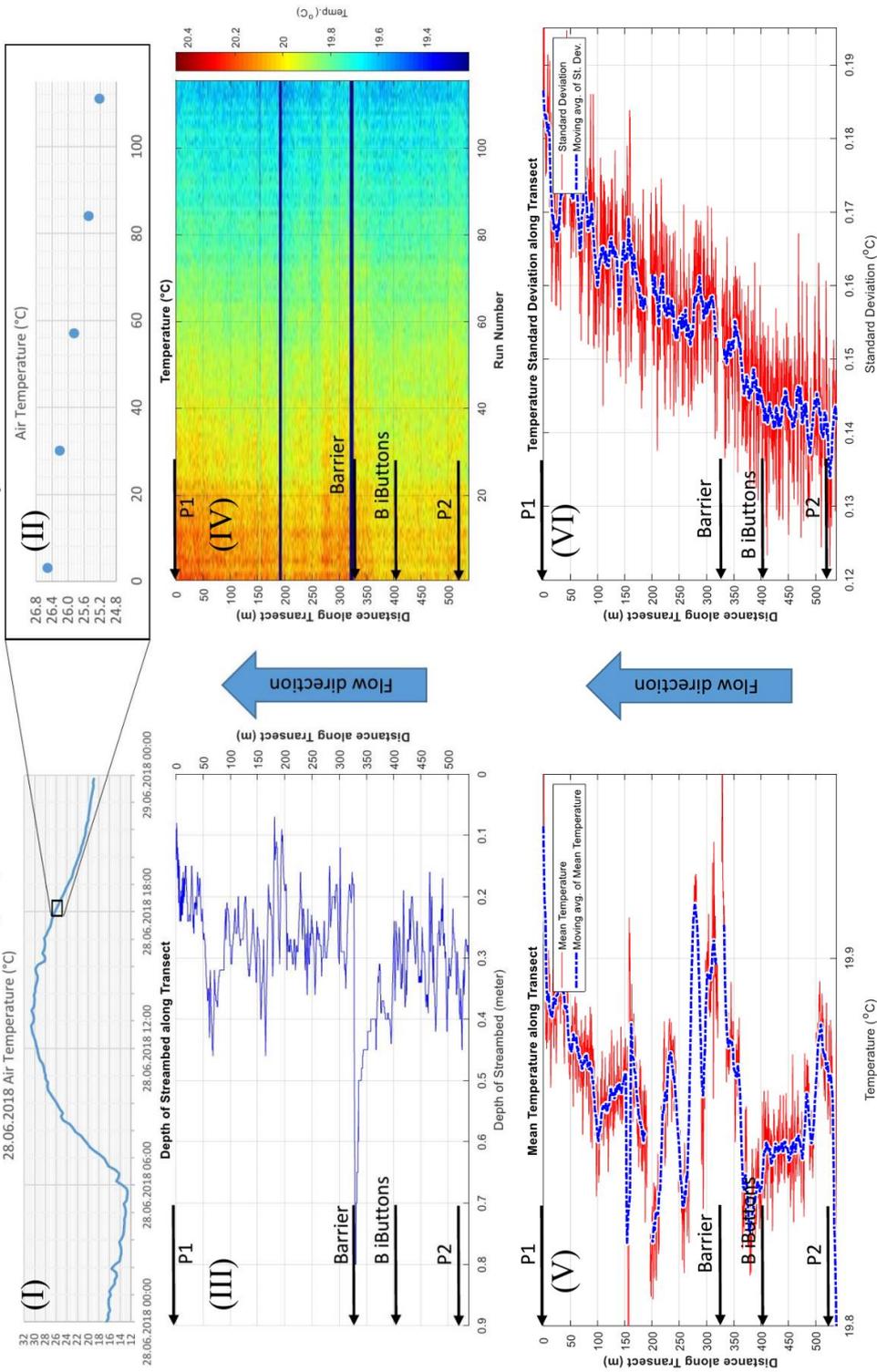
Figure 5.6. DTS measurements taken on 28 June, 2018 at 17:49 -18:31
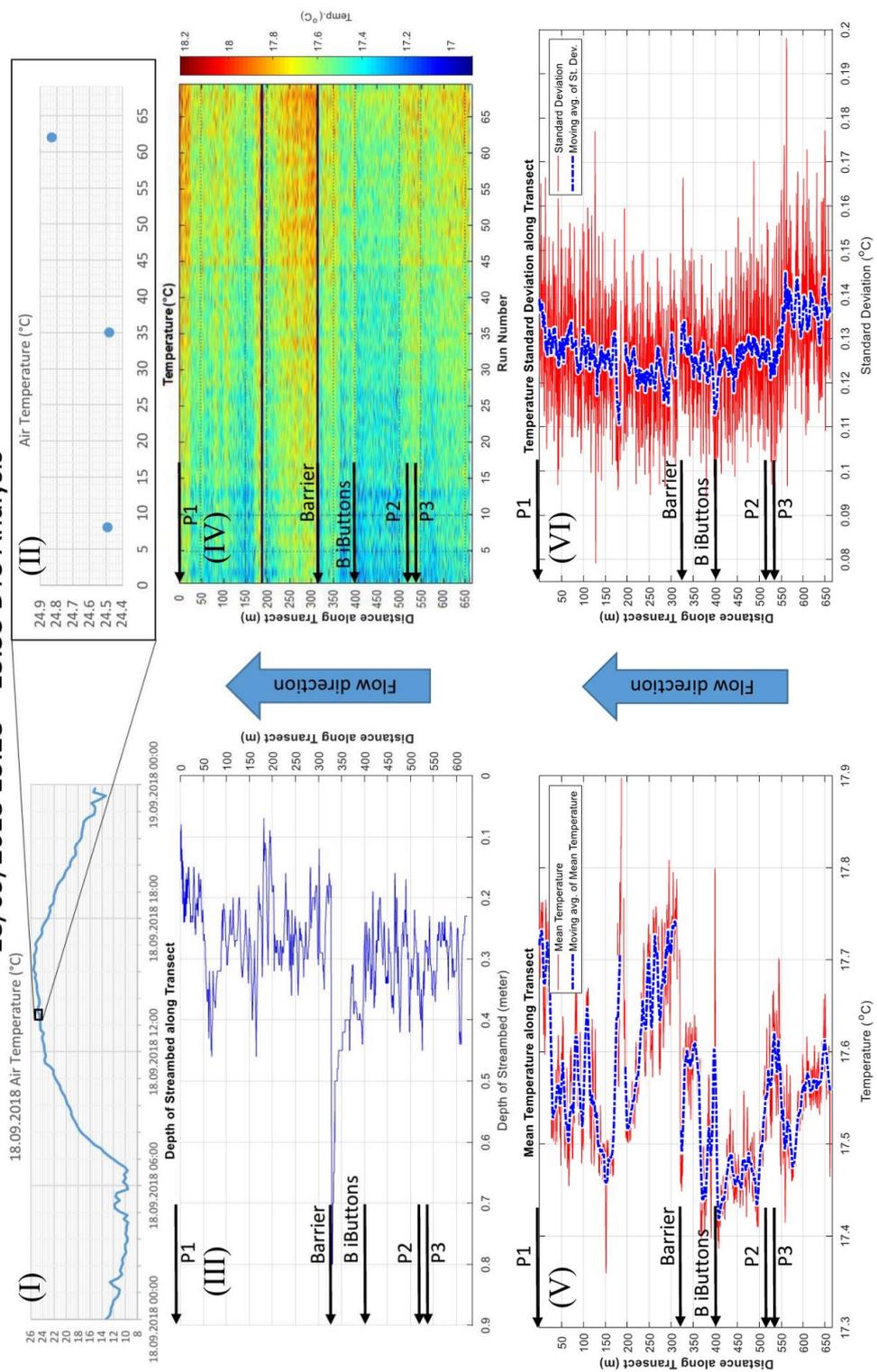
Figure 5.7. DTS measurements taken on 18 September, 2018 at 13:28 -13:53

In October, the colder air/surface water temperatures, clouds blocking solar radiation and lower stream discharge enabled favorable conditions for the DTS measurements. It can be seen from Figure 5.8 that air temperature (10.2-12.1 °C) on 25th of October, 2018 at 07:41-08:11 is significantly lower than that of June and September measurements, yet it is very close to the temperature of groundwater (14 °C). Locations with groundwater inflows would be indicated by sustained warmer temperatures along the x-axis in Figure 5.8 (Graph IV), and warm anomalies in mean temperatures (Graph V). A warm anomaly is indeed detected close to site P2 and P3 (Graph V) possibly indicating groundwater inflow from the streambed. Note also that the stream water temperature increases towards upstream which may also indicate warmer groundwater recharging streamwater at the upstream locations.

Even colder weather conditions on 26 October, 2018 gave stronger indication of groundwater upwelling close to sites P2 and P3. Figure 5.9-Figure 5.10-Figure 5.11 show DTS measurements at 07:31-08:02, 10:51-11:21, and 12:32-13:02 respectively, on 26 October, 2018 with persisting cold weather conditions. The measurements in the early morning (Figure 5.9) shows that air temperature is around 3°C whereas surface water and groundwater temperatures are around 9.5°C and 12.5°C, respectively. It can be seen from graph (V) that the surface water is cooling along the flow direction, possibly indicating warmer groundwater recharging streamwater at the upstream locations. A major warm anomaly is evident around 550 m close to piezometers P2 and P3. This warm anomaly was persistently evident for the two other measurements taken during the same day (Figure 5.10 and Figure 5.11). Hence this warm anomaly detected by the DTS measurements can be inferred as warm groundwater seepage into the stream.
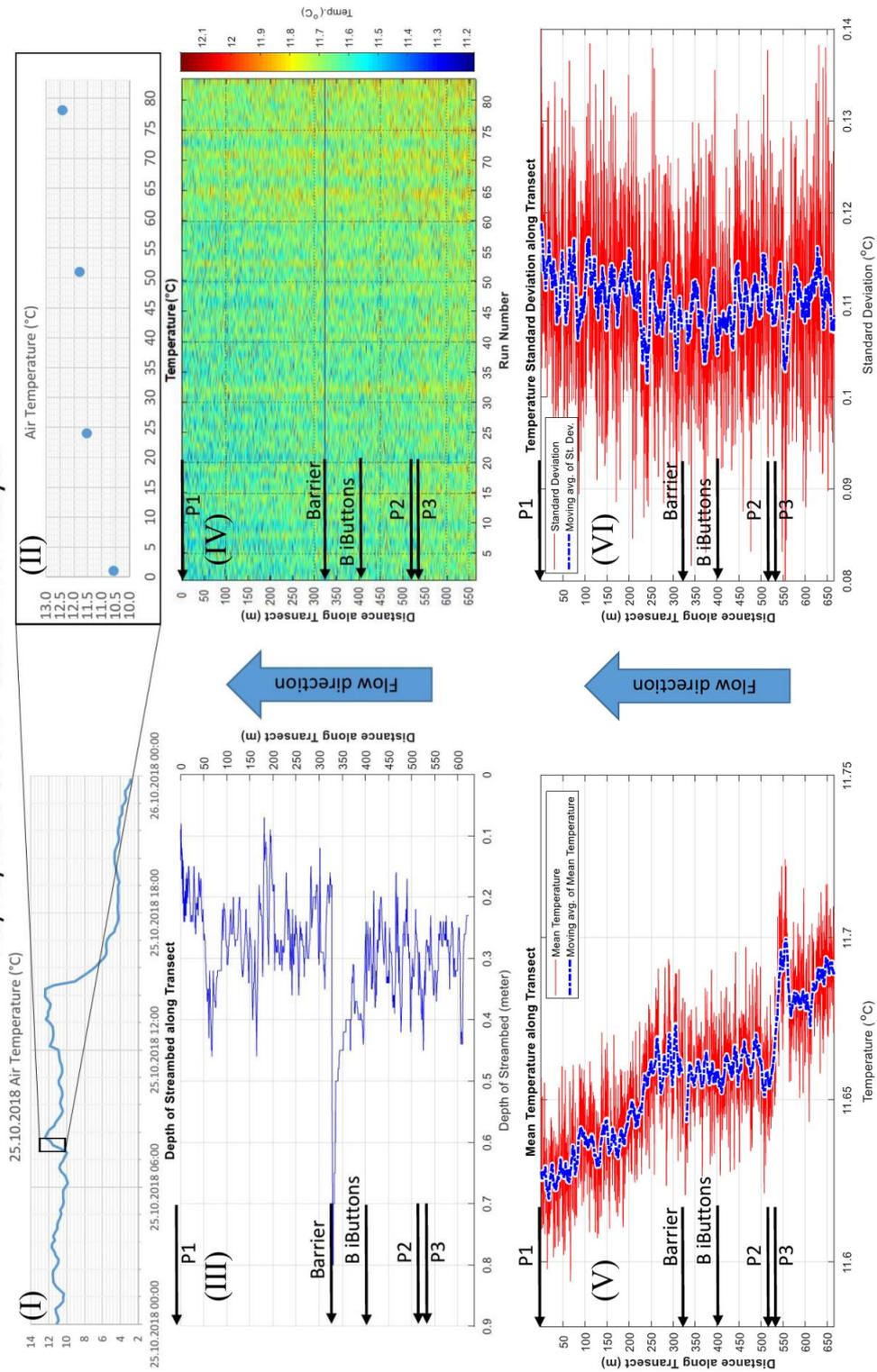
Figure 5.8. DTS measurements taken on 25 October, 2018 at 07:41 - 08:11

69
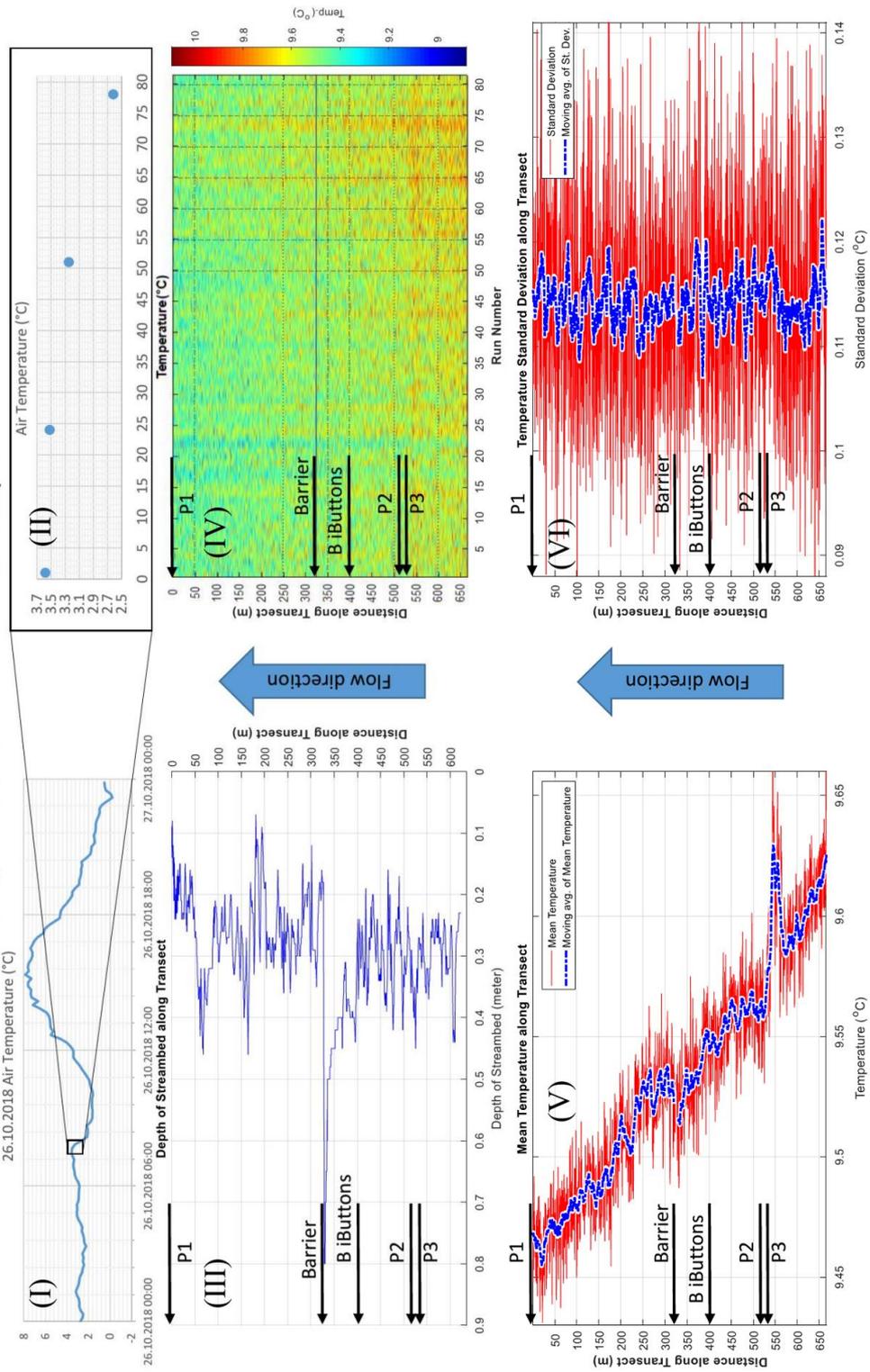
Figure 5.9. DTS measurements taken on 26 October, 2018 at 07:31 - 08:02
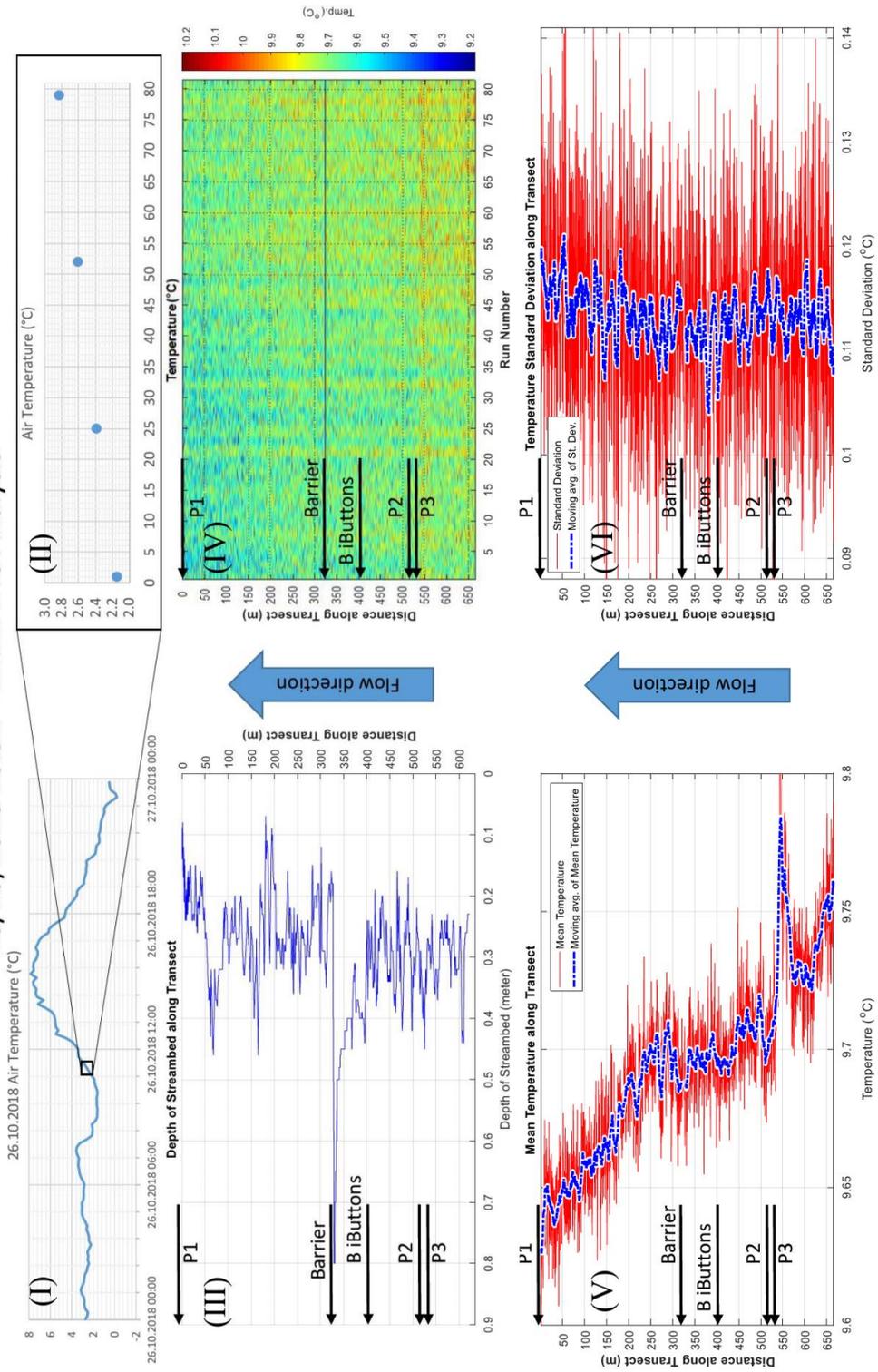
Figure 5.10. DTS measurements taken on 26 October, 2018 at 10:51 – 11:21

71
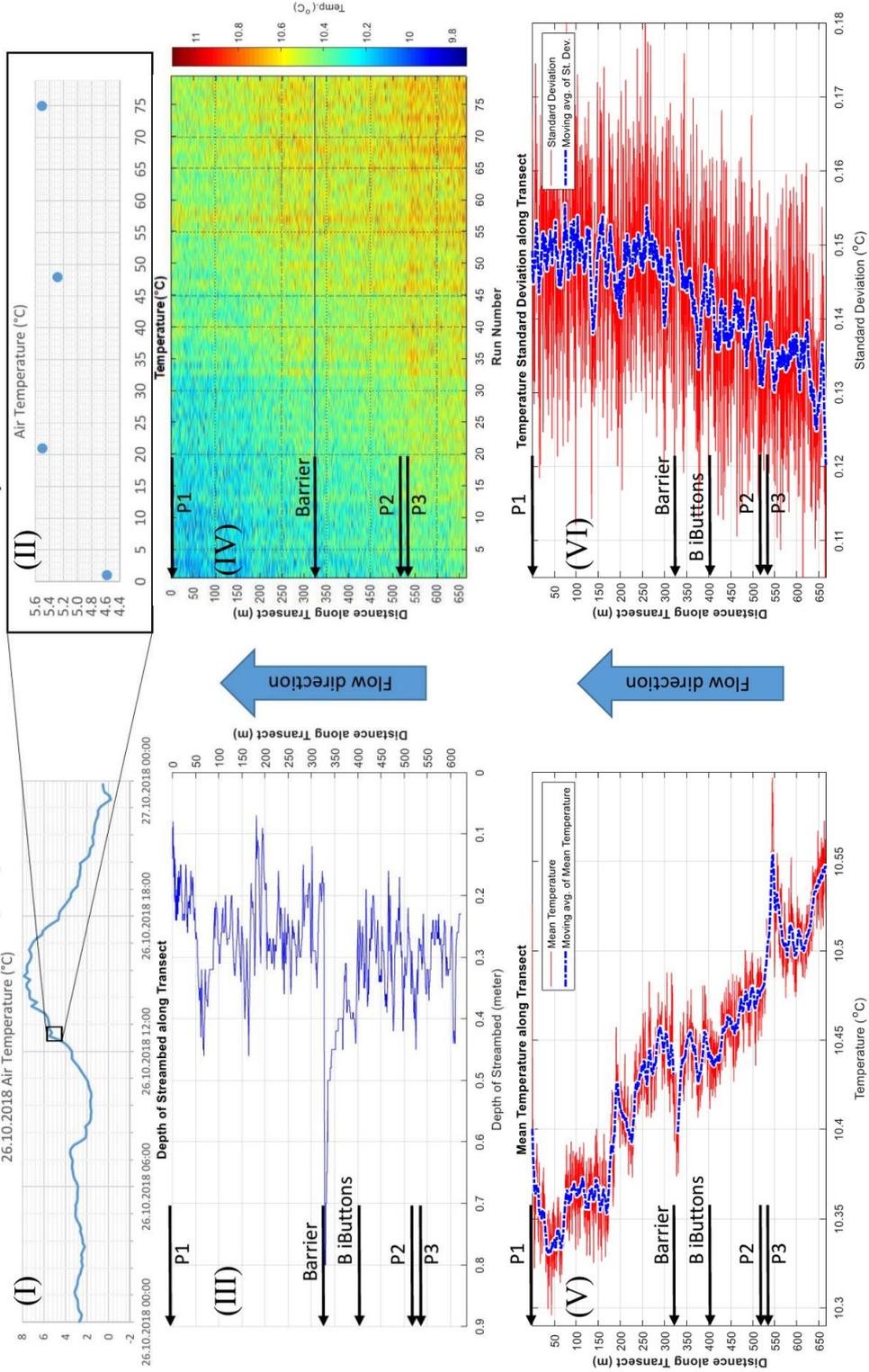
Figure 5.11. DTS measurements taken on 26 October, 2018 12:32 – 13:02

Although an implication of groundwater upwelling is observed close to site P2 and site P3 in all three measurement periods of 26 October, 2018, this marked implications became noisy as the effect of solar radiation increases slowly toward noon time, inducing high variations in temperature profile and hence potentially obscuring the groundwater signal (compare Figure 5.11 and Figure 5.9).

Figure 5.12 presents a more detailed picture of this warm anomaly by comparing the mean temperature values along the transect for the early morning measurement and noon measurement during October 26th, 2018 together with the EC values of streambed sediments inferred from EMI survey conducted on 27 June 2018. It can be seen that the warm temperature anomaly around 550 m closely coincides with the EC anomaly with around 25 m shift downstream, which may be due to inaccuracy in distance measurement. Note also that there are noises at two locations: barrier 328-m, and at 195-m arising with the effect of the solar radiation at noon.

The temperature data only gave information about daily pattern of stream water in June and September measurements. Short period of measurements (30-45 minutes) with high frequency of data recording (for each 23 seconds) possibly decreased the accuracy of the FO-DTS unit, although this decrease was found as insignificant by Selker et al., (2014). Measurement periods with 2 hours or higher could give a higher chance of success in detecting sustained water temperatures using temperature standard deviations (Matheswaran et al., 2014). Moreover, the magnitude of GW-SW exchange can also be determining factor to detect the temporal change of temperature. Under favorable conditions such as low air temperature, no solar radiation and low stream discharge, FO-DTS measurements successfully detected the warm temperature anomaly location which coincided with the high permeable streambed location by the EMI survey.
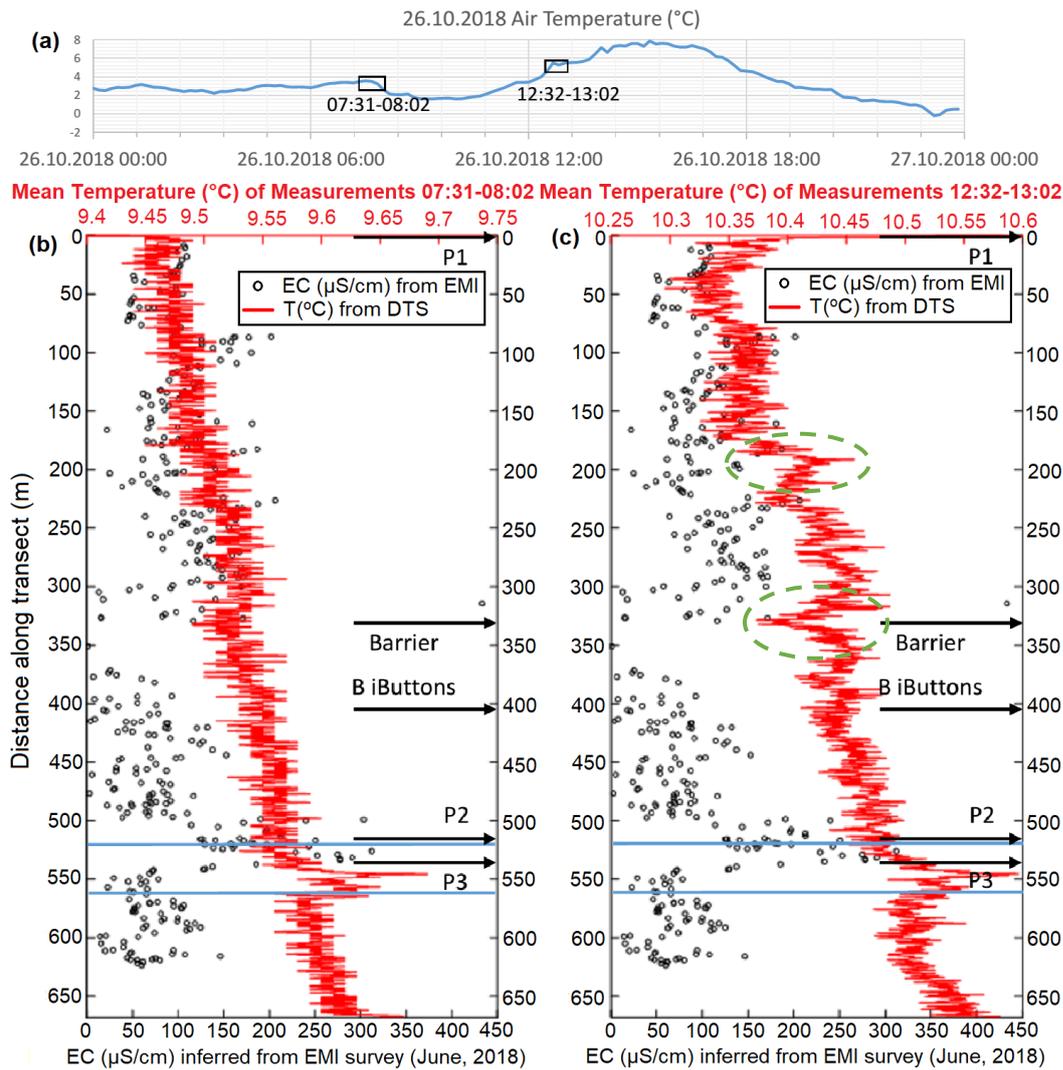
Figure 5.12. (a) air temperature, and EC data inferred from EMI Survey (June, 2018) overlain by mean top-of-the-streambed temperature values measured by the DTS unit on 26.10.2018 (b) at 07:31-08:02, and (c) at 12:32-13:02. Green circles in (c) indicate the effect of sunlight and shading which are not present in (b).

5.3. Nested Piezometers and Vertical Hydraulic Gradient Estimation

VHG (%) values calculated by manual hydraulic head measurements at sites P1, P2 and P3 are tabulated in Table 5.2, Table 5.3 and Table 5.4 respectively. Figure 5.13 shows the time series plot of VHG at sites P1, P2 and P3 for ease of comparison. Table

74

5.2 and Figure 5.13a show consistent positive VHG values at site P1 indicating strong downward flux that is increasing in magnitude from June to November. Site P2 is characterized by consistent upward gradient until September 20, 2018, and shows slight upward and downward gradient based on measurement sets after this date. Moreover the magnitude of the VHG is significantly lower compared to that of site P1. After September 20, 2018 response of the water level after purging at P2-D was very slow which could be due to clogging of P2-D, and the results of VHG estimations were deemed as erroneous after this date (see Table 5.3 and Figure 5.13b). At Site P3 (see Table 5.4 and Figure 5.13c)., VHG values calculated from individual and nested piezometers were consistently negative (-1.6% to -8%) indicating consistent upward flux from June towards the end of September, and became slightly positive (+0.2% to 4.3%) indicating no or minor downward flux in a consistent manner after October 24, 2018. Note that gentle gradients at Sites P2 and P3 increase the sensitivity of the results to the measurement errors.

Table 5.2. *Vertical hydraulic gradient (%) estimations at site P1*

Date	P1-S		P1-D		VHG Estimation from Two nested Piezometers	
	VHG (%)	Vertical Direction	VHG (%)	Vertical Direction	VHG (%)	Vertical Direction
28.06.18 11:30	48.966	Downward		-		-
29.06.18 11:31	52.874	Downward		-		-
30.06.18 12:30	54.713	Downward		-		-
30.06.18 19:45	45.747	Downward		-		-
01.07.18 10:30	46.437	Downward		-		-
01.07.18 18:30	47.356	Downward	27.220	Downward	12.683	Downward
02.07.18 11:15	42.529	Downward	26.146	Downward	12.520	Downward
02.07.18 16:45	42.529	Downward	24.293	Downward	9.431	Downward
18.09.18 10:10	72.414	Downward		-		-
19.09.18 08:06	68.736	Downward	36.683	Downward	13.333	Downward
19.09.18 10:55	69.195	Downward	36.976	Downward	14.634	Downward
20.09.18 09:30	68.276	Downward	36.293	Downward	13.984	Downward
20.09.18 13:12	68.736	Downward	34.439	Downward	12.846	Downward
20.09.18 14:40	62.299	Downward	34.927	Downward	14.146	Downward
03.10.18 13:19	77.471	Downward	42.146	Downward	15.935	Downward
24.10.18 16:47	90.805	Downward	49.951	Downward	19.512	Downward
25.10.18 07:30	89.195	Downward	49.463	Downward	19.024	Downward
25.10.18 12:00	89.195	Downward	48.780	Downward	18.211	Downward
26.10.18 07:55	91.724	Downward	50.732	Downward	19.675	Downward
26.10.18 10:58	92.874	Downward	52.000	Downward	18.699	Downward
26.10.18 12:55	94.943	Downward	50.927	Downward	19.024	Downward
26.10.18 15:30	93.563	Downward	51.024	Downward	19.512	Downward
07.11.18 13:45	89.655	Downward	50.146	Downward	20.163	Downward
07.11.18 15:55	93.793	Downward	51.122	Downward	19.024	Downward

Table 5.3. *Vertical hydraulic gradient (%) estimations at site P2*

Date	P2-S		P2-D		VHG Estimation from Two nested Piezometers	
	VHG (%)	Vertical Direction	VHG (%)	Vertical Direction	VHG (%)	Vertical Direction
28.06.18 17:30	-2.927	Upward	0.842	Downward	-0.370	Upward
29.06.18 13:30	-4.878	Upward	-2.105	Upward	-1.852	Upward
30.06.18 11:30	9.512	Downward	-2.105	Upward	-10.370	Upward
30.06.18 18:45	-0.244	Upward	-2.421	Upward	-3.519	Upward
01.07.18 09:30	7.805	Downward	-	-	-	-
01.07.18 17:30	5.366	Downward	-	-	-	-
02.07.18 10:15	3.659	Downward	1.368	Downward	-2.778	Upward
02.07.18 15:30	1.707	Downward	-	-	-	-
18.09.18 12:15	1.951	Downward	0.000	-	-1.481	Upward
18.09.18 15:41	-	-	-	-	-	-
18.09.18 16:57	-2.195	Upward	-	-	-	-
18.09.18 17:00	-1.707	Upward	-	-	-	-
19.09.18 09:03	-0.732	Upward	-	-	-	-
19.09.18 12:45	-	-	-	-	-	-
19.09.18 16:45	-	-	-	-	-	-
20.09.18 10:14	0.244	Downward	0.211	Downward	0.185	Downward
20.09.18 12:50	-0.732	Upward	-3.053	Upward	-6.852	Upward
20.09.18 15:10	-0.976	Upward	-3.158	Upward	-6.296	Upward
03.10.18 12:30	-2.195	Upward	5.368	Downward	10.370	Downward
24.10.18 17:26	-	-	10.737	Downward	-	-
25.10.18 08:00	-4.146	Upward	11.263	Downward	18.889	Downward
25.10.18 13:52	-1.951	Upward	10.421	Downward	19.444	Downward
26.10.18 11:34	-	-	10.632	Downward	-	-
26.10.18 16:00	-	-	9.895	Downward	-	-
07.11.18 12:02	-	-	11.579	Downward	-	-
07.11.18 16:28	-1.220	Upward	13.053	Downward	21.481	Downward

Table 5.4. *Vertical hydraulic gradient (%) estimations at site P3*

Date	P3-S VHG (%)	P3-S Vertical Direction	P3-D1 VHG (%)	P3-D1 Vertical Direction	P3-D2 VHG (%)	P3-D2 Vertical Direction	VHG of Two nested Piezometers P3-D2 & P3-S VHG (%)	VHG of Two nested Piezometers P3-D2 & P3-S Vertical Direction
19.09.18 09:17		-	-1.071	Upward		-		-
19.09.18 12:19		-	-1.905	Upward		-		-
19.09.18 16:40		-	-1.905	Upward		-		-
20.09.18 10:00	-8.056	Upward	-2.619	Upward	-1.591	Upward	-2.114	Upward
20.09.18 12:30	-8.056	Upward	-4.167	Upward	-1.591	Upward	-1.480	Upward
20.09.18 15:00	-4.167	Upward	-2.619	Upward	-1.705	Upward	-3.594	Upward
03.10.18 12:20	-1.944	Upward	-0.476	Upward	2.045	Downward	-0.211	Upward
24.10.18 17:34	1.667	Downward	0.595	Downward	4.318	Downward	0.000	-
25.10.18 08:15	1.944	Downward	1.548	Downward	2.159	Downward	0.634	Downward
25.10.18 13:35	0.556	Downward	0.238	Downward	2.500	Downward	0.211	Downward
26.10.18 11:26		-	1.071	Downward		-		-
26.10.18 15:53		-	0.238	Downward		-		-
07.11.18 12:50		-	0.595	Downward		-		-
07.11.18 16:12	2.500	Downward	1.190	Downward	3.409	Downward	0.423	Downward

Figure 5.13. Vertical Hydraulic gradient (%) values calculated using manual water level measurements at (a) site P1, (b) site P2, and (c) site P3.

79

To observe the vertical hydraulic gradients at piezometer sites in a continuous manner, HOBO® pressure transducers were installed at selected piezometers and surface water. Water levels were measured every 10 minutes for the period October 27 - November 7, 2018. VHG at Site P3 is calculated using piezometers P3-D and P3-S while VHG at site P2 is calculated using the surface water level data together with piezometer P2-S (Figure 5.14). VHG values at site P3 vary between -0.2% and +1.6% with a more or less diurnal cycle, but the dominant character at this site is downward flux for this period (Figure 5.14a). At Site P2 minor upward flux was evident with VHG values varying narrowly around -0.5% with diurnal cycle (Figure 5.14b).

The results of VHG have shown that while downstream of the study site (P1) was characterized by strong downward flux, the upstream part of the study area, namely P2 and P3 sites, was characterized by lower hydraulic gradient magnitudes changing from upwelling flux towards neutral to slightly downwelling flux starting from late October, 2018.
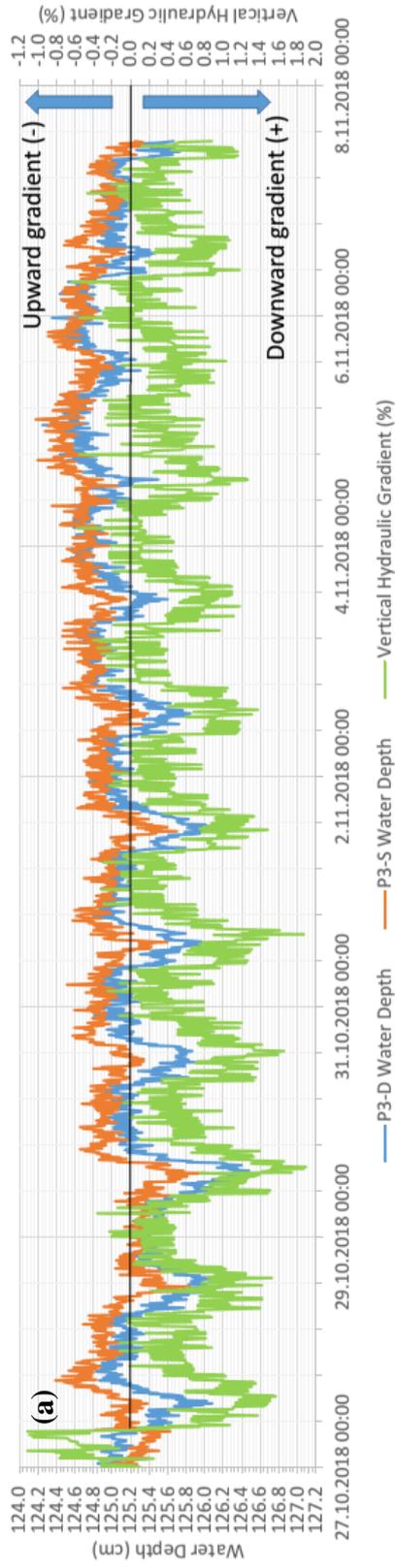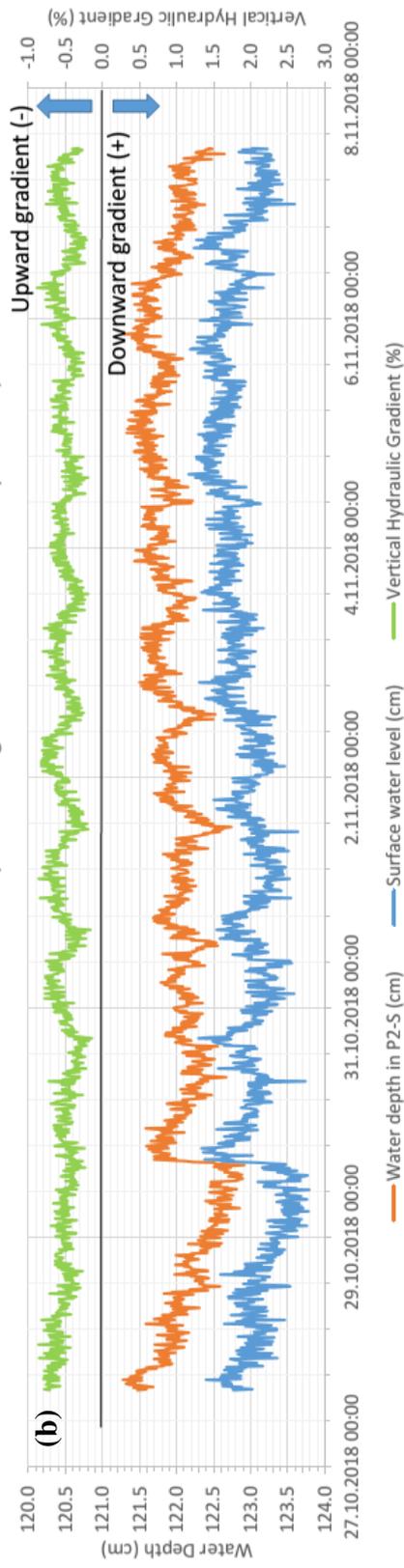
Figure 5.14. Water level measurements using pressure transducers (HOBO) and vertical hydraulic gradient values at (a) Site P3 and (b) Site P2

5.4. Vertical Flux Determination from Vertical Temperature Profile

Diurnal variation in streamed temperature values at various depths were recorded at sites P1, P2 and P3 for three measurement periods (Table 5.5). High temperature difference between minimum and maximum values at the depth of 17 cm indicated that downwelling is the predominant behavior at site P1. For the site P3, low temperature difference between minimum and maximum temperature measurements were recorded in both September, and October measurement periods which indicates that there is no important change in the behavior of vertical flux. However, temperature difference of P2 has increased in October compared to September measurement period which can be interpreted as the behavior of vertical flux at site P2 has changed starting from October, 2018. Site B which was investigated on October measurement period was also characterized by low temperature difference.

Table 5.5. *Maximum and minimum temperature measurements of iButton Thermochrons at corresponding depths and measurement periods*

Site	Measurement Period	Depth (cm)	Max (°C)	Min (°C)
P1	06.28.2018 - 07.02.2018	2	21,19	12,93
		17	18,64	14,32
P2	09.18.2018 - 10.03.2018	2	16,77	11,95
		9	15,87	12,74
		17	14,88	13,19
	10.26.2018 - 11.07.2018	2	13,67	8,46
		17	12,14	9,94
P3	09.18.2018 - 10.03.2018	2	16,65	12,26
		9	16,15	12,95
		17	15,53	13,40
	10.26.2018 - 11.07.2018	2	14,14	8,31
		9	13,49	8,66
		17	14,82	13,25
B	10.26.2018 - 11.07.2018	2	14,14	9,07
		17	13,58	12,46

Vertical fluid flux values were estimated from diurnal temperature variations at two different depths using the amplitude method of Hatch et al., (2006). The results of the vertical fluid flux estimations using vertical temperature profile data obtained from iButtons are illustrated in Figure 5.15-Figure 5.20. These figures show the graphs of air temperature data (Graph I) obtained from Ulukışla meteorological station, raw temperature time series (Graph II), filtered temperature time series (Graph III), amplitudes of the temperature data (Graph IV) and the resulting vertical fluid flux estimation (Graph V) based on Hatch Amplitude method. While raw temperature time series (Graph II) is the data measured by the iButtons, filtered data (Graph III) are the resampled and filtered version of the original raw data, amplitudes (Graph IV) are the real components of the resampled data and the vertical flux estimation (Graph V) (Hatch Amplitude) is estimated using the VFLUX program (Gordon et al., 2012). In order to eliminate the edge effect, the flux estimates for the first and last day of temperature measurements were removed. Note that vertical heterogeneity in the streambed sediments potentially increases the uncertainty in the flux estimates.

For the flux calculation to be reliable, the amplitude of the temperature signal should be greater than the sensor precision (0.0625 °C for the iButtons). Amplitudes lower than sensor precision may thus result in unreliable flux estimations as seen in flux estimates obtained from site P3 in September at a depth of 13 cm (Figure 5.17). Therefore, flux estimates at site P3 in September at the depth of 13 cm were not taken into account but are shown in Figure 5.17 for information. However, it is also important to note that low amount of diurnal variations with temperature values close to the temperature of groundwater can be considered as the sign of strong upwelling. Summary of the vertical flux estimates can be seen in Table 5.6 for the measurement periods.
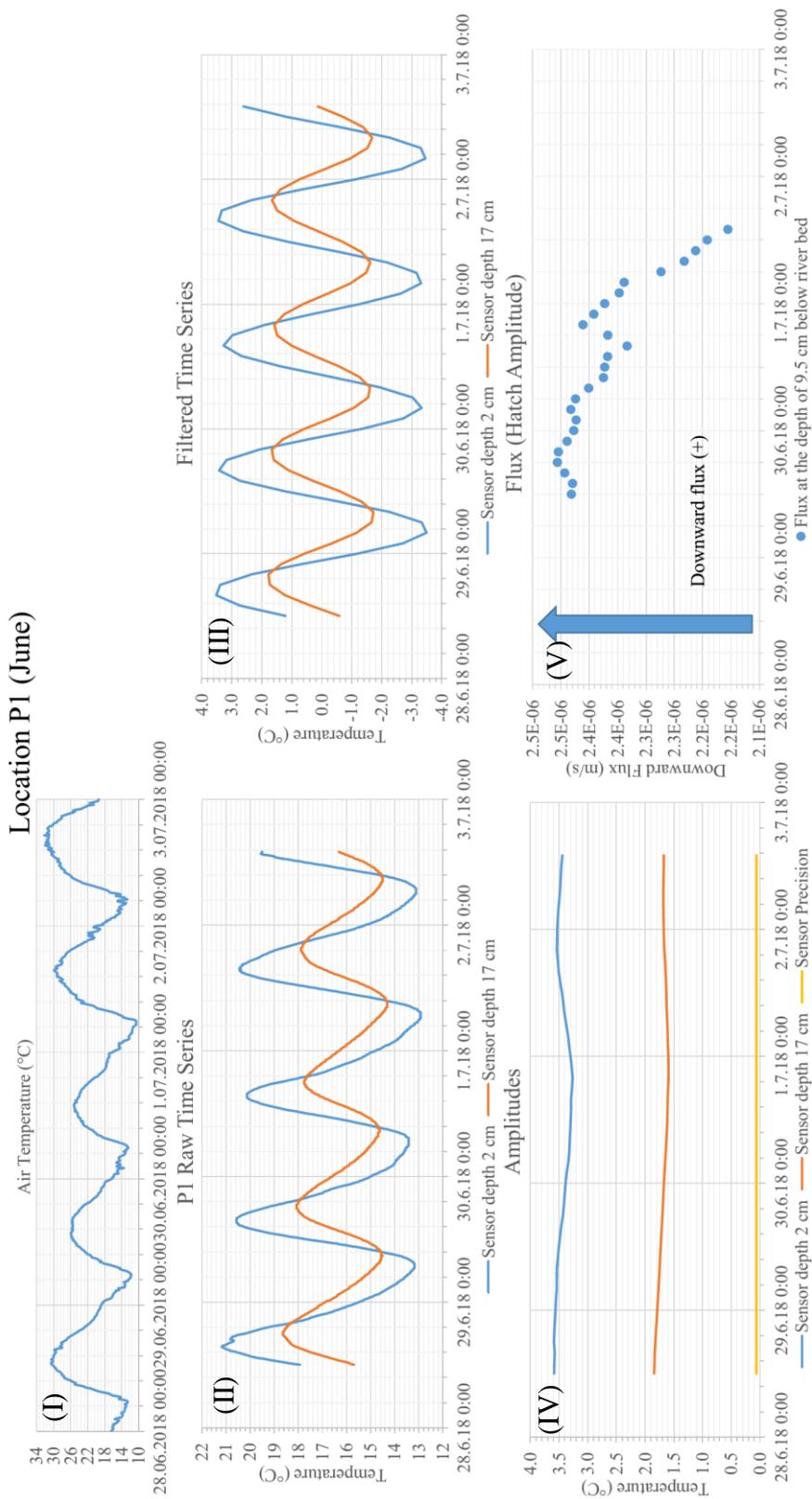
Figure 5.15. Vertical water flux analysis for site P1 in June 2018

84
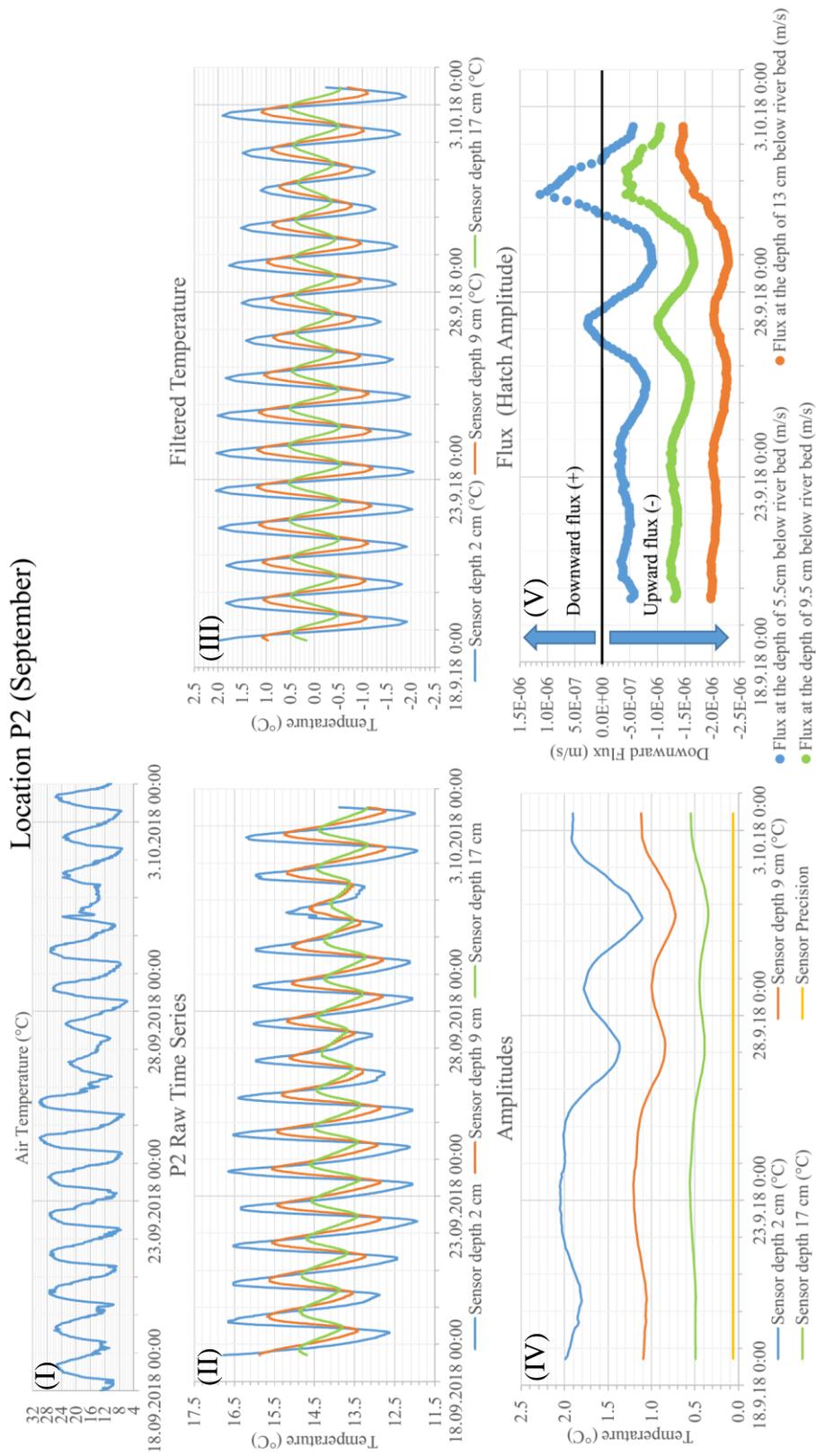
Figure 5.16. Vertical water flux analysis for site P2 in September, 2018
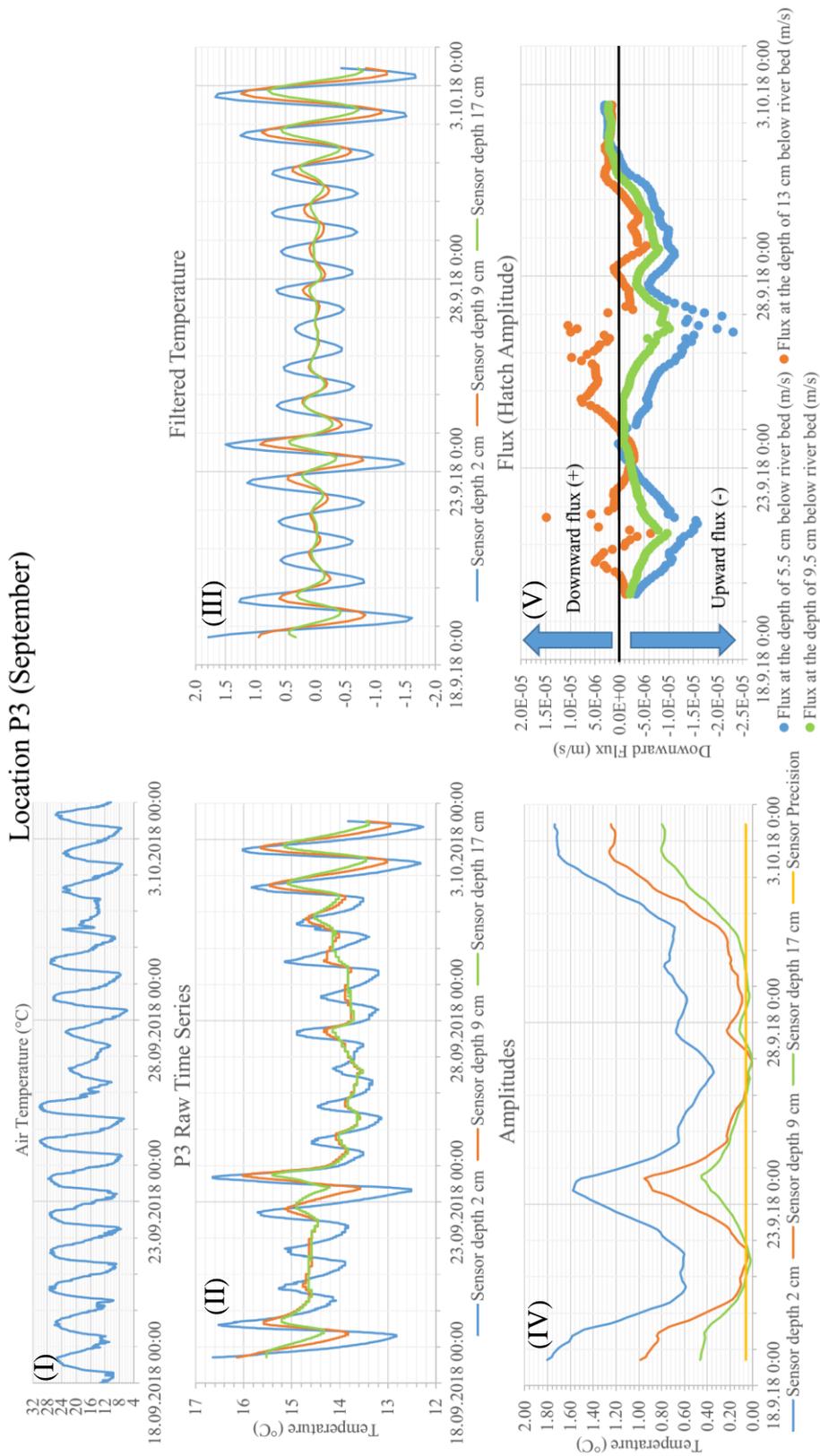
Figure 5.17. Vertical water flux analysis for site P3 in September, 2018
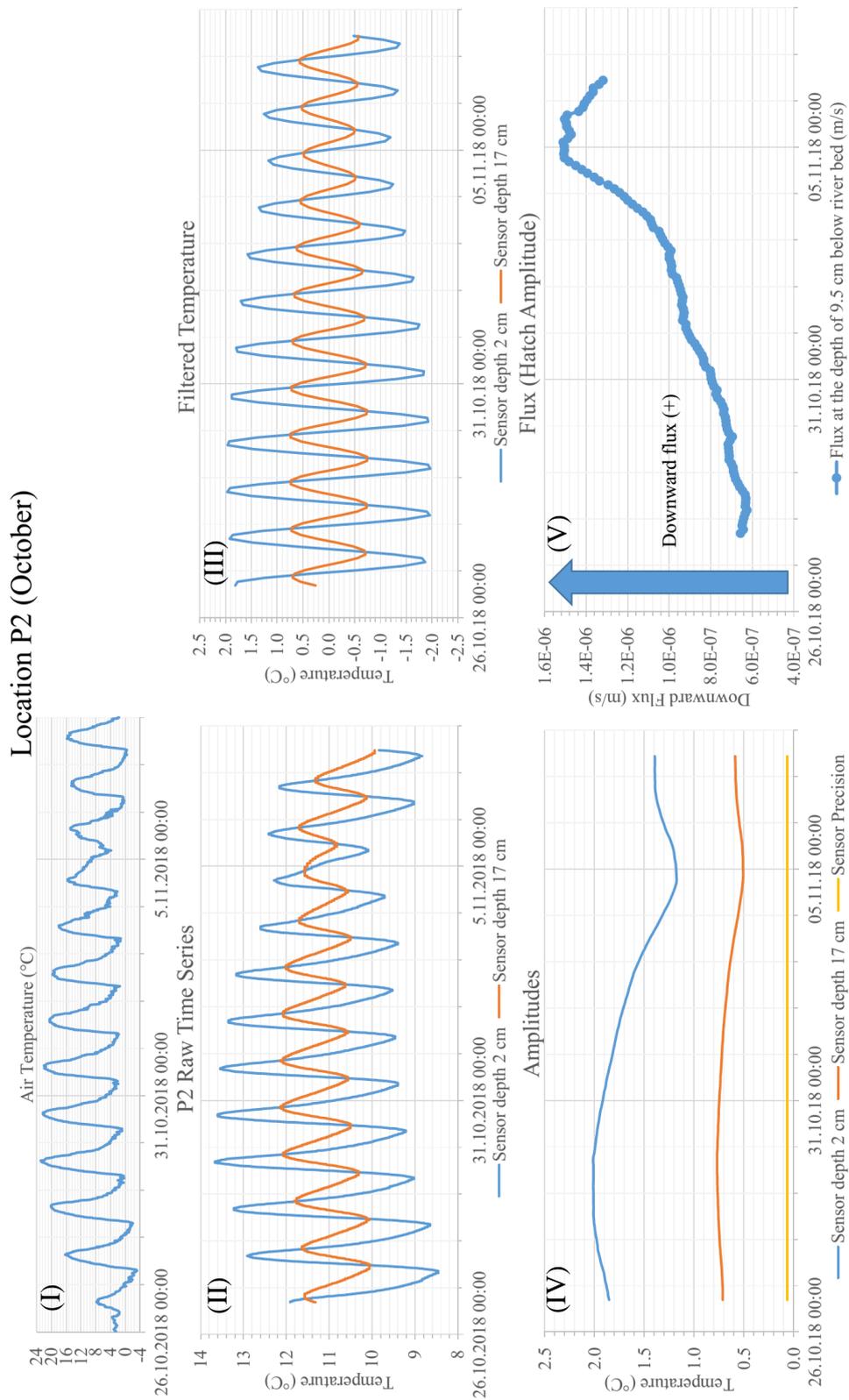
Figure 5.18. Vertical water flux analysis for site P2 in October, 2018
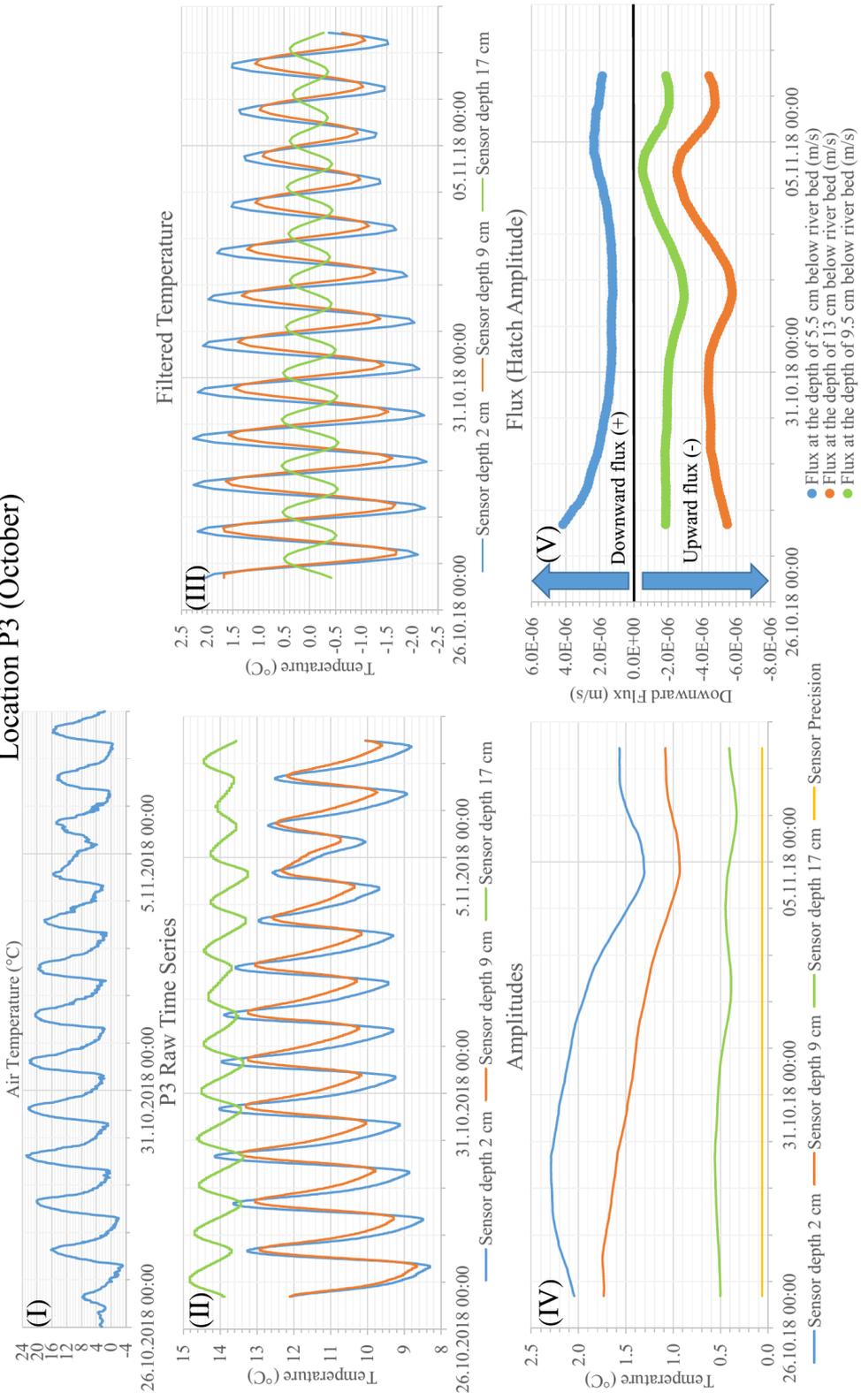
Figure 5.19. Vertical water flux analysis for site P3 in October, 2018
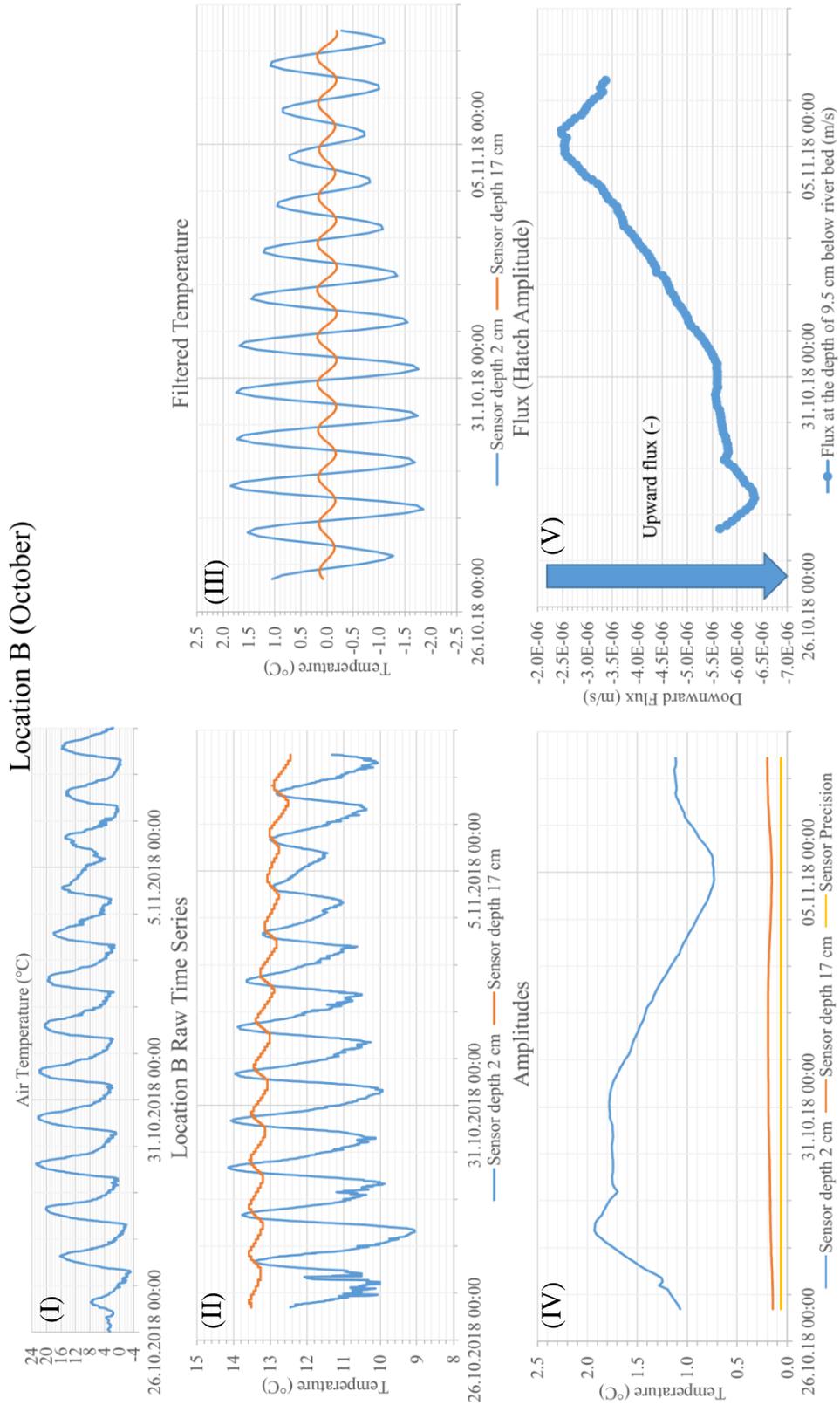
Figure 5.20. Vertical water flux analysis for site B in October, 2018

89

Table 5.6. *Summary of vertical water flow estimates*

Time Period	Site	Depth below top of streambed (cm)	Vertical flux (m/s)	Flow direction
28.06.2018 - 02.07.2018	P1	9.5	$(+2.2 \times 10^{-6})$ - $(+2.5 \times 10^{-6})$	Downward
18.09.2018 - 03.10.2018	P2	9.5	(-5×10^{-7}) - (-2×10^{-6})	Upward
	P3	5.5	(-1×10^{-6}) - (-1×10^{-5})	Upward
26.10.2018 - 07.11.2018	P2	9.5	$(+6 \times 10^{-7})$ - $(+1 \times 10^{-6})$	Downward
	P3	9.5	(-2×10^{-6}) - (-3×10^{-6})	Upward
	B	9.5	(-4×10^{-6}) - (-6×10^{-6})	Upward

Since Site P1 is characterized by strong downward vertical hydraulic gradients from piezometers, temperature-based vertical flux was only estimated in June 2018 and indicated downward fluid flux ranging between 2.2×10^{-6}-2.5×10^{-6} m/s (see Figure 5.15). In September 2018, flux estimates at location P2 range between 5×10^{-7} - 2×10^{-6} m/s in the upward direction (Figure 5.16). Again in September 2018, flux estimates at location P3 - considering temperature data at the depth of 2 cm and 9 cm are reliable – range between 1×10^{-6} – 1×10^{-5} m/s in upward direction at a depth of 5.5 up to end of September, and this behavior has changed to slightly downward direction at early days of October (See Figure 5.17). When flux estimates at sites P2 and P3 are compared, it can be seen that much stronger upwelling is evident at site P3. In October 2018, the flux behavior at location P2 and P3 has changed in response to the changing seasonal conditions. While flux behavior at P2 was in upward direction in September, this has changed to downward direction in October (Figure 5.18) with values ranging between 6×10^{-7} – 1×10^{-6} m/s downward direction at a depth of 9.5 cm for the 28.10.2018-02.11.2018 period. An increase in the magnitude of downward flux is evident through time during this period. Moreover, upward flux is still observed in P3 in October, but an evident decrease was observed in the amount of upward flux. Flux estimates of P3 range around 2×10^{-6} – 3×10^{-6} m/s in upward direction at the depth of 9.5 cm in between

the dates of 28.10.2018-02.11.2018 (Figure 5.19). Lastly, flux estimates at site B range between $4x10^{-6}$ – $6x10^{-6}$ m/s upward direction at a depth of 9.5cm between the dates of 28.10.2018-02.11.2018 (Figure 5.20).

5.5. Analyses of Water Quality Parameters in Surface Waters and Piezometers

Electrical conductivity (25 °C) and temperature variations in surface waters, and piezometers (middle of the screen) were investigated using Solinst® TLC Meter. Temperature and EC measurements normalized to 25 °C for sites P1, P2 and P3 are shown respectively in Table 5.7, Table 5.8 and Table 5.9, and all measurements are illustrated together in Figure 5.21.

For site P1, EC values representing surface water and piezometers are consistent with each other and slightly increases from June (1051-1302 µS/cm) through October (1410-1717 µS/cm) as the water temperature gets cooler. At site P2, EC values measured from shallow piezometer (P2-S) and surface water are close to each other, P2-S having slightly higher EC values compared to surface water. While EC values measured from P2-S and P2-D agree well in June-July field work, EC values measured from P2-D become significantly lower (vary between 878-980 µS/cm) compared to that of P2-S (vary between 1393-1549 µS/cm) and surface water (vary between 1397-1694µS/cm) starting from September field work. This difference in EC values could be due to the clogging of P2-D piezometer, because the response of the water level after purging was also very slow. At site P3, EC measurements from shallow and deep piezometers were close to each other and varied between 1532-1665µS/cm, while being higher than that of surface water in September. When different sites are compared, it can be seen that the EC values in piezometer at Site P2 is consistently lower than piezometers at P1 and P3. Another difference is marked by transition from September to October; while EC values in piezometers at site P1 and surface waters increase from September to October, EC values in piezometers at Site P2 and P3 increase in this period. EC values in September at P3-S and P3-D were slightly higher than that of surface water in September.

91

Table 5.7. *EC (@ 25 °C) and temperature (°C) measurements at site P1. Note that SW is surface water.*

Date	P1-S EC and Temperature		P1-D EC and Temperature		SW EC and Temperature	
	EC (μS/cm)	T (°C)	EC (μS/cm)	T (°C)	EC (μS/cm)	T (°C)
28.06.18 11:30	1051.2	16	1080.8	18.3	1055.9	17.9
29.06.18 11:31	1179.0	15.5	1142.5	17.1	1152.6	16.6
30.06.18 12:30	1262.4	15.4	1160.7	16.7	1249.4	16.7
30.06.18 19:45	1260.0	17.5	1232.9	17.5	1264.8	17.3
01.07.18 10:30	1294.2	14.6	1303.5	14.7	1284.5	14.9
01.07.18 18:30	1193.2	19	1167.4	19.5	1189.9	19.5
02.07.18 11:15	1302.5	15.5	1267.0	16.2	1223.3	17.1
02.07.18 16:45	1219.3	19	1215.6	20	1199.3	19.9
18.09.18 10:10	1477.7	15.4			1519.1	14.2
19.09.18 08:06	1533.5	13.8	1534.8	13.8	1576.7	12.8
19.09.18 10:55	1516.6	14.2	1493.7	14.9	1488.8	15
20.09.18 09:30	1469.2	13.9	1480.9	14.3	1467.8	13.8
20.09.18 13:12	1440.8	14.7	1433.8	15.8	1382.1	17.4
20.09.18 14:40	1440.1	15.1	1423.5	16.2	1389.2	17.4
03.10.18 13:19	1509.0	13.8	1491.1	14.2	1442.5	15.9
24.10.18 16:47	1552.5	13.1			1411.3	15
25.10.18 07:30	1576.7	12.8			1630.1	11.9
25.10.18 12:00	1583.8	12.6			1595.2	12.3
26.10.18 07:55	1644.0	11.1	1620.2	11.6	1717.8	9.9
26.10.18 10:58	1650.8	10.8	1614.6	11.2	1700.0	10
26.10.18 12:55	1652.7	10.7	1619.8	11.3	1662.5	10.7
26.10.18 15:30	1636.1	11	1525.9	11.7	1544.8	11.8
07.11.18 13:45	1649.6	10.1			1549.7	12.2
07.11.18 15:55	1579.2	11			1529.0	12.9

Table 5.8. *EC (@ 25 °C) and temperature (°C) measurements at site P2. Note that SW is surface water.*

Date	P2-S EC and Temperature		P2-D EC and Temperature		SW EC and Temperature	
	EC (µS/cm)	T (°C)	EC (µS/cm)	T (°C)	EC (µS/cm)	T (°C)
28.06.18 17:30	1109.4	16.6	1125.6	15.2	1009.8	20.8
29.06.18 13:30	1159.4	16.1	1189.7	14.8	1080.8	20.2
30.06.18 11:30	1209.0	15.2	1201.8	14.4	1259.2	15.9
30.06.18 18:45	1261.0	15.8	1251.3	14.6	1243.0	18
01.07.18 09:30	1332.9	14.8	1315.1	14.2	1300.0	14
01.07.18 17:30	1259.7	16.2	1262.6	14.8	1165.9	19.9
02.07.18 10:15	1311.7	15.1	1283.2	14.2	1277.5	15.9
02.07.18 15:30	1315.1	16.1	1246.2	14.6	1183.2	20.3
18.09.18 15:41	1520.2	14.7	878.8	14.6	1407.8	17.3
18.09.18 16:57	1518.8	14.8	885.5	14.3	1434.1	16.7
18.09.18 17:00			885.8	14.4		
19.09.18 09:03	1549.0	13.8	906.9	14.2	1557.6	13.2
19.09.18 12:45	1520.2	14.6	900.5	14.7	1423.4	16.8
19.09.18 16:45	1517.6	14.7	902.8	14.6	1441.0	16.5
20.09.18 10:14	1537.2	14	917.1	14.2	1459.3	14.3
20.09.18 12:50	1522.7	14.6	913.7	14.4	1397.6	17
20.09.18 15:10	1513.9	14.7	914.8	14.3	1399.0	17.1
03.10.18 12:30	1455.0	13.9	931.9	13.9	1461.4	15.2
24.10.18 17:26	1393.4	13	938.3	13.1	1508.8	14.6
25.10.18 08:00	1424.9	12.3	948.5	12.9	1634.1	11.9
25.10.18 13:52	1413.8	12.7	949.9	12.9	1575.4	12.8
26.10.18 11:34			974.4	12.1	1694.3	10
26.10.18 16:00			964.1	12.6	1609.5	12
07.11.18 12:02	1504.2	10.8	994.5	11.2	1588.2	11.3
07.11.18 16:28	1484.8	11.1	980.9	11.7	1555.7	12.7

Table 5.9. *EC (@25 °C) and temperature (°C) measurements at site P3. Note that SW is surface water.*

Date	P3-S EC and Temperature		P3-D1 EC and Temperature		P3-D2 EC and Temperature		SW EC and Temperature	
	EC (μS/cm)	T (°C)	EC (μS/cm)	T (°C)	EC (μS/cm)	T (°C)	EC (μS/cm)	T (°C)
19.09.18 09:17			1394.3	15.2			1541.5	13.6
19.09.18 12:19	1608.9	15.4	1256.1	15.8	1540.3	15.9	1432.7	16.6
19.09.18 16:40	1604.9	16	1298.5	15.7	1613.9	15.4	1433.9	16.6
20.09.18 10:00	1665.4	14.3	1258.7	15.2	1630.9	15.1	1478.3	14.2
20.09.18 12:30	1641.8	15.2	1285.2	15.5	1655.5	15.2	1396.9	16.7
20.09.18 15:00	1623.8	15.4	1318.2	15.7	1640.7	15.5	1386.3	17.2
03.10.18 12:20	1616.7	14	1321.2	14.7	1585.2	14.9	1501.3	14.1
24.10.18 17:34	1532.5	13.5	1325.7	14.3	1534.4	14.2	1511.4	14.4
25.10.18 08:15	1585.8	12.3	1360.8	13.8	1551.5	13.8	1635.5	11.9
25.10.18 13:35	1560.7	12.9	1502.6	13.8	1541.0	14	1576.7	12.8
26.10.18 11:26			1497.4	13			1696.6	10.1
26.10.18 15:53			1369.8	13.8			1391.9	12
07.11.18 12:50	1598.6	11	1512.0	12.6	1590.2	12.7	1569.1	11.9
07.11.18 16:12	1553.3	11.6	1381.2	13.3	1571.2	12.9	1535.6	12.9

Temperature measurements of P1-S (10.7 – 19.0 °C) and P1-D (11.2 – 20.0 °C) are very close to each other during the whole measurement period, and temperature measurements of both piezometers show that surface water affects piezometer measurements which can be inferred as downward water flow is dominant. In sites P2 and P3, deep and shallow piezometers show different thermal behavior than surface water with relatively sustained temperatures compared to P1 temperature measurements. P2-D temperature measurements show very close temperature results to groundwater temperature during June and July measurements. Although, P2-D shows the sign of clogging starting from September, measurements still implies that there is upwelling controlling the temperature of deep piezometer levels until November. In the same way, temperature of P2-S is also close to temperature of groundwater, which is approximately 14.0 °C. However, temperature measurements of both P2-S and P2-D become closer to surface water in November measurements, which can be inferred that direction of vertical water flow change from upwelling to

downwelling with the effect of seasonal changes. Similar temperature recordings are observed in P3 with little differences compared to P2. Deep piezometers of P3 still show the sign of upwelling in November measurements, while temperature measurements of P3-S are closer to surface water temperature, which can be implied as rate of upwelling decreased in P3 after October.
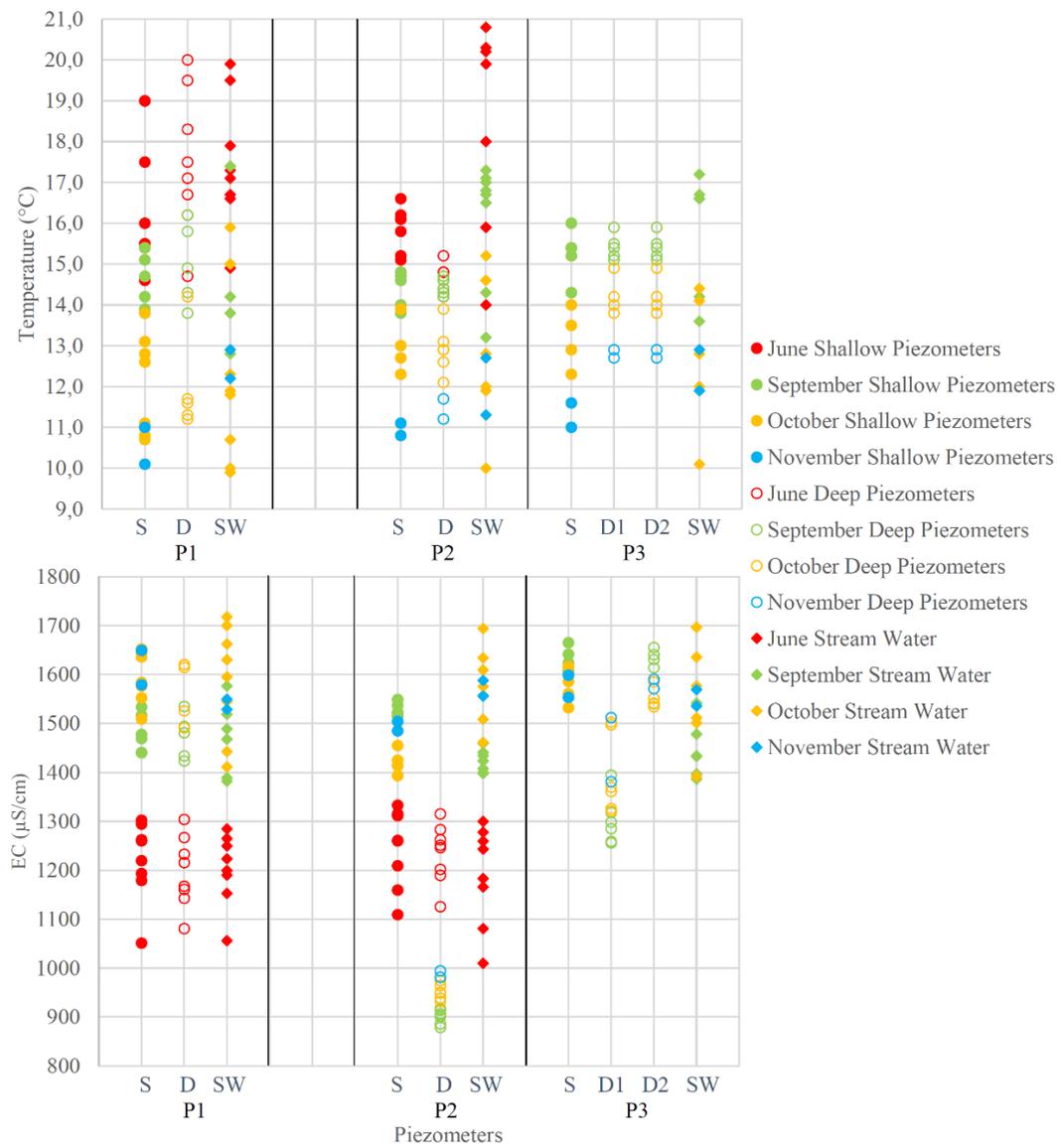
Figure 5.21. EC (25 °C) and temperature measurements from piezometers and stream water

CHAPTER 6

CONCLUSIONS AND RECOMMENDATIONS

The objective of this study was to quantify the spatio-temporal distribution of the GW-SW exchange fluxes along the Çakıt Stream. The study was conducted in a hierarchical manner, starting from the basin scale towards the stream reach scale. First, water quality analyses and geological information were utilized understand the general characteristics of the water flow path at the basin scale. Secondly, small stream reach scale study was conducted to identify GW-SW exchange using electromagnetic induction surveys, fiber-optic distributed temperature sensing technology, nested piezometers to estimate vertical hydraulic gradient, iButton temperature loggers constructing vertical temperature profiles and hence estimation of vertical fluid fluxes, and analyses of water quality parameters.

6.1. EMI Survey and FO-DTS Technology

The study has shown that EMI survey is an efficient and effective method to identify high permeability zones within the streambed sediments which may indicate the groundwater surface water exchange locations. EMI survey was conducted using Multi-depth Electromagnetic Conductivity Meter (GF Instruments) with the CMD-1 probe. This probe is only capable of taking measurements at single depth. However, performing EMI survey at multiple depths would provide a stronger conceptualization of the streambed with permeable zones (Binley et al., 2013; Rejiba et al., 2018).

 EMI survey requires precise positioning system. For EMI surveys performed in September and October, 2018, the coordinate information were sometimes not satisfying due to the distorted coordinates of the data. Under cloudy and rainy weather conditions, GPS devices (even with high sensitivity) can fail to give exact position in

highly vegetated areas, and therefore weather conditions need to be considered for the techniques that requires highly sensitive coordinate data.

FO-DTS application provided a promising result using mean temperature method under cold weather (winter) and low streamflow conditions. Each FO-DTS measurement period used in this study was limited to 30 minutes due to battery limitations. Higher measurement period intervals, for example 2 hours or more, would provide more detailed information (Matheswaran et al., 2014). The method used in this study was successful to detect an upwelling location. However, observation of transient conditions such as rain events and floods would be also useful to detect downwelling location (Gaona et al., 2019).

The results obtained from FO-DTS technology supported the results obtained from EMI surveys. A major anomaly location with high EC results inferred from EMI survey was assumed to have high permeability and hence potential to have GW-SW interaction. Acquiring temperature anomaly at the same location showed how FO-DTS application can be a complimentary method for the EMI survey. However, a marked difference in the temperature of groundwater and stream water, low discharge rates (proper seasonal conditions), minimizing the effect of solar radiation/shading effects are important factors to achieve successful FO-DTS data. Our study have shown that FO-DTS data can be inconclusive when one or more of these factors were not met. Position of the fiber-optic cable was recorded during the deployment using a handheld GPS tracker, and this resulted with bias about the cable location. A small distortion with one percent of a total length can be resulted in 10 meters long distortion of the cable. Therefore, positioning of the fiber-optic cable is an important issue that require high attention to get better results. Use of a GPS device with a higher sensitivity can be better to locate the position of the fiber-optic cable instead of handheld GPS trackers. The FO-DTS measurements were conducted with the highest capacity of the DTS unit in terms of spatial resolution (25 centimeters) and temporal resolution which is 23 seconds (when the DTS unit is used with 1-km-long fiber-optic cable) because of the limited battery capacity. If the energy issues can be resolved

during the field measurements of FO-DTS, configuring the optimum calibration properties in terms of temporal resolution and spatial resolution can enhance the accuracy of the temperature data. Therefore, a station supported by continuous energy (like solar panels) for DTS measurements can be more beneficial than batteries to be able to monitor the suitable conditions in extended time periods.

6.2. Point-Based Methods

The vertical flux values estimated from iButton thermochrone temperature logging sensors and vertical hydraulic gradient values obtained by nested piezometers provided important quantitative insight for the stream reach at point scale (Constantz, 2008; Kalbus et al., 2006). However, it is also important to remind that point-based data collection methods can be insufficient to represent a region and increasing the point-based data collection locations can be rather time consuming (Conant, 2004). At this point, coupling the DTS application and point-based methods in this study offered more robust results.

Vertical flux estimates obtained by vertical temperature profiles indicated upward water flow direction in location P2, P3 and B. Vertical water flow direction changes from upward direction to downward direction in location P2 after October. These results were also supported by piezometers. Coupling the two point-based methods strengthened our deduction that behavior of the interaction between groundwater and stream water changes gradually with seasonal change at upstream of the study area from upward water flux direction to the downward direction. The material that we used for piezometers was high density polyethylene (HDPE) pipes. Using HDPE pipes can be beneficial for water-quality measurements since they are corrosion-resistant and they are environment-friendly since they are made from recycled materials. However, it is important to notice that HDPE pipes are flexible and hence could distort water level measurements if not properly fixed. Therefore, fixing the shape of piezometer made by HDPE pipe or similar materials, which is flexible, is an important issue that requires attention for water level measurements through piezometers.

Estimation of vertical fluid flux from vertical temperature profiles requires a set of assumptions to be made. One of the major assumptions in this study was to assign homogeneous vertical structure to streambed, which means that thermal and sediment properties were constant and set at typical streambed properties (Gordon et al., 2012). Laboratory tests such as sediment core analysis and hydraulic conductivity tests [e.g., Binley et al., 2013] could provide better insight to determine streambed properties, and a complex modeling with multilayers in vertical direction could give better results.

6.3. Water Quality Studies

Water-quality studies have shown that surface water at upstream of Çakıt Stream is heavily affected by gypsum units and gypsum units cause to increase in EC values of surface water. Furthermore, being aware about the geology of the basin provided strong insights for the application of the reach-scale methods. EC and temperature recordings enhanced the conceptualization of seasonal changes. Our study has also shown that the relation between geology and water-quality properties cannot be neglected in hydrological studies.

6.4. Conclusion

In summary, the results indicated that the studied stream reach show different characteristics at downstream and upstream parts. While downwelling is the all-time dominant behavior for the downstream of the study reach, upwelling is the dominant behavior at some locations of upstream part of the study reach and varies in response to seasonal variation in surface water levels and groundwater levels.

The study has shown that EMI which can be conducted along long stream reaches in short time intervals is a strong reconnaissance method. Moreover, FO-DTS is a promising method in hydrological studies since it offers continuous observations in time and space. EC anomaly location (showing highly permeable streambed) obtained from EMI survey coincided with temperature anomaly location obtained from the FO-DTS technology. Coinciding anomaly results obtained from both EMI survey and FO-DTS can be considered as one of the most important finding of this study. The

study has also shown that point-based methods which are vertical hydraulic gradient estimation from hydraulic head measurements, vertical flux estimation from temperature time series and water quality measurements from nested piezometers are essential methods for hydrological studies since they provide quantitative results and they enhance the conceptualization of GW-SW interaction.

Finally, the use of different set of techniques that are sensitized to different space and time scales in a hierarchical manner improves the characterization of GW-SW interaction processes that are known to be highly heterogeneous in space and time. Especially, combining point-based methods that are highly capable of quantifying vertical water exchange fluxes with the methods that provide continuous data both in space and time reduce the uncertainties and provide higher confidence in estimated exchange fluxes at the reach-scale.

REFERENCES

Anderson, M. P. (2005). Heat as a ground water tracer. *Ground Water*, 43, no. 6: 951-968, doi.org/10.1111/j.1745-6584.2005.00052.x.

Archie, G. E. (1942). The electrical resistivity log as an aid in determining some reservoir characteristics. *Trans. Am. Inst. Min. Metal. Pet. Eng.*, 54-62.

Baxter, C., Hauer, F. R., and Woessner, W. W. (2003). Measuring groundwater–stream water exchange: new techniques for installing minipiezometers and estimating hydraulic conductivity. *Transactions of the American Fisheries Society*, 493-502.

Binley, A., Hubbard, S. S., Huisman, J. A., Revil, A., Robinson, D. A., Singha, K., and Slater, L. D. (2015). The emergence of hydrogeophysics for improved understanding of subsurface processes over multiple scales. *Water Resour. Res.*, 51, 3837–3866, doi:10.1002/2015WR017016.

Binley, A., S. Ullah, A. L. Heathwaite, C. Heppell, P. Byrne, K. Lansdown, M. Trimmer, and H. Zhang (2013), Revealing the spatial variability of water fluxes at the groundwater-surface water interface. *Water Resour. Res.*, 49, 3978-3992, doi:10.1002/wrcr.20214.

Bredehoeft, J. D., and Papaopulos, I. S. (1965). Rates of vertical groundwater movement estimated from the Earth's thermal profile. *Water Resour. Res.*, 1, 325-328, https://doi.org/10.1029/WR001i002p00325.

Briggs, M. A., Lautz, L. K., and McKenzie, J. M. (2012). A comparison of fibre-optic distributed temperature sensing to traditional methods of evaluating groundwater inflow to streams. *Hydrol. Process.*, 26, 1277-1290, DOI: 10.1002/hyp.8200.

Brodie, R., Sundaram, B., Tottenham, R., Hostetler, S., and Ransley, T. (2007). *An Overview of Tools for Assessing Groundwater-Surface Water Connectivity.* Canberra: Bureau of Rural Sciences.

Brunke, M., and Gonser, T. (1997). The ecological significance of exchange processes between rivers and groundwater. *Freshwater Biology, 37*(1: 1-33), 1-33.

Candela, L., and Morell, I. (2009). GROUNDWATER – Vol. II – Basic Chemical Principles of Groundwater. *Encyclopedia of Life Support Systems*, 43-55.

Carter, R. W., and Davidian, J. (1968). *General procedures for gaging streams.* U.S. Geol. Surv. Techniques of Water Resources Investigations, Book 3, Chapter A-6, 1968.

Casas, J. R., and Cruz, P. J. (2003). Fiber Optic Sensors for Bridge Monitoring. *Journal of Bridge Engineering*, DOI: 10.1061/~ASCE!1084-0702~2003!8:6~362!

Chebotarev, I. I. (1955). Metamorphism of natural waters in the crust of weathering. *Geochim. Cosmochim. Acta*.

Clark, M., and Robertson, A. (2005). Uppermost Cretaceous - Lower Tertiary Ulukışla basin, south-central Turkey: sedimentary evolution of part of a unifid basin complex within an evolving Neotethyan suture zone. *Sediment Geol*, 173: 15-51.

Conant, J. B. (2004). Delineating and quantifying ground water discharge zones using streambed temperatures. *Ground Water*, 243-257.

Constantz, J. (2008). Heat as a tracer to determine streambed water exchanges. *Water Resour. Res.*, 44, W00D10, doi:10.1029/2008WR006996.

Covino, T. P., and McGlynn, B. L. (2007). Stream gains and losses across a mountain-to-valley transition: Impacts on watershed hydrology and stream water chemistry. *Water Resour. Res.*, 43, W10431, doi:10.1029/2006WR005544.

104

Cox, M. H., Su, G. W., and Constantz, J. (2007). Heat, Chloride, and Specific Conductance as Ground Water Tracers near Streams. *Ground Water*, 45, 187-195.

Crook, N., Binley, A., Knight, R., Robinson, D. A., Zarnetske, J., and Haggerty, R. (2008). Electrical resistivity imaging of the architecture of substream sediments. *Water Resour. Res.*, 44, W00D13, doi:10.1029/2008WR006968.

Darcy, H. P. (1856). *Les fountaines publiques de la Ville de Dijon.* Paris: Victon Dalmont.

Demirtaşlı, E., Bilgin, A. Z., Erenler, F., Işıklar, S., Sanlı, Y., Dilaver, S. M., and Turhan, N. (1975). Bolkardağlarının jeolojisi. *Cumhuriyetin 50. Yılı, Yer Bilimleri Kongresi Tebliğler Kitabı* (pp. 42-57). Ankara, Turkey: MTA.

Demirtaşlı, E., Turhan, N., Bilgin, A. Z., and Selim, M. (1984). Geology of the Bolkar Mountains. *Geology of the Taurus Belt Proceedings International Symposium on the Geology of the Taurus Belt* (pp. 125-142). Ankara, Turkey: MTA.

Deng, L., and Cai, C. S. (2007). Applications of fiber optic sensors in civil engineering. *Structural Engineering and Mechanics*, 577-596.

Domenico, P. A. (1972). *Concepts and Models in Groundwater Hydrology.* New York: McGraw-Hill.

DSİ. (2016). *Seyhan Basin Master Plan.* Ankara, Turkey: DSİ.

Freeze, A. R., and Cherry, J. A. (1979). *Groundwater.* Englewood Cliffs, New Jersey 07632 : Prentice-Hall, Inc. .

Gaona, J., Meinikmann, K., and Lewandowski, J. (2019). Identification of groundwater exfiltration, interflow discharge, and hyporheic exchange flows by fibre optic distributed temperature sensing supported by electromagnetic induction geophysics. *Hydrological Processes*, 33:1390–1402. https://doi.org/10.1002/hyp.13408.

Gautier, P., Bozkurt, E., Bosse, V., Hallot, E., and Dirik, K. (2008). Coeval extensional shearing and lateral underflw during Late Cretaceous core complex development in the Niğde Massif, Central Anatolia, Turkey. *Tectonics*, 27: TC1003.

Gordon, R. P., Lautz, L. K., and Daniluk, T. L. (2013). Spatial patterns of hyporheic exchange and biogeochemical cycling around cross-vane restoration structures : Implications for stream restoration design. *Water Resour. Res.*, 49, 2040–2055, doi:10.1002/wrcr.20185.

Gordon, R. P., Lautz, L. K., Briggs, M. A., and McKenzie, J. M. (2012). Automated calculation of vertical pore-water flux from field temperature time series using the VFLUX method and computer program. *Journal of Hydrology*, 142-158.

Hatch, C. E., Fisher, A. T., Revenaugh, J. S., Constantz, J., and Ruehl, C. (2006). Quantifying surface water–groundwater interactions using time series analysis of streambed thermal records: method development. *Water Resour. Res.*, 42, W10410, doi:10.1029/2005WR004787.

Hausner, M. B., Suarez, F., Glander, K. E., and Van de Giesen, N. (2011). Calibrating Single-Ended Fiber-Optic Raman Spectra Distributed Temperature Sensing Data. *Sensors*, 11, 10859-10879; doi:10.3390/s111110859.

Hvorslev, M. J. (1951). Time lag and soil permeability in ground-water observations. Vicksburg, Mississippi: Waterways Experiment Station Corps of Engineers, U. S. Army.

Hyder, Z., Butler, J. J., McElwee, C. D., and Liu, W. (1994). Slug tests in partially penetrating wells. *Water Resour. Res.*, 2945-2957.

Kalbus, E., Reinstorf, F., and Schirmer, M. (2006). Measuring methods forgroundwater, surface water and their interactions: a review. *Hydrol. Earth Syst. Sci.*, 10, 873-887, doi.org/10.5194/hess-10-873-2006.

Keery, J., Binley, A., Crook, N., and Smith, J. W. (2007). Temporal and Spatial Variability of groundwater - surface water fluxes: Development and application of an analytical method using temperature time series. *Journal of Hydrology*, 336, 1-16, doi:10.1016/j.jhydrol.2006.12.003.

Kennedy, C. D., Genereux, D. P., Corbett, R., and Mitasova, H. (2009). Spatial and temporal dynamics of coupled groundwater and nitrogen fluxes through a streambed in an agricultural watershed. *Water Resources Research*, Res., 45, W09401, doi:10.1029/2008WR007397.

Kostaschuk, R., Best, J., Villard, P., Peakall, J., and Franklin, M. (2005). Measuring flow velocity and sediment transport with an acoustic Doppler current profiler. *Geomorphology*, 25-37, doi.org/10.1016/j.geomorph.2004.07.012.

Krause, S., Blume, T., and Cassidy, N. J. (2012). Investigating patterns and controls of groundwater up-welling in a lowland river by combining Fibre-optic Distributed Temperature Sensing with observations of vertical hydraulic gradients. *Hydrol. Earth Syst. Sci.*, 16, 1775–1792, doi:10.5194/hess-16-1775-2012.

Krause, S., Hannah, D. M., and Fleckenstein, H. J. (2009). Hyporheic hydrology: interactions at the groundwater-surface water interface Preface. *Hydrol. Process.*, 23: 2103-2107. DOI: 10.1002/Hyp.7366.

Lambs, L. (2004). Interactions between groundwater and surface water at river banks and the confluence of rivers. *Journal of Hydrology*, 312-326, doi.org/10.1016/j.jhydrol.2003.10.013.

Landon, M. K., Rus, D. L., and Harvey, E. F. (2001). Comparison of Instream Methods for Measuring Hydraulic Conductivity in Sandy Streambeds. *Ground Water*, 39, 870-885.

Lapham, W. W. (1989). Use of Temperature Profiles Beneath Streams to Determine Rates of Vertical Ground-Water Flow and Vertical Hydraulic Conductivity. Denver: U.S. Geological Survey Water-Supply Paper 2337.

Lee, R. D. (1977). A device for measuring seepage flux in lakes and estuaries. *Limnology and Oceanography*, 140-147.

Lee, R. D., and Cherry, J. (1978). A field exercise on groundwater flow using seepage meters and mini-piezometers. *Journal of Geological Education 27*, 6-10.

Lee, R. D., and Hynes, H. B. (1978). Identification of groundwater discharge zones in a reach of Hillman Creek in southern Ontario. *Water Quality Research Journal of Canada*, 121-133.

López-Higuera, J. M., Cobo, L. R., Incera, A. Q., and Cobo, A. (2011). Fiber Optic Sensors in Structural Health Monitoring. *Journal of Lightwave Technology*, DOI: 10.1109/JLT.2011.2106479.

Malcolm, I. A., Soulsby, C., and Youngsen, A. F. (2003). Heterogeneity in ground water-surface water interactions in the hyporheic zone of a salmonid spawning stream. *Hydrol. Process.*, 17, 601-617, doi.org/10.1002/hyp.1156.

Martinez, J. L., Raiber, M., and Cox, M. E. (2015). Assessment of groundwater–surface water interaction using long-term hydrochemical data and isotope hydrology: Headwaters of the Condamine River, Southeast Queensland, Australia. *Sci. Total Environ.*, 536, 499-516, doi.org/10.1016/j.scitotenv.2015.07.031.

Matheswaran, K., Blemmer, M., Rosbjerg, D., and Boegh, E. (2014). Seasonal variations in groundwater upwelling zones in a Danish lowland stream analyzed using Distributed Temperature Sensing (DTS). *Hydrol. Process.*, 28, 1422-1435, DOI: 10.1002/hyp.9690.

McGlynn, B. L., and McDonnell, J. J. (2003). Quantifying the relative contributions of riparian and hillslope zones to catchment runoff. *Water Resour. Res.*, 39(11), 1310, doi:10.1029/2003WR002091.

McNeill, J. D. (1980). Electromagnetic terrain conductivity measurements at low induction numbers. *GEONICS Tech. Note TN6.*, Mississauga, Ont., Canada, Geonics.

Merzbacher, C. I., Kersey, A. D., and Friebele, E. J. (1996). Fiber optic sensors in concrete structures: a review. *Smart Mater. Struct.*, 5, 196-208.

Naranjo, R. C., and Turcotte, R. (2015). A new temperature profiling probe for investigating groundwater-surface water interaction. *Water Resour. Res.*, 51, 7790–7797, doi:10.1002/2015WR017574.

Rejiba, F., Schamper, C., Chevalier, A., Deleplancque, B., Hovhanissian, G., Thiesson, J., and Weill, P. (2018). Multiconfiguration electromagnetic induction survey for paleochannel internal structure imaging: a case study in the alluvial plain of the River Seine, France. *Hydrol. Earth Syst. Sci.*, 22, 159–170, 2018, doi.org/10.5194/hess-22-159-2018.

Rosenbarry, D. O. (2008). A seepage meter designed for use in flowing water. *Journal of Hydrology*, 118-130, https://doi.org/10.1016/j.jhydrol.2008.06.029.

Schmidt, C., Bayer-Raich, M., and Schirmer, M. (2006). Characterization of spatial heterogeneity of groundwater-stream water interactions using multiple depth streambed temperature measurements at the reach scale. Hydrol. Earth Syst. Sci., 10, 849-859, doi.org/10.5194/hess-10-849-2006, 2006.

Schmidt, C., Musolff, A., Trauth, N., Vieweg, M., and Fleckenstein, J. H. (2012). Transient analysis of fluctuations of electrical conductivity as tracer in the stream bed. *Hydrol. Earth Syst. Sci.*, 16, 3689-3697, doi:10.5194/hess-16-3689-2012.

Selker, J. S., L. Thevenaz, H. Huwald, A. Mallet, W. Luxemburg, N. van de Giesen, M. Stejskal, J. Zeman, M. Westhoff, and M. B. Parlange (2006a). Distributed fiber-optic temperature sensing for hydrologic systems. *Water Resour. Res.*, 42, W12202, doi:10.1029/2006WR005326.

Selker, J. S., Tyler, S., and N. van de Giesen (2014). Comment on "Capabilities and limitations of tracing spatial temperature patterns by fiber-optic distributed temperature sensing" by Liliana Rose et al. *Water Resour. Res.*, 50, 5372-5374, doi:10.1002/2013WR014979.

Selker, J., Van de Giesen, N. C., Westhoff, M., Luxemburg, W. M., and Parlange, M. B. (2006b). Fiber optics opens window on stream dynamics. *Geophysical Research Letters*, 33, L24401, doi:10.1029/2006GL027979.

Seyitoğlu, G., Işık, V., Gürbüz, E., and Gürbüz, A. (2017). Th discovery of a low-angle normal fault in the Taurus Mountains: the İvriz detachment and implications concerning the Cenozoic geology of southern Turkey. *Turkish Journal of Earth Sciences*, doi:10.3906/yer-1610-11.

Shaw, G. D., Conklin, M. H., Nimz, G. J., and Liu, F. (2014). Groundwater and surface water flow to the Merced River, Yosemite Valley, California: 36Cl and Cl-evidence. *Water Resour. Res.*, 50, 1943-1959, doi:10.1002/2013WR014222.

Sophocleous, M. (2002). Interactions between groundwater and surface water: the state of the science. *Hydrogeology Journal*, 52-67, doi.org/10.1007/s10040-001-0170-8.

Stallman, R. W. (1963). Computation of ground-water velocity from temperature data. *Geological Survey Water-Supply Paper*, 1544-H, 36-46.

Suzuki, S. (1960). Percolation measurements based on heat flow through soil with special reference to paddy fields. *Journal of Geophysical Research*, 65-69.

Şengör, C. A., and Yılmaz, Y. (1981). Tethyan evolution of Turkey: a plate tectonic approach. *Tectonophysics*, 75, 181-241.

Todd, D. K., and Mays, L. W. (2005). *Groundwater Hydrology.* Hoboken: Wiley.

Tóth, J. (1963). A theoretical analysis of groundwater flow in small drainage basins. *Journal of Geophysical Research*, 4795 - 4812.

Van de Giesen, N., Steele-Dunne, S., Jansen, J., Hoes, O., Hausner, M. B., Tyler, S., and Selker, J. (2012). Double-Ended Calibration of Fiber-Optic Raman Spectra Distributed Temperature Sensing Data. *Sensors*, 12, 5471-5485; doi:10.3390/s120505471.

Winter, T. C., Harvey, J. W., Franke, O. L., and Alley, W. M. (1998). Ground Water and Surface Water A Single Resource. *U. S. Geological Survey*, Circular 1139.